Observation and Creation of Defects of Transition Metal and van der Waal Surfaces through Scanning Tunneling Microscopy

Dejia Kong
Beijing, China

B.S. Indiana University Bloomington, 2019
M.A. University of Virginia, 2020

A
Dissertation
Presented to the Graduate Faculty
of the University of Virginia in Candidacy for the Degree of
Doctor of Philosophy

Department of Chemistry
University of Virginia
May 2025

Abstract

The research described in this dissertation involves the study of two different kinds of surfaces: (i) Pt(111), which is a model surface for heterogeneous catalysis, and (ii) the surfaces of a range of 2D materials with technologically interesting electronic properties, which include TaS_2, iron intercalated TaS_2 and $EuZn_2As_2$.

Local real space observations were made of the dissociative chemisorption products of a branched alkane on a catalytic metal surface. The initial dissociative chemisorption of saturated alkanes on catalyst surfaces typically occurs through C-H bond cleavage, and initial dissociative chemisorption by C-C bond cleavage is rarely observed. Tetramethylbutane (TMB) is the only saturated alkane that has been conjectured to display an additional C-C bond cleavage pathway on Pt(111) at high temperatures based on dissociative sticking coefficient measurements. Scanning tunneling microscopy (STM) was used here to directly observe the fragment products from both C-H and C-C bond cleavage pathways for TMB on Pt(111) and thereby confirmed the mechanistic conjecture made earlier based on the macroscopic dissociative sticking coefficient experiments.

Interactions between the biased metallic STM tip and the surface of 2H-TaS_2 bulk crystal were investigated. Tip-induced surface structure manipulation has displayed potential towards the application of scanning probes in surface nanolithography, and it is vital to understand the roles of surface and tip conditions to progress this application in a practical way. STM and scanning transmission electron microscopy (STEM) experiments provided a surface defect inventory of chemical vapor transport (CVT) grown 2H-TaS_2 crystals which were consistent with a clustering and propagation of defect structures during the CVT growth. At high defect concentrations, the

STM tip-induced growth of defect vacancy islands (VIs) in the monolayer was linear in time for the VI perimeter and parabolic in time for the VI area. New vacancies emerged from layers below the surface after the top layer was removed during the etching process. More importantly, mobile surface islands/flakes were revealed to play a crucial role in the tip-induced etching mechanism.

Anisotropic ferromagnetic phases can be introduced to transitional metal dichalcogenide (TMD) 2H-TaS_2 through intercalating Fe in the van der Waals (vdW) gaps. By deviating from the commensurate values (x = ¼ or ⅓), the crystalline structure as well as the magnetotransport properties of the TMD system can be tuned. For instance, $Fe_{1/4}TaS_2$ has a centrosymmetric 2 × 2 structure while $Fe_{1/3}TaS_2$ has a non-centrosymmetric $\sqrt{3} \times \sqrt{3}\, R30°$ supercell structure. The magnetic Curie temperature of Fe_xTaS_2 also exhibits a strong dependence on Fe concentration. We evaluate $Fe_{0.28}TaS_2$ and 2H-TaS_2 samples using STM/Spectroscopy (STM/S) and density functional theory (DFT) to investigate the real-space intercalant electronic structure comparatively and the potential phase segregation between the two commensurate compounds. $Fe_{0.28}TaS_2$ shows a $\sqrt{3} \times \sqrt{3}\, R30°$ supercell at 77 K, whereas 2H-TaS_2 displays no apparent supercell at the same temperature. Fe vacancy defects and clusters are discovered in the intercalated surface, and their surrounding local density of states (LDOS) shows non-trivial differences at energies compared to the pristine $Fe_{0.28}TaS_2$ area, which is believed to be related to Fe orbitals contributions based on DFT calculations. These investigations are important to better understand the anomalously high peak in the magnetoresistance displayed by Fe_xTaS_2 materials with x = 0.28.

The surface electronic structure of $EuZn_2As_2$ was studied, and a deep-learning-based workflow and DFT were employed to determine the termination of the surface in a complex defect

environment. EuM_2As_2 (M = Zn, Cd, In, Sn, etc.) are excellent material systems for studying electronic topological properties, which can be easily tuned by application of magnetic fields. Theoretical calculations predict gapped and flat bands in the LDOS for $EuZn_2As_2$ but a gapless structure in $EuCd_2As_2$. In this work, low-temperature (77 K) cleaved $EuZn_2As_2$ crystals were studied using STM/S and DFT calculations. Characteristic defects imaged as triangular shapes with modified LDOS helped identify the surface terminations: Eu versus As capped surfaces. While large bandgaps (~1.5 eV at 77 K) are observed on both pristine surfaces, the bandgap width is found to be very sensitive to local heterogeneities, such as defects and step edges, that tend to reduce the bandgap. Combining experimental data with DFT simulations, we conclude that the modified bandgap in the heterogeneous area arises from Zn sub-surface vacancies and/or substitution into those Zn vacancies by As atoms. Our investigation offers important information for evaluating the electronic structure topology of the EuM_2As_2 family of materials by establishing a methodology to correctly identify the exposed surface plane under study by STM/S.

Acknowledgements

First, I would like to thank my advisor Prof. Ian Harrison for having me on your team and supporting me on the journey of ultra-high vacuum and scanning tunneling microscopy. Ian was the first person I met from the Department of Chemistry when I joined UVa as a master's student. He welcomed me to join his research group when I had little research experience and always kept his office door open for me when I was baffled by technical issues in the lab and when I needed help with proposals. I am glad and grateful that our effort paid off.

I would also like to thank Prof. Petra Reinke for her altruistic aid during the early days of bringing our VT-STM back to life. I learned so much about material science from her class and our collaboration. Petra shared her time, resources, and her enthusiasm for research even though I brought few results to the table for years.

I want to thank Dr. Zheng Gai for giving me the opportunity to work at Oak Ridge National Laboratory. Zheng put a lot of time and effort into guiding me through all of my projects, and she trusted me to use her laboratory's resources freely. I have learned from her step-by-step how to work with STM in uncharted territory.

There are many people who helped me along the way in restoring the STM chamber. Many thanks to my lab mates, who helped me work through the tough days. Dr. Xingyu Wang and Dr. Mark Bernard taught me so much in the lab and were always willing to help with my projects. Richard worked alongside to solve the mysterious noise in the STM and take the long shift in STM experiments. Julissa and Kason were in the lab for me when I needed a hand countless times. And

to all the friends I met in the Department of Chemistry and MSE, I am incredibly lucky to have you through the past and beyond.

Special thanks to Alex Skripnik and Randy Dellwo, who never missed a single email and were patient to see every problem being solved. I would also like to thank Yiren and Lin for their friendship and advice.

In the end, I would like to say thank you to my family. My absence was not easy for you, and I can't say thank you enough for the sacrifice you made. You have been a constant source of love and support to me, and I am really looking forward to going back home again.

Contents

Chapter 1. Introduction

Defects are imperfections in the crystalline lattice structure. Conventionally, these imperfections are viewed as shortcomings of the material, leading to detrimental impacts on material structure and departure from the material's inherent properties. To get a better understanding and control of defects, a general three-step method, including (1) measuring the dimensionalities of the defects; (2) adjusting preparation pathways to regulate the generation of defects and (3) studying the effects of having defects on the physico-chemical properties and applications of the materials, is widely adopted to examine defects from atomic vacancies to micropores. While minimizing defects is necessary from the perspective of growing high-quality material, the presence of defects is never completely avoidable in an experimental setting, per the second law of thermodynamics. In addition, studies of defects, especially those on the surface, in materials have demonstrated their key roles in engineering novel industrial catalysts, electronic components, and quantum materials by intentionally deviating from the material's inherent properties.

Understanding the surface defects is also important to the effort of transitioning the first-principal calculation knowledge to materials application, because the introduction of the defects complicates the calculations on surfaces, enlarging the periodic unit cell into a larger supercell. Needless to say, the supercell needs to be large enough to avoid interactions between the defect sites in neighboring supercells, which makes the calculation computationally expensive. The nature of first-principal calculations points to a simple fact: the computational prediction and modeling of surface defects becomes less accurate as the defect density decreases. With the recent rampant evolution of microscopic and vacuum technologies, the scientific community can observe

and control atomic and sub-atomic defects more accurately than ever. However, such success often comes with the requirement of extreme conditions like ultra-high vacuum, cryogenic environment, and long experimental observation time. Furthermore, there is still an existing knowledge gap in modeling individual atomic defects to the global physico-chemical properties of the material. As a result, new additions need to be made to the conventional material research methodology to connect local defects to global properties. In this dissertation, we start by demonstrating the observation of local defects can be used to reinforce conjectures drawn from the macroscopic measurements. Then, two different strategies are introduced to find and study local defects with a low abundance. A scanning probe-based surface etching is shown to be a potential way to create local defects and single-layer patterns on 2D materials, and a deep learning-driven strategy is introduced to search for local defects on layered materials automatically.

1.1 Alkane Catalysis on Single Crystal Surfaces

Serving as the simplest hydrocarbons with only single bonds, alkanes, especially light alkanes (C_1-C_4) hold significant importance in the chemical production process like olefins, aromatics, and alcohols.[1] The use of a homogeneous or heterogeneous metal catalyst, or a combination of both, is one of the most important routes in the activation of alkanes since the single bonds in the alkanes are energetically expensive to break.[2] The alkane C-H bond energies (ca., 410-439 kJ/mol) are typically greater than those of C-C bonds (ca., 323-377 kJ/mol) in alkanes. However, it is usually C-H bonds instead of energetically weaker C-C bonds that break first in dissociative chemisorption, presumably because C-H bonds have better steric access to the surface. The catalytic platforms for alkane activation are often supported metal catalysts, due to the high cost of pure transition metals and their vulnerability to coke deposition. With the

introduction of oxide support, coke formation can be either partially suppressed or easier to remove. However, the surface reaction dynamics and kinetics are harder to understand with the participation of other elements. In past research within Harrison group, platinum (Pt), an active catalyst for alkanes, has been studied to understand the reaction dynamics and kinetics of light alkane dissociative chemisorption.[3-6] In its pure form, Pt(111) surfaces and its step edge sites can be rapidly deactivated by the accumulation of carbonaceous deposits or "coke" during the alkane dissociative chemisorption. In a recent Harrison group study, the step edge sites of the Rh(111) surface were found to remain active during the dissociative chemisorption of methane and ethane, which emphasizes the importance of site-resolved chemistry and carbon products' dissolution and segregation in the study of dynamics and kinetics.[7]

1.2 Defect-Dominated Reactivity on Rh(111)

Isomeric and branched alkanes offer unique properties in industrial applications. For example, octane rating, which measures gasoline's ability to withstand compression in an internal combustion engine without causing knocking, is closely related to the type and the ratio between the alkane compound in the gasoline.[8] Highly branched isomers of alkanes, like 2,2,4-Trimethylpentane (Octane rating standard point), provide a higher octane rating due to their slower combustion kinetics compared to chain n-alkanes.[8] Pt group transition metal surfaces serves as both dehydrogenation and hydrogenation catalyst, which can be regulated by the hydrogen pressure, providing an ideal environment for investigating the initial steps of the isomerization process.[9] In a previous effusive molecular beam study of C_1-C_9 alkane reactivity on Pt(111) in the Harrison group, it was found that activation barriers for alkane dissociative chemisorption by C-H bond cleavage fell monotonically with increasing van der Waals (vdW) interaction with the

surface.[10] Amongst the group of alkanes studied, the Arrhenius plot of the thermal dissociative sticking coefficient of 2,2,3,3-tetramethylbutane (TMB) showed two branches, a low-temperature branch with an activation energy of 10 kJ/mol that was consistent with C-H bond cleavage and the behavior of the other alkanes, and a high-temperature branch that began at 560 K with an activation energy of 40 kJ/mol that was attributed to C-C bond cleavage in part, by analogy to reports for higher temperature C-C cleavage for C_3-C_4 alkanes on the more reactive Ir(111) surface. Johnson & Weinberg's studies on Ir(111) identified a low-temperature C-H bond cleavage pathway for the C_3-C_4 alkanes by its primary H/D kinetic isotope effect and deducted that the negligible H/D kinetic isotope effect at high temperature was based on C-C bond cleavage.[11] In a different experiment, interestingly, the Arrhenius plot of the thermal dissociative sticking coefficient of methane on Rh(111), also shows two branches, a low-temperature branch with an activation energy of 36.7 kJ/mol that was attributed to defect reaction sites, and a high-temperature branch that begin somewhere between 600 K to 700 K with an activation energy of 74.3 kJ/mol that was attributed to terrace reaction sites.

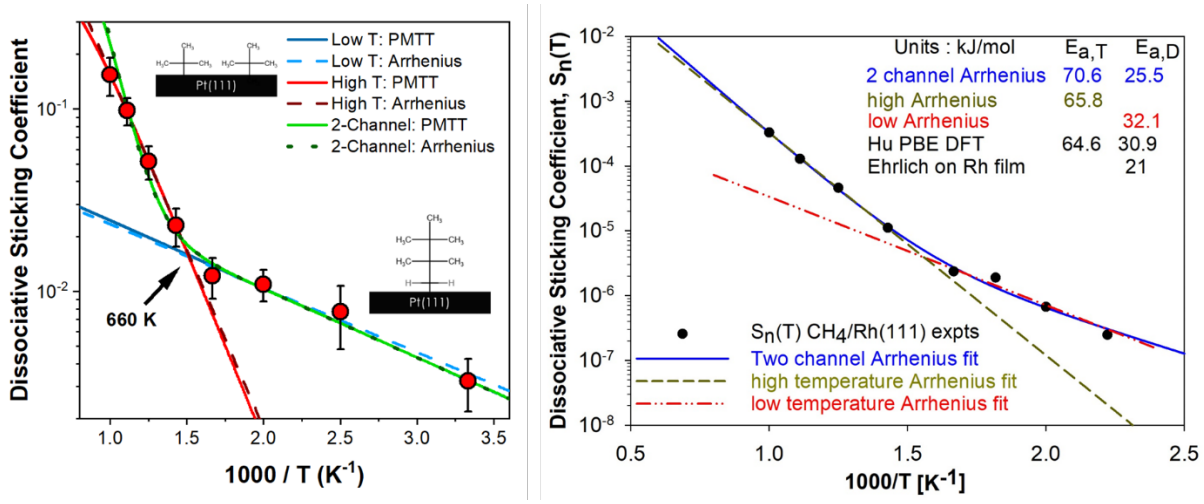

Figure 1-1 (Left) 2,2,3,3-tetramethylbutane thermal dissociative sticking coefficients on Pt(111) from 300 to 1000 K;[10] (Right) Methane thermal dissociative sticking coefficients on Rh(111) from 300 to 900K.[7]

The similarity in two-slope behavior in the Arrhenius plots between different alkanes on the Pt(111) and Rh(111) leads to the discussion of using a secondary technique to study the dissociative chemisorption products on these two surfaces for the reason that global experimental methods like Auger electron spectroscopy are not comprehensive enough to explain structural and site-dependent chemistry by themselves. One conventional way to differentiate dissociative chemisorbed alkanes on transition metal surfaces is to deuterate the alkanes and expect an absence of kinetic isotope effect for the C-C bond cleavage reaction.[11] However, per-deuterated TMB is not commercially available and difficult to synthesize in our lab. For methane on Rh(111), sputtering the surface to generate more defect sites was carried out as a proof of concept. However, at the terrace-dominated reaction temperature, the Rh surface starts to reconstruct, eliminating the defect sites gradually. In addition, the estimation of defect site density requires a surface-sensitive local probe technique. STM can compensate for the limitations in both experiments because its

real-space imaging not only gives us more information on the reaction products like chemisorbed TMB radicals or *tert*-butyl (isobutane) fragments in terms of their sizes and density but also can resolve the reaction site contribution based on the relative position of the chemisorbed carbonaceous species to the step edges. At the time, we decided to use the idle UHV-STM in the Harrison lab to examine the TMB on Pt(111) system first because the dissociative chemisorption sticking coefficient through background gas dosing is high enough to provide sufficient coverage on Pt(111) for real-space imaging. Also, our lab has a distant history of working with Pt(111) using STM at low temperatures.[12-14]

1.3 2D Materials

To accelerate the process of bringing our UHV-STM back to full capacity, highly oriented pyrolytic graphite and transition metal dichalcogenides (TMDs) were used to achieve atomic-resolution imaging at room temperature. These 2D materials are chosen because they are generally easy to clean because they don't have dangling bonds at their surfaces, which makes them more resilient to oxidation compared to transition metal single crystals. TMDs are a group of monolayer materials that have molecular composition MX_2, with one layer of M transition-metal atom sandwiched between two layers of X chalcogen atom. Bulk crystals of TMDs are formed of monolayers bound to each other by van-der-Waals forces. This anisotropic structure results in distinct properties along the plane of the layers compared to perpendicular to the layers.[15] For this reason, TMDs have attracted extensive attention in the last two decades for their potential in electrical,[16,17] magnetic,[18] optical,[19,20] and catalysis[21-23] applications. Chemical vapor transport (CVT) is the most common method used to grow TMD crystals.[24] During the growth of these materials, intrinsic defects are inevitably formed. Atomic vacancies are the most common type of

defects in TMDs. They can also be engineered during chemical vapor deposition (CVD) growth by either tuning the precursor composition, flow rate and temperature, or adjusting the temperature of the target sample.[25] Vacancies can also form post-growth by applying thermal annealing,[26,27] electron radiation,[27,28] and etc.. And once the vacancies exist in the sample, further surface treatment can introduce substitution defects.[29] The electronic states at the step edges and the defects on TMD surfaces are very different from the states in the crystal bulk, hence the local physical and chemical properties around the defect are drastically different from the pristine surface. Characterizing these defects provides opportunities for bridging the knowledge gap between ideal surfaces and real-life practical technology. STM has been used for studying the defects in TMDs and site-dependent physical and chemical properties.[30,31] During our experiments on 2D materials, it was found that the prolonged scanning on the surface and abrupt changes in the tunneling conditions can create defects of various sizes, which encouraged us to pursue the functionalization of tip-induced defect creation and modification of the local electronic structure of the TMD surfaces.

1.4 Scanning Tunneling Microscopy

In 1981, Binning and Rohrer developed the first scanning tunneling microscope in the IBM Research Laboratory and showed the real-space image of atoms on Si(111) surfaces for the first time.[32] Their invention provides a unique approach to study disordered structures and low density defects on conductive surfaces. The STM operates based on the quantum tunneling of electrons through the vacuum barrier between two conductive objects. When the distance between these two objects is only a few angstroms, the wave functions of the electron states on both sides start to overlap and the tunneling probability increases exponentially as the objects get closer to each other.

In the case of STM, an atomically sharp tip is used to create the tunneling junction between the lowest atom of the tip and the sample surface and raster the tip across the surface with a feedback loop to gauge the distance between them. The unique tunneling interaction between the two atoms on both sides gives STM an unrivaled spatial resolution. On top of that, the scanning tunneling spectroscopy (STS) maps can also provide great energy resolution, which is essential for evaluating the surface local density of states (LDOS) and offering atomic-level information for understanding energy-sensitive phenomena such as superconductivity, [33] phase transitions.[34,35]

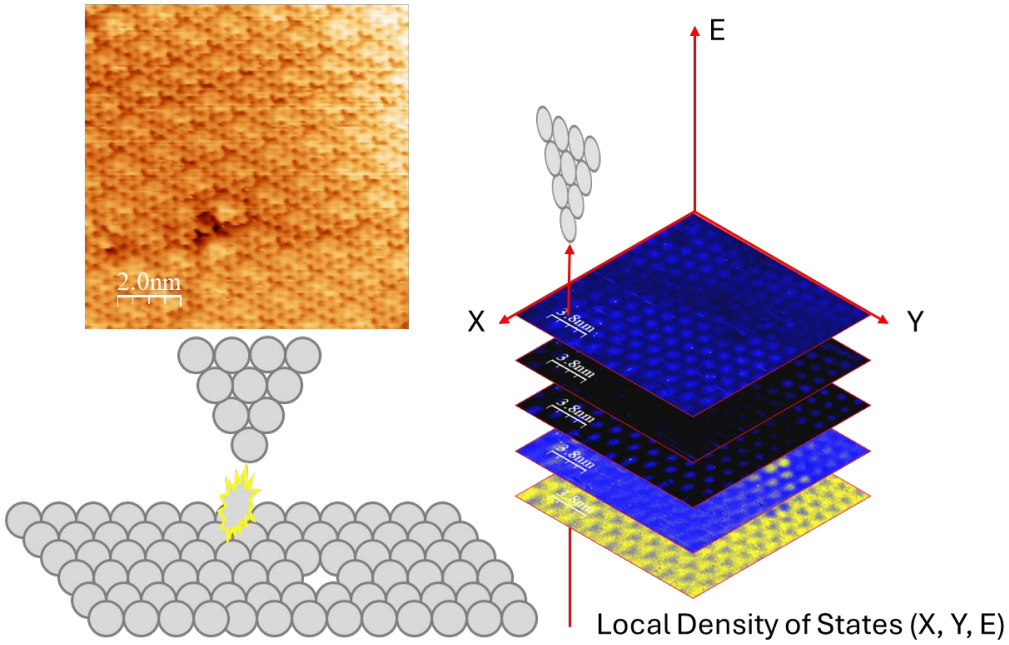

Figure 1-2. A metal probe-tip is raster scanned across a surface by piezoelectric motors. The feedback loop keeps either position Z or current I to the sample constant and records the other variables to generate STM images. If an STS spectrum is collected at each raster point then a hyperspectral STS image is collected.

The use of STM in studying chemical dynamics and kinetics at the gas-surface interface is difficult to do because STM doesn't have absolute chemical sensitivity due to the variability in the tip DOS but combined with other *in-vacuo* surface detection techniques, STM can be a powerful tool to study physical and electronic structures of the surface reaction products. Tip-enhanced Raman spectroscopy has been developed to chemically identify surface species with STM spatial resolution.[36] Merino *et al.* showed that a low temperature STM tip can be used to extract photon correlations in the far-field electroluminescence of C_{60} molecules on an Ag(111) single-crystal.[37] In the absence of other techniques, Chapter 3 of this dissertation relies on replicating the surface reactions in a separate UHV chamber and connecting the results from global probe techniques and local probe techniques.

It is well known that STM experiments often take enormous amounts of time to conduct because STM is an extremely local technique, especially while looking for specific types of defect sites with low defect concentrations on the surface. The common procedure for STM experiments is that a human operator selects sample regions to scan and assesses the acquired image's quality based on mostly experience, which usually takes most of the time during the experiment before any data collection. Pre-trained deep learning models have been developed in the interests of structural classification,[38,39] defect detection,[40] artifact correction,[41] and automatic tip conditioning.[42] These display the potential of using machine learning (ML) and convolutional neural networks (CNN) applications to reduce the manpower spent on STM data collection. However, there are several challenges to implementing a reliable pre-trained deep learning model for the fully automatic experiment: First, no sample can provide a surface that has a consistent angle of tilt across multiple points. As a result, a human operator needs to evaluate the surface on

approach and then decide whether to start collecting data, perform tip conditioning, or relocate the scanner. This is still challenging since the surface needs to be evaluated while the tip's states are constantly changing, and a combination of STM and STS is normally used instead of only image-based analysis. Secondly, the model trained on a specific sample doesn't necessarily work on a different sample. The chemical composition and the history of the sample are normally considered during the identification of a surface feature, but they are rather difficult to define in image-based neural networks, implying the need to retrain for every new sample. Lastly, during the STM experiment, electrical contact with the surface can cause the tip apex to spontaneously and randomly change, modifying the wave function of the tip's electrons and therefore changing the data acquired nonlinearly. This means that in the supervised study, the ground truth data are not unique in the sense that only one type of image represented perfect tip states, instead every tip state has a unique interpretation. In this dissertation, a deep learning method from automated atomic force microscopy is introduced to STM, which combines the correlative power of the deep learning model with human-defined physics-based scalars that drive model optimization.[43,44] The automation of the STM experiment was explored in this dissertation in an effort to reduce the downtime of STM and to verify the reproducibility of defect STS results. Additionally, the combination of human knowledge and deep learning-driven automated exploration offers a novel workflow on the path towards fully automated STM experimentation.

Chapter 2. Experimental

2.1 Ultra-high Vacuum

To keep the sample's surface as clean as possible, all experiments discussed here are performed in an ultra-high vacuum environment. The vacuum condition is more impactful while working with a local real-space imaging technique like scanning tunneling microscopy. Having different contamination residues on the sample surface is obvious during the STM experiments and they are hard to distinguish from experiment-related adsorbates. The UVa VT-STM maintains a base pressure of 5×10^{-11} Torr. High vacuum conditions are achieved with a TMH-262 Pfeiffer turbo-molecular pump with a nominal pumping speed of 210 L/s for N_2. Ultrahigh vacuum conditions are achieved and maintained with three ion pumps in each chamber and the titanium sublimation pump (TSP), which is operated at 42 A for 2 minutes every week. The other apertures that are attached to the chamber but not used in this dissertation are also shown in Figure 2-1. The CNMS VT-STM maintains a base pressure of 3×10^{-10} Torr. The connected molecular beam epitaxy chamber maintains a base pressure of 10^{-8} Torr but the gate valve connected to it has never opened since 2015. High vacuum conditions are achieved with a Leybold TURBOVAC 361 turbo-molecular pump in the main chamber with a nominal pumping speed of 345 L/s for N_2 and a Leybold TURBOVAC 50 in the load lock with a nominal pumping speed of 55 L/s for N_2. Ultrahigh vacuum conditions are achieved and maintained with an ion pump and the TSP, which is operated at 45 A for 2 minutes every week, and after alkane dosing. The Unisoku STM chamber maintains a base pressure below 10^{-11} Torr while the STM is under constant cooling at a temperature around 77 K. The preparation chamber maintains a base pressure of 8×10^{-11} Torr.

High vacuum conditions are achieved with a Seiko Seiki STP-300 turbo-molecular pump with a nominal pumping speed of 340 L/s for N_2. Ultrahigh vacuum conditions are achieved and maintained with two ion pumps, one in each chamber, and the TSP, which is operated at 45 A for 2 minutes only after the chamber is opened to the load lock.

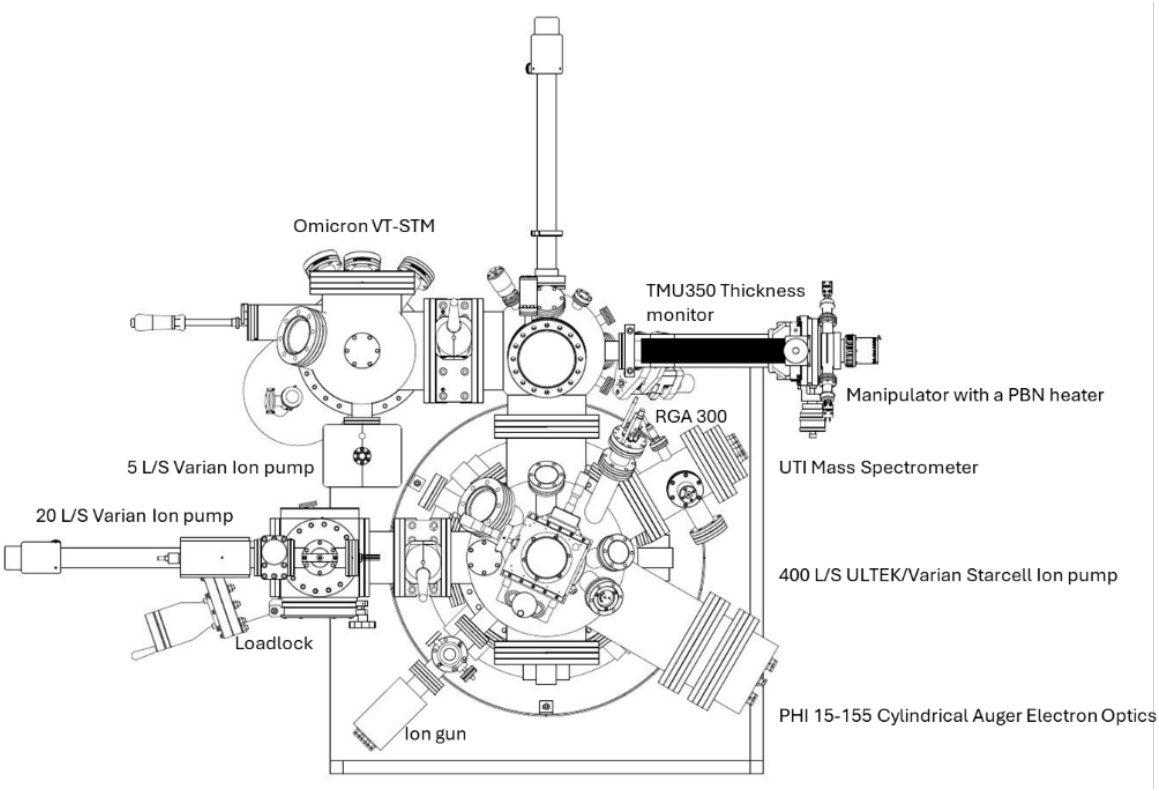

Figure 2-1. Schematic diagram of the UHV VT-STM chamber at University of Virginia. CAD drawing by Mark Bernard.

2.2 Temperature Control and Measurement

The Pt(111) single crystal is spot welded on to a piece of tantalum foil to adapt the Omicron resistive heating sample plate (B001387-S). The sample is mounted in front of a pyrolytic boron nitride (PBN) heating element. The sample and one of two contact bars are grounded to the sample plate, and the other contact bars are floating and can be used to apply a heating voltage to the PBN

heater. The resistance between the heaters should be measured as 15 to 25 Ω at room temperature. During the experiment in the preparation chamber, the temperature of the sample is measured through an infrared pyrometer at temperatures above 500 K, and a temperature calibration curve was provided by Omicron for sample temperatures below 500 K. The real temperatures are later calibrated with a K-type thermocouple spot welded on the side of the Pt(111) sample. During the STM measurement, the sample stage temperature is measured by a Si diode temperature sensor located at the clamping block. In the Unisoku STM, temperature measurements of the STM stage, the cryostat bath, and the cleavage stage are taken by type K thermocouples and controlled by a Lakeshore temperature controller. The controller can control the counter heating on the STM stage and cryostat bath with DC resistive heating. The Au(111) single crystal is mounted onto a Unisoku sample plate with an electron beam heating filament mounted on the bottom of the crystal for sputtering and annealing. The electron beam heating is carried out on the preparation chamber manipulator.

2.3 Sample Preparation for Single Crystals

Cleaning of the surface of single crystals like Au(111) and Pt(111) is primarily accomplished by physical cleaning via ion sputtering. The ion gun is generally constructed with two main parts: a heated filament to boil off electrons that can ionize the gas molecules nearby, and a high-voltage gun that provides a voltage gradient that accelerates and focuses the ions into an ion beam. The gas molecules, in this case, Ar, can be introduced either by backfilling with a higher Ar background pressure in the enclosed chamber or introducing Ar directly to the end of the ion gun which allows for a lower Ar pressure in the chamber. The objective of both methods is to provide 1keV Ar^+ ion collisions with the surface to sputter away surface atoms in a reasonable

amount of time. During the initial sputtering of the samples after their exposure to air, the samples are kept at room temperature, and no annealing is needed for the first few sessions. This is important for Cu(111) or Rh(111) since the carbon and oxygen species on these surfaces are mobile if heated and it will be harder to clean the bulk of the sample. Before the experiment, the typical cleaning procedure for Pt(111) is to maintain Ar pressure at 5×10^{-5} torr, 1 keV ion energy, and 800 K surface temperature for 1 hour. Then, pump out the Ar gas, and turn off the ion gun and filament. Release O_2 gas into the chamber , and maintain surface temperature at 800 K for 1 hour. When the ion gauge reading drops below 10^{-10} torr after the O_2 cleaning, heat the sample to 1150 K for 10 minutes.

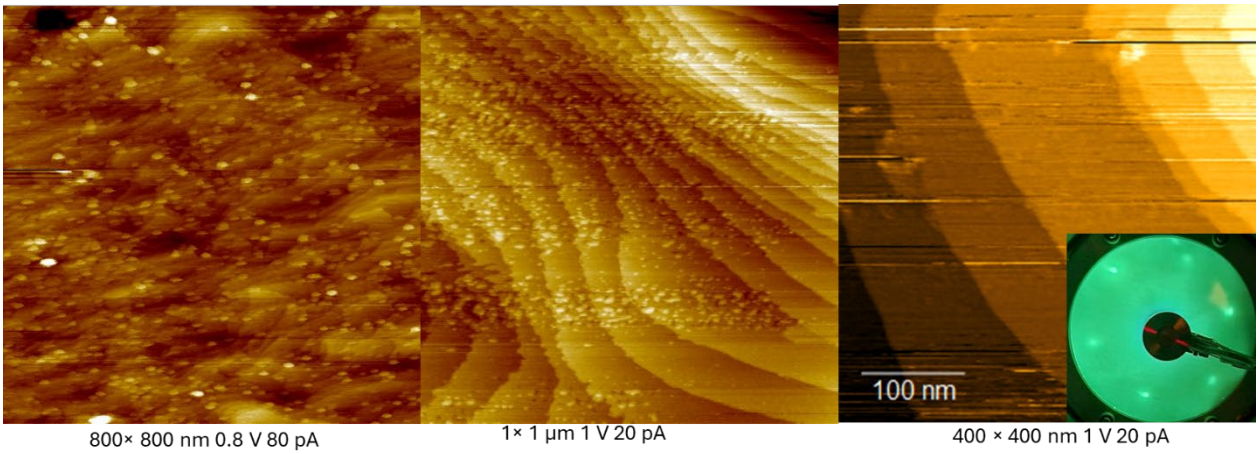

Figure 2-2. STM topography of Pt(111) after sputtering for 30 minutes and annealed at (a) 1000 K, (b) 1150 K, and (c) 1150K after oxygen cleaning.

During the initial operation of the ion gun system, a grounded phosphor screen sample can be used to establish a visual observation of the beam spot. The phosphor screen emits photons when bombarded by high energy particles. The light spot can faint so all the light sources in the room need to be switched off including the ion gauge.

Due to the recent progress in van der Waals materials in electrical, magnetic, optical, and chemical applications, the cleavage of such materials to manufacture thin layers receives extensive attention. Making these 2-D materials in bulk and then exfoliating them into thin sheets reduces the cost and difficulty in the initial synthesis phases and transportation. Top-down methods include mechanical cleavage,[45,46] chemical oxidation-reduction,[47] liquid-phase exfoliation,[48] and electrochemical exfoliation.[49] In this work, for the 2-D materials studied, the mechanical cleavages are utilized either through *ex-situ* cleavage through simple office Scotch tape, or *in situ* cleavage with an epoxy sandwich. With the sample mounted on the sample plate, press a piece of adhesive tape against the mounted sample and pull. Thin flakes of the sample should be visible on the tape. Then transfer the sample to the load lock of the UHV chamber immediately. This method can also be carried out inside the load lock by taping the other end of the scotch tape to the load lock flange and cleaving by moving the transfer arm. The Epoxy sandwich setup is used at the CNMS facility in the Unisoku high field STM, but it should work with most of the commercial STM sample plates. In a realistic scenario, samples received from our collaborators have varied sizes from ~0.5 mm to 1 cm, and it's not easy to apply the commercial sample fixation parts to all situations. One way to establish conductive fixation between the sample plate and the sample is through vacuum friendly, silver-filled epoxy paste, EPO-TEK E4110-1oz electrically conductive epoxy. We use Torr-Seal resin to establish contact between the surface of the sample and a flat-head bolt. Any vacuum friendly bolts or screws should do as long as the head of the part is flat so it can stay vertically straight during the curing process. The contact area between the Torr-Seal and the silver paste epoxy should be minimized to avoid removing the whole assembly during the cleavage. EPO-TEK E4110-1oz uses a mixing ratio of 10:1 between parts A and B. Torr-seal uses a mixing

ratio of 2:1 between parts A and B. Curing of the Epoxy and Torr-Seal is carried out at 125 °C for 30 minutes. For temperature-sensitive samples, they can also be cured at room temperature for more than 24 hours. The cleavage stage can cool the sample holder to 81 K by flowing liquid nitrogen through it. Once the temperature is stable, the cleavage can be carried out by the wobble stick hammer. Use the hammer to give the screw an abrupt nudge, and ideally, half of the sample remains on the sample holder.

Figure 2-3. (a) A side-view schematic showing the layers in the epoxy sandwich.(b) A top-down view of the sample plate after the silver-filled epoxy is cured. (c) A side-view of a sample plate right before the cleavage. The hammer is in the background out of focus. (d) The sample plate after cleavage.

O_2, Ar, and Tetramethylbutane (99.999% from Airgas, 99.99% from Air Liquide, and ≥94% from Sigma-Aldrich, respectively) are admitted into the chamber through a gas manifold

connected to the preparation chamber of the ORNL VT-STM. TMB has a solid form at room temperature and sublimates quickly. They were transferred into a Swagelok connector end piece with a gate valve as the transport container between UVa and ORNL. The Swagelok junction was then connected to a vacuum manifold pumped by a HiCube 300 Neo pumping station. The TMB was freeze-pump-thawed to remove impurities like Isobutane, Butane, Ethane, 2,2,3-trimethylbutane and Methane. The junction was transported to ORNL and then installed to the VT-STM manifold. Gas phase TMB was released into the chamber and the purity was checked by an SRS residual gas analyzer. It is worth noting that the TMB can be broken down into smaller alkanes rather effectively by using the TSP.

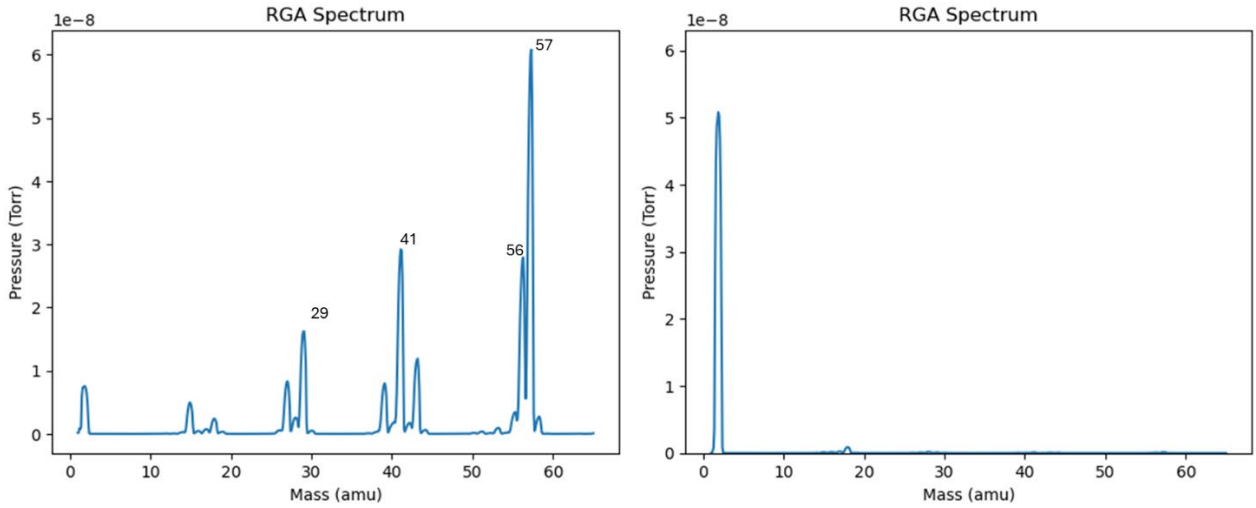

Figure 2-4. RGA spectra of the UHV chamber (left) right after dosing TMB, and (right) 20 minutes after using the TSP. We can see significant decrease in TMB fragments[50] at 57, 56, 41, 29 m/z and increase of hydrogen gas.

2.4 STM Tip Making and Conditioning

In this work, the electrochemically etched tungsten, nickel, and mechanically cut $Pt_{90}Ir_{10}$ tips are used. The method of making sharp metallic tips electrochemically was originally

developed from samples preparing method for field ion microscopy (FIM)[51] before STM was invented. The following reactions take place:

$$Cathode: 6H_2O + 6e^- \rightarrow 3H_2(g) + 6OH^-$$

$$Anode: W + 8OH^- \rightarrow WO_4^{2-} + 4H_2O + 6e^-$$

$$Overall: W + 2OH^- + 2H_2O \rightarrow 3H_2(g) + WO_4^{2-}$$

Two different types of electrochemical etching setups were used throughout this dissertation. The first is generally called the DC drop off method. A piece of tungsten wire (diameter = 0.5 mm) mounted on the micrometer is submerged into a beaker with 4M NaOH solution. A positive voltage of 4 V is applied to the wire and the cathode is a stainless wire placed in the solution. The process ends with a piece of the wire dropping from the tip.

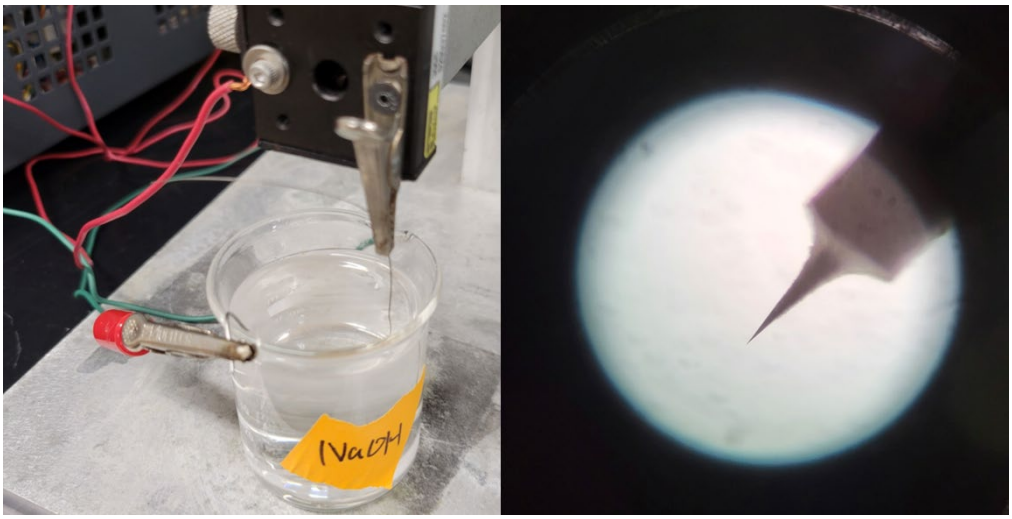

Figure 2-5. Etching setup for DC drop off method and qualitative microscopy image of the tip apex. Wire diameter = 0.5 mm.

The second setup utilizes a method which was described as “lamella drop off”, where the electrochemical reaction is happening within the solution held by a metal loop. The benefit of this

method is that two tips are being created simultaneously from a single etch. And by introducing another metal loop as a second electrode, the etching voltage can be applied through two solution lamellae, instead of the micrometer holding the wire. This provides an instant voltage cut-off when the bottom tip drops from the wire. The most critical parameter that affects the final shape of the tip apex is the time for the etching current to cut off after the wire breaks in halves, because the apex of the tip remains submerged in the solution, and further electrochemical reaction after breakage will cause blunting. To shorten the cutoff time, a commercial etching box that utilizes comparator circuits is available to help shut off the etching voltage and disengage the wire from the solution by setting a threshold to either the current or the current variation. However, it is worth noting that the bottom part of the lamella is stretched out by gravity, so the bottom piece of the wire always has a longer shank compared to the top part, giving it a better macroscopic shape. In addition, after the drop off the bottom part loses contact with the solution instantly, so the most used method in this work is to catch the bottom piece since they are generally better, and no cut-off circuit is needed. It is quite common for the solution lamella to break during the etching process due to bubbling from the hydrogen gas production. As a result, it is recommended to have a CCD camera providing an enhanced view at the etching junction so that the user can resume the etching at the same junction after restoring the lamella.

For Nickel tips, the same procedure is followed but the NaOH solution is replaced with the KCl solution.[52] The following reactions take place:

$$Cathode: 2H_2O + 2e^- \rightarrow H_2(g) + 2OH^-$$

$$Anode: Ni + 2Cl^- \rightarrow NiCl_2 + 2e^-$$

The concentration of $NiCl_2$ in the solution quickly saturates and forms a solid halo around the etching junction. Ammonia solution is effective in removing these residues once the etching is complete.

Pt/Ir tip can be created by cutting the wire directly using a wire cutter. Use the wire cutter to grab the wire but don't cut through the wire completely, and then pull or push the wire with the wire cutter along the direction of the wire to create a fracture. This procedure creates multiple nanotips at the breakage position, and Pt/Ir tips are believed to be more stable in ambient conditions. Only a few Pt/Ir tips were used in this dissertation during the initial calibration of the VT-STM at UVa.

In situ tip treatments are used throughout all the experiments in this dissertation, which include tip voltage pulse, high field scanning, and controlled tip crash. The importance of tip treatment was recognized in the initial work of STM by Binnig and Rohrer, where they realized that the radius of the tip apex must be smaller than 10 Å.[32] The tip voltage pulse is carried out by applying a voltage that is 2-3 V higher than the imaging bias on top of the artefact for 3-20 ms. The high-field scanning was first demonstrated with a W tip on Al(111) surface.[53] This can be done on a clean and flat surface while scanning with a voltage higher than 4 V for a long period of time. The field applied to the tip stimulates the W atoms toward the apex due to the highly nonuniform electric field, and with a higher voltage applied, the faster the apex is going to reconstruct.[54,55] Once the image is stable across scans, retract the tip, and move to a new area. Restore normal imaging conditions to examine the tip sharpness, because the surface under the high field scanning is mostly like going to be disrupted by the tip adsorbates ejected from the treatment. For controlled tip crash, the tip is rammed into the surface for less than 200 nm deep

and retracted with a high field applied. This process was used by Binnig and Rohrer in their revolutionary paper on Si(111) 7 x 7 reconstruction.[56] Soft and well-controlled surfaces like Au(111) and Pt(111) are preferred substrates for tip crash since it's easier to find a crash angle close to 90 degrees, and even if the surface atoms attached to the tip, they don't cause too much instability in the STM experiment. On the contrary, crashing on 2D materials sometimes might work but most of the time, the tip extracts 2D flakes that could cause severe instability. Au(111) is also the go-to sample for conditioning and calibrating tips before an experiment. As shown in Fig. 2-6, the tip was conditioned using previously mentioned methods until a clear herringbone pattern is visible and the signpost -400mV feature is stable in STS spectra.

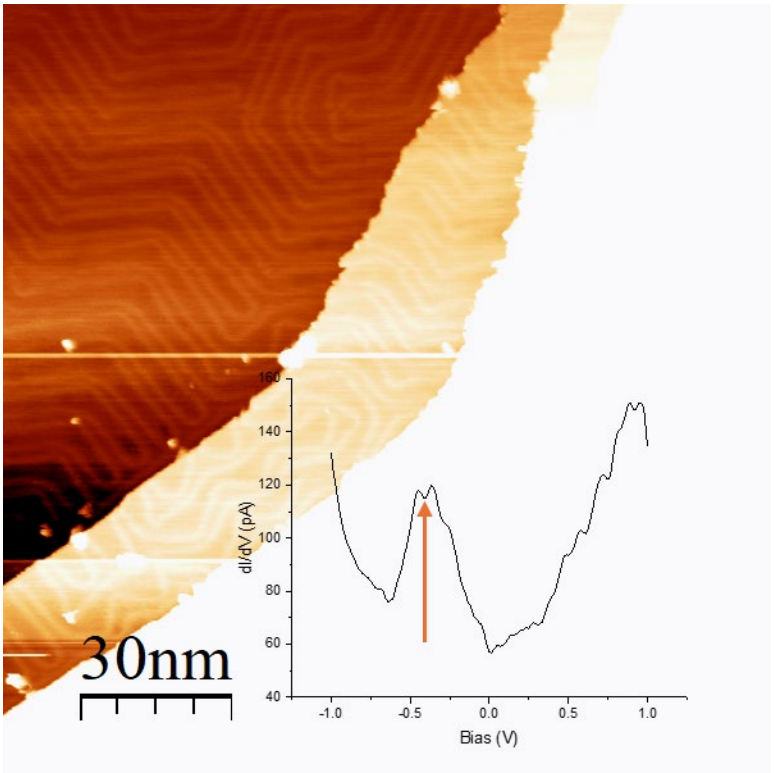

Figure 2-6. STM image of Au(111) taken with W tip after calibration (V= -1 V, I_t= 100 pA). Inset shows the dI/dV spectrum with the signature state at around -400 mV.

To get the apex of the tip into the vicinity of establishing tunneling current. An auto-approach method is used for most of commercial STM electronics. The piezoelectric motor along the z direction is going to extend and the feedback loop will be turned on to try to find any tunneling current. If no tunneling current is found or the current set point is not reached, the piezo will retract and the coarse motor along the z direction will extend for 1 step. This procedure would repeat until the tunneling is established. To minimize the time for auto-approaching and avoid a tip crash at the same time, the user should use the coarse motor to bring the tip as close as it is still visually separated from the sample, then start the auto-approach. The Unisoku STM used in this work doesn't have a line of sight available for the sample region so the distance between the tip and the sample must be estimated by utilizing the electromagnetic induction coming from the AC current applied by lock-in amplifier. By increasing the amplitude of the function generator to a higher value (compared to experiments) like 1 V, the fluctuating magnetic field around the sample will cause enough magnetic flux leakage to the feedback circuit so that the in-phase signal read from the lock-in amplifier can be associated with the tip-sample distance. It is worth noting that the signal for approached position is depending on material type, sample heights and tip length. For the Au(111) sample, the typical target lock-in signal is at around 750 pA with 1 V amplitude at 977 hertz, but for some other 2D materials like $SnSe_2$, the target signal could be sitting at around 880 pA.

2.5 Scanning Tunneling Microscopy Methods

The scanning tunneling microscope is the main experimental instrument used in this dissertation. The operation of STM is based on the concept of quantum tunneling. By applying a bias voltage, the overlapping states between a sharp tip and the sample in close proximity enable

electron transfer through the vacuum via tunneling. The tunneling current is a function of the bias voltage V_{bias}, the LDOS of the surface, the work function of the tip, and the tip-surface distance. On an electronically uniform surface, the tunneling current I_t depends on tip-sample separation d exponentially as described:

$$I_t \propto e^{-2\kappa d}$$

In constant current mode, a tunneling current setpoint, proportional and integral elements of the feedback loop are set by user. Either the sample or the tip is grounded, and the other part is floating with a bias voltage, which can range from 10 mV to several volts based on the material studied. Governed by the feedback loop, the instrument scanner positions either the tip or the sample very close to each other to stabilize the tunneling current to the target setpoint. Then the scanner is rastered along the x and y directions to generate a topography based on the z position recorded at each raster point. The information in STM images can be interpreted as the combination of the electronic local density of states and the topological data of the surface, so sometimes it is difficult to assess topological features solely based on images due to the restriction of the tunneling condition. For example, an atomic pothole in the STM images looks like an atomic vacancy, but at different biases, it might appear to be an adsorbate. This is because tunneling microscopy doesn't measure the physical height directly but the perturbation of the electron density at the location where physical height is different from the surroundings. To extend the information collected from STM, it is essential to interpret the STM data accompanied by tunneling spectroscopy.

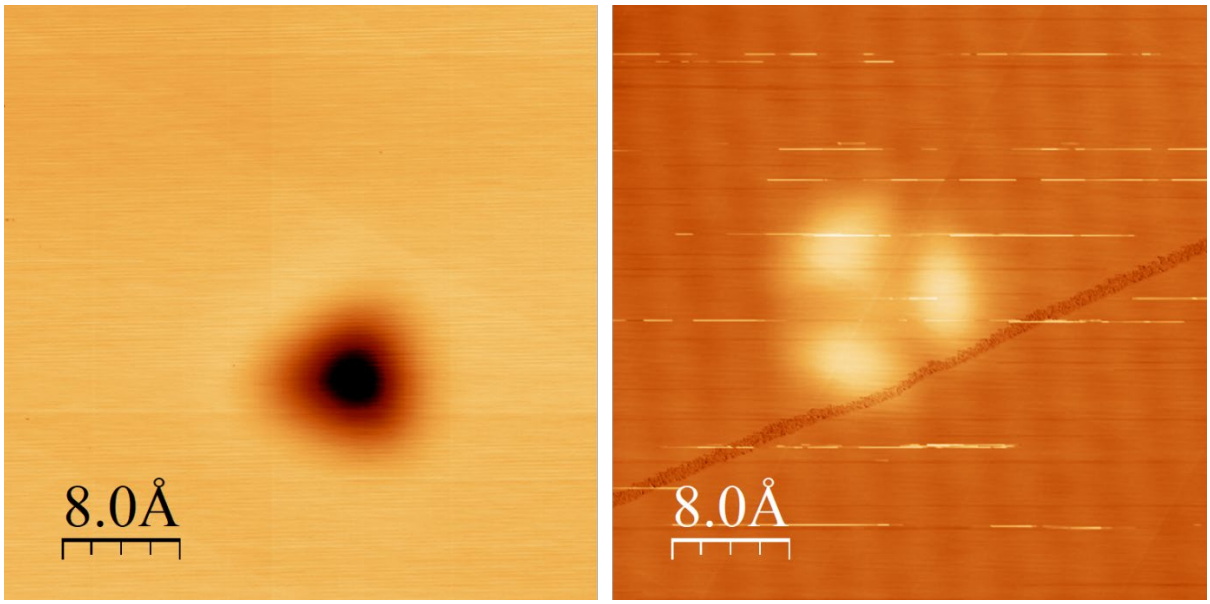

Figure 2-7. STM images of the same arsenic vacancy defect on $EuZn_2As_2$ taken at -1.5V (left) and 1.0V (right), respectively.

2.6 Scanning Tunneling Spectroscopy Methods

In most cases, the STS data contains the local measurement of the tunneling current versus tip-sample bias (I versus V, commonly referred as I-V) curve, and from the obtained I-V curves, the bandgap of the sample at the location of the I-V measurement can be determined. The derivative of the I-V curves (dI/dV versus V, common referred as dI/dV) gives differential conductance information, which is associated with the density of states of the surface at a smaller bias that is less than the work functions of the tip or the surface.[57] During the I-V spectroscopy, the feedback loop is turned off and the tip-surface distance is constant. By applying a voltage ramp on the tunneling junction, the tunneling current as a function of bias provides information that is a convolution of the tip DOS and the sample DOS. The bandgap of the semiconductor sample can be determined by plotting the tunneling current on a log scale versus the tip-sample bias. In addition to the well-known "point and shoot" STS collection method, spatial dI/dV maps can be

collected through two different methods. The first one is to utilize a lock-in amplifier to modulate the bias voltage with a low-amplitude sinusoidal signal which needs a higher frequency than the high frequency cutoff of the Z-piezo feedback loop.[58] The output signal of the lock-in is directly proportional to the dI/dV. The scaling factor is related to the amplitude of the modulation and can be calculated by dividing the derivative of the real I-V signal. Collecting STM images with the voltage modulation from the lock-in amplifier can generate spatial dI/dV maps simultaneously. The second method is current image tunneling spectroscopy or Continuous Imaging Tunneling Spectroscopy (CITS).[59] Fundamentally, the scanner will use the same grid and pixelation number as STM images but in addition to collecting current, height and lock-in output, an I-V spectroscopy curve is collected at each pixel to generate a hyperspectral image that can be sliced into multiple energy levels. This method takes significantly longer than the first one since the tip will stay at each pixel for 1-3 seconds depending on the spectroscopy setting. CITS images that contain more than 200×200 pixels will normally take more than a day, and one should expect finite levels of non-linear thermal drift-induced distortion in the image.

The analysis of STS is based on Bardeen's qualitative description of the tunneling process,[60] the expression for the tunneling current is:

$$I(V,x) \propto \int_{E_f}^{E_f+eV} \rho_s(E)\rho_t(e+eV)|M(E,V)|^2\, dE,$$

where I is the tunneling current density, E_f is the Fermi energy, ρ_s and ρ_t are densities of the electronic states of the sample and the tip, respectively. $M(E,V)$ is a transition matrix element defined by the overlapping of the tip and sample wave function which is described as:

$$M(E,V) = \frac{\hbar^2}{2m}\int(\psi_S^*\nabla\psi_T - \psi_T\nabla\psi_S^*)\, dA,$$

where ψ_S^* and ψ_T are the sample's and the tip's wave function, and A is the surface area within the tunneling region. However, the tip wave function is unknown in the experiment, so a simplified tip model can be used to interpret the experimental results on the fly. Tersoff and Hamann assume the tip has a spherical orbital and a flat DOS. When a low bias voltage is applied ($M(E,V)$ is constant), the I(V,x) equation can be simplified to:[57]

$$I(V,x) \propto \int_{E_f}^{E_f+eV} \rho_s(E)dE.$$

This approximation shows that the tunneling current is proportional to the local density of states (LDOS) near the Fermi level of the sample. By differentiating the equation, the dynamic tunneling conductance *dI/dV* is given, which reflects the sample LDOS as a function of energy:

$$\frac{dI}{dV} \propto \rho_s(E_f + eV).$$

Depending on the polarity of the bias voltage applied to the tunneling junction, the occupied and empty states of the sample can be accessed. It is important to state that the tip's DOS is not only constant in a real experiment, but also likely to change during a long experiment, which is important to acknowledge while interpreting simulated STM data based on the previous approximation.

Once the I-V and lock in dI/dV spectra are collected, they are normalized following the procedure first described by Prof. Randall Feenstra.[61,62] A normalized conductance, *(dI/dV)/(I/V)* , is computed by scaling up the lock in dI/dV to the same numerical level as the dI/dV from differentiating I-V spectra using a first degree polynomial function. This operation gives *(dI/dV)V* with a unit of Ampere since the scaling factor is directly proportional to the lock-in modulation voltage with a unit of Volt. Then the relatively high signal-to-noise normalized lock-in dI/dV

spectra are divided by the I-V curves to give LDOS with arbitrary units versus energy (eV, where $E_f = 0$). This procedure negates the dependency of tunneling transmission probability on tip-sample spacing and tip-sample bias, which in experimental reality are interpreted as the difference in starting point voltage bias and the setpoint current between spectra. This procedure is necessary even if all data are taken with the same setpoint and bias range to minimize the error generated by different tip states.

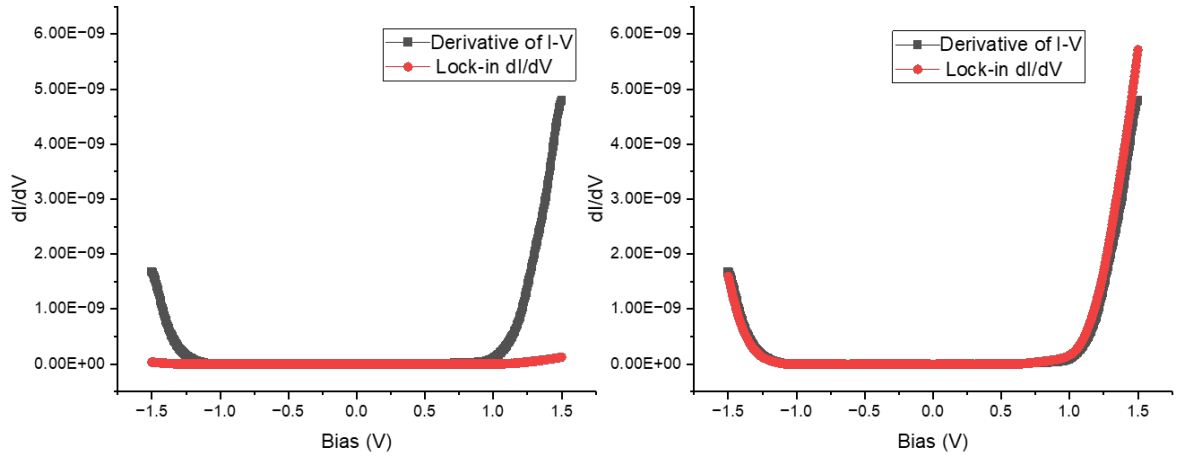

Figure 2-8. dI/dV data processing of $EuZn_2As_2$ As-Zn substitution defect. (a) dI/dV calculated from differentiating a I-V curve and dI/dV directly collected from the lock-in output signal. (b) dI/dV calculated from differentiating a I-V curve and dI/dV directly collected from the lock-in output signal with a first order polynomial function applied. The variable in the polynomial function is determined through weighted least χ^2 method.

The default normalization method works well on metallic samples where there are electronic states near the Fermi level, but for semiconductors, the I-V signals diminish within the stateless bandgap so that only electrical noise was collected. While dividing extremely small tunneling current values with random polarity within the bandgap, the LDOS plots are populated with positive and

negative spikes, which are shown in Fig. 2-9. To eliminate the I-V of two edges of the bandgap were fitted with the cumulative distribution function of the Gumbel distribution.[63]

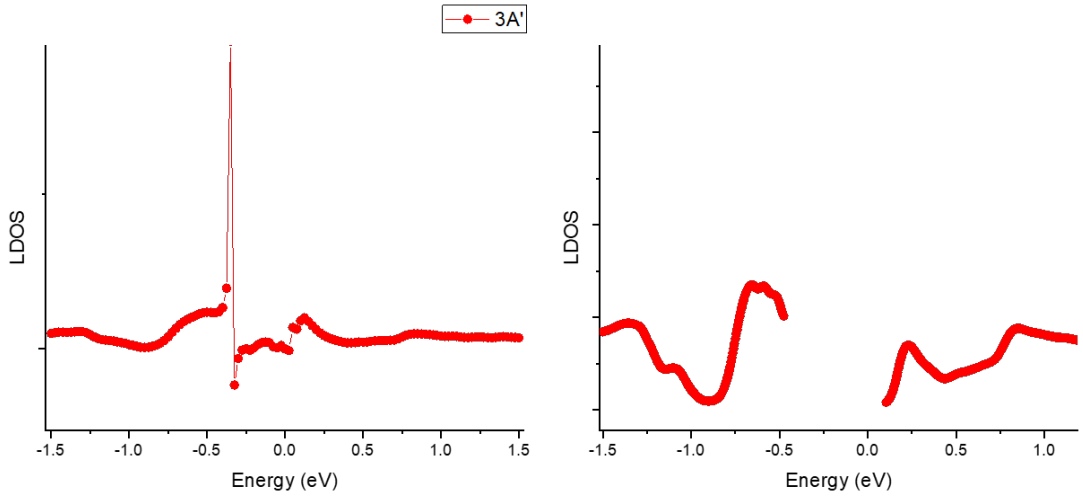

Figure 2-9. (a) LDOS from *(dI/dV)/(I/V)* versus V for a semiconductor. (b) LDOS calculated from (d*I*/d*V*)/(*Gumbel fitted I*/*V*) for a semiconductor. The data points within the bandgap are hidden.

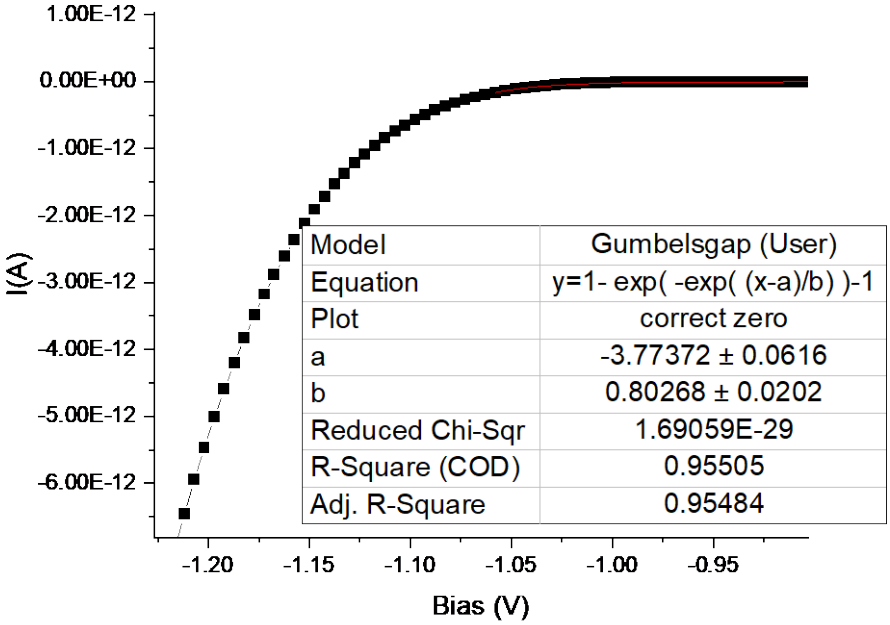

Figure 2-10. Semiconductor I-V curve fitted to Gumbel distribution from the edge of the bandgap to the Fermi energy.[63]

2.7 Quasi-particle interference (QPI) analysis

QPI or Fourier-transform scanning tunneling spectroscopy (FT-STS) is a technique to process the CITS data in order to yield simultaneous real space and momentum space information at different energy levels near the Fermi level. Due to matchless energy and reciprocal space resolution in QPI, it has been highly successful in unveiling the detailed dispersion relation and structure of the superconducting order parameter in many correlated electron materials.[64-67] The Jupter Notebook code for QPI analysis of CITS was obtained from Dr. Zheng Gai and modified based on the version developed by Dr. Qiang Zou. The first part of the code loads the CITS binary data file using an open-sourced package nanonispy. Then the subsection block plots the topography file in the data file and provides an option to select a rectangular region in the image

for the following process. Then, the averaged I-V, dI/dV, and the 2D-FFT of the topography are presented. A peak-finding algorithm that relies on scipy locates the reciprocal coordinates of the K-points in the lattice Brillouin zone, which can also be input by the user manually. The next block performs drift correction and symmetrizes the 2D-FFT on all dI/dV maps. The final outputs are plots of the dI/dV map, original 2D-FFT of the dI/dV map, symmetrized 2D-FFT of the dI/dV map, and the QPI map that plots the intensity of the FFT signal of the dI/dV map as a color map with energy and reciprocal position as X and Y axes, respectively.

2.8 Density functional theory

In collaboration with the Jin group and Mu group at the University of South Carolina, the STM/S measurements conducted on $EuZn_2As_2$ surface defects were analyzed with the assistance of first-principles density function theory (DFT) calculation. DFT is a quantum mechanical modeling method that utilizes functionals to approximate the exchange/correlation effect of the electronic structure Hamiltonian to calculate the electronic and geometric structure of many body systems. The calculation involves constructing the initial lattice cell based on educated assumptions from the experimental results. Then the lattice structure is optimized using the projector augmented-wave (PAW) method as implemented in the Vienna *ab initio* simulation package (VASP) including the spin-orbital couplings.[68,69]

The DFT-calculated structures at different bias voltages were visualized with using the p4vasp software package.[70] The simulation images are collected in constant height mode with a tip position ~ 5 Å away from the surface. Due to the nature of the periodic boundary conditions of the lattice structure, we selected the tip position across all biases and structures that gave the best similarity to the real STM images.

2.9 Low Energy Electron Diffraction (LEED)

Low Energy Electron Diffraction (LEED) is a surface science technique that studies the electron diffraction patterns arising from irradiating a crystalline sample with low energy electrons.[71] The electron gun irradiates the sample with a beam of electrons that are typically within the energy range between 20 - 200 eV. The reflected elastic beam and diffraction pattern electrons are selected as elastic ($\Delta E = 0$) and accelerated to a 6 kV fluorescent screen. The diffraction pattern observed on the fluorescent screen is a direct picture of the reciprocal lattice of the part of surface "under beam" and can be used to interpret the surface crystallography. However, a great diffraction pattern doesn't guarantee the whole sample has an ordered surface. In this dissertation, LEED was used as a complementary technique to STM to characterize the Pt(111) surface after the cleaning process.[72]

Chapter 3. Temperature-tuned Selectivity of the Initial Bond Rupture in Dissociative Chemisorption of a Branched Alkane on Pt(111) Investigated by Scanning Tunneling Microscopy

3.1 Technical Background

In a previous study by the Harrison Lab, Eldridge et al. have shown that Tetramethylbutane (TMB), an octane isomer, has a C-H and a C-C bond dissociation reaction pathways upon dissociative chemisorption on Pt(111), with activation energies E_a = 7.82 kJ/mol and E_a = 40.0 kJ/mol respectively.[10] This is highly interesting since the initial chemisorption by C-C bond dissociation on metal surfaces is rarely observed because access to C-C bonds is often sterically constrained from the surface and hence very little understood by the surface chemistry community. Weinberg *et al.* found initial C-C bond cleavage is more favorable over dissociative chemisorption by initial C-H bond cleavage for a number of alkanes at high temperatures on Ir(111),[73-76] Ir(110),[77,78] and Ru(0001)[74,79,80] surfaces, but no saturated alkane were found to have C-C bond cleavage pathway on Pt(111) prior to the previously mentioned work. In addition, Eldridge et al. also showed that by increasing the surface temperature to 1000K, which is a common condition for alkane to form graphene on Pt(111), the measured carbon coverage formed by TMB does not exceed 1.36 ML with respect to Pt(111), much less than the 2.58 ML coverage of graphene formed by ethylene.[10] The ongoing hypothesis is that initially, isolated graphene islands formed across the Pt(111) lattice from the chemisorbed carbon product. Once the graphene island starts to nucleate, they do not easily diffuse across the surface. As these islands propagate, they block more and more Pt from

impinging TMB, leaving significant gaps which could be occupied by carbon, but are not because (a) TMB is too large and cannot fit into the space to react and (b) the graphene islands do not easily diffuse or sinter. This hypothesis presents a potential method to grow porous graphene on Pt(111), leading to tunable specific surface area, mass density and accessible internal space. Porous graphene has extensive applications in making functionalized graphene products for CO_2 reduction,[81] nitroarenes,[82] and other hazardous pollutants.[83] A recent study on porous graphene nanoribbons synthesis with 2,2'-di([1,1'-biphenyl]-4-yl)-10,10'-dibromo-9,9'-bianthracene on Au(111) demonstrated successful STM imaging of a porous graphene layer.[84]

3.2 Experimental Methods

The experiments were performed under ultra-high vacuum (UHV) conditions with a base pressure of 2×10^{-10} torr using a Scienta-Omicron variable temperature scanning tunneling microscope (VT-STM) operating at room temperature. Tungsten tips were prepared by electrochemical etching. Prior to STM experiment, the Pt(111) single crystal was cleaned with the method described in Chapter 2.3, and left idle for the chamber pressure to return to the base pressure. Then, the desired dosage of TMB was introduced into the chamber through backfilling via a variable leak valve while the crystal was being heated to the dosing temperature. At the end of the dose, the variable leak valve was closed to reach the target exposure, and the sample remained heated until the pressure dropped below 1×10^{-8} torr. After the sample was cooled back to room temperature, it was transferred to the STM sample stage. The STM images were acquired in constant current mode at room temperature (~292 K). STM images were processed with Gwyddion and are plane-leveled.[85] The temperature of the crystal was measured by an infrared pyrometer and plotted against the heating power. Since the pyrometer is not sensitive to temperatures below 550 K, the Omicron

reference curve for the PBN heater plate was used for heating powers from 0-2.5 W. The temperature of the PBN filament and the surface of the Pt(111) are taken and shown in Appendix Table A. Per filament specification, the highest power output should not be more than 30 W, and the highest temperature that could be achieved at the crystal surface was ~1160 K.

3.3 Thermal Dissociative Chemisorption at 400 K and 790 K

The first condition used in the experiment was 33 L of TMB dosed at 400 K of substrate temperature, and the STM image of the surface after dose is shown in Fig 3-1. The image shows a very amorphous surface that shows a line scan with much higher roughness than an atomically flat Pt(111). One running hypothesis at that time was that the residual TMB gas was adsorbing to the cooling surface of Pt(111) and introduced severe tip imaging during the STM. The coverage was slightly higher than desired because the partial pressure of TMB in the chamber didn't decrease for an extended amount of time. At the end of the dosage, the variable leak valve to the TMB gas is closed and the heating on the Pt(111) decreases gradually. As a result, the Pt(111) was heated to 700 K on the VT-STM sample stage at 5 W (maximum on sample stage) for 5 minutes, and the STM images were taken after cooling the sample to 300 K. However, the previous temperature programmed desorption experiment of TMB on Pt(111) shows that TMB completely desorbed before 250 K, so it is unlikely that the tip imaging is induced by large physisorbed TMB/carbon island on the surface. Another possibility here is that the residual TMB gas in the vacuum chamber was picked up by the apex of the tip during the transfer process of the sample.

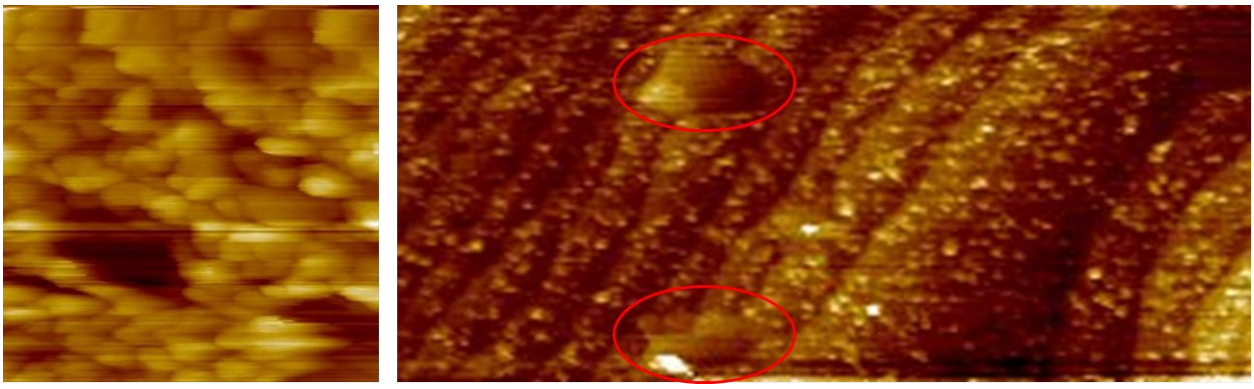

Figure 3-1. (Left) Amorphous surface after dosing TMB on the Pt(111) at 400 K. (400 × 400 nm) (Right) After annealing to ~650 K, the carbon island covered Pt surface emerged. Two large islands with non-atomic periodicity were labeled with red circles. (176 × 400 nm)

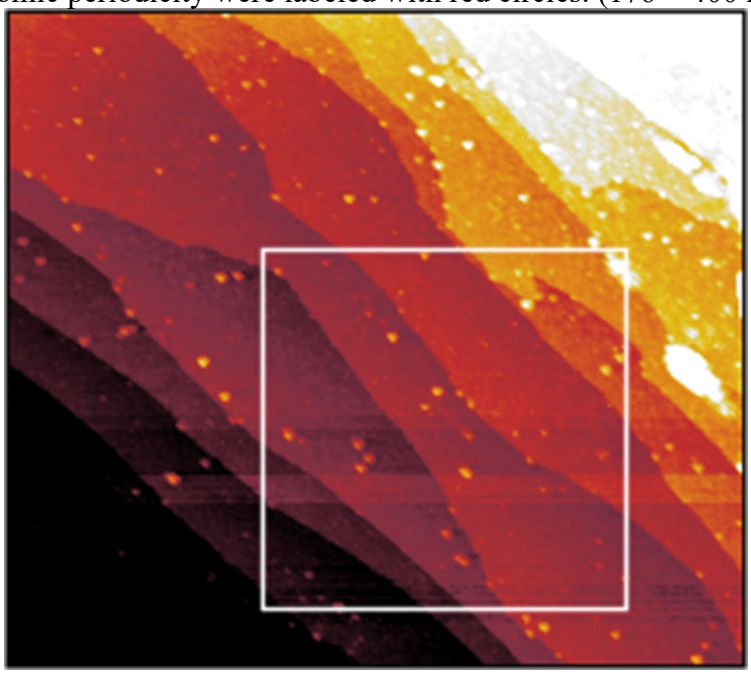

Figure 3-2. STM image of product of TMB dissociative chemisorption on Pt(111).

At 790 K substrate temperature, 0.66 L of TMB was dosed and the STM image of the surface after dose is shown in Fig. 3-2. The carbonaceous products of dissociative chemisorption can be seen on the surface, and they are stable over a couple hours of scanning. It was found that

two types of features exist on the surface, which were differentiated by their apparent heights, ~ 4 Å and 2 Å. The step height of the Pt(111) terraces were measured to be 3.0 ± 0.2 Å, which is within the acceptable range of errors to the measurement of 2.3 ± 0.3 Å in previous studies of Pt(111)[86] due to the default calibration of the piezos are normally done at low temperatures, so the measurement at room temperature tends to be higher. The ratio between the measured and expected step height was used to normalize the apparent height of the carbon islands. The group 1 island's height agrees with the diameter of a gas phase TMB molecule, which is 4.5 Å, and the group 2 island is about half of the size of the TMB molecule. This result reinforces the high-temperature trapping-mediated pyrolysis by Eldridge et al. and further shows that both C-C and C-H bond dissociation products exist on the surface after cooling down to room temperature at the end of the dosing.

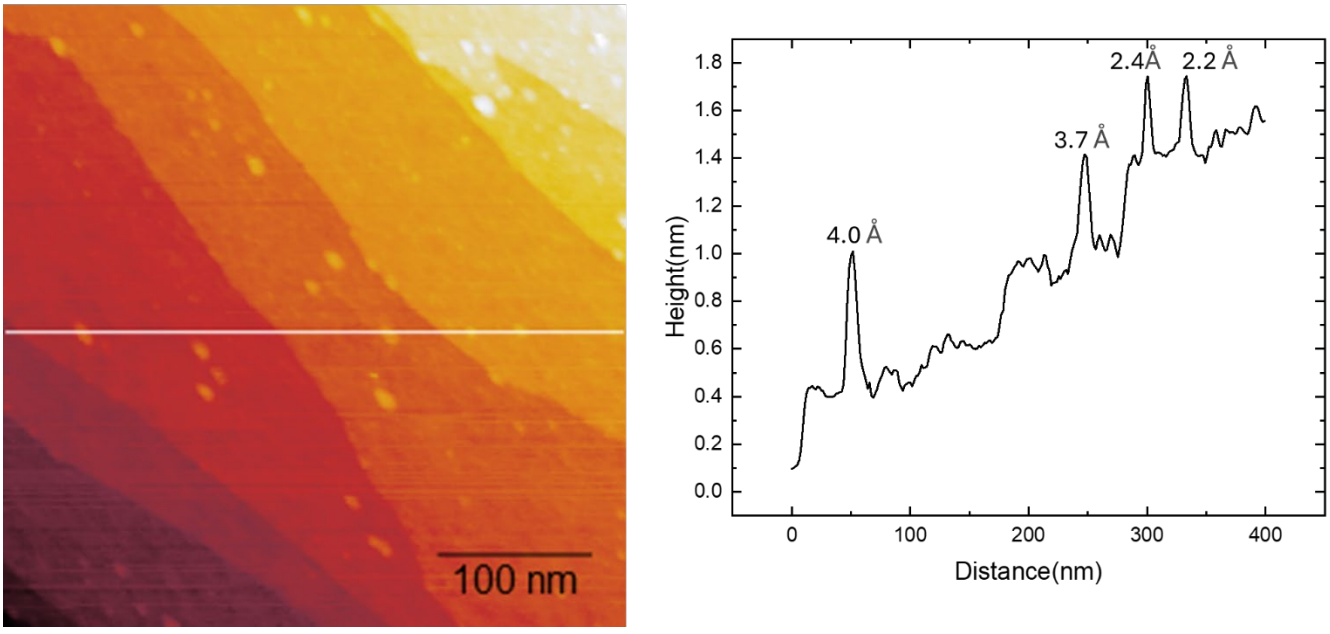

Figure 3-3. (Left) Enlarged STM image within the white rectangular area in Figure 2, and (Top Right) corresponding line profiles of two types of features indicated by the white line.

The coverage of the carbonaceous product was calculated through height segregation over each terrace and the percentage of surface adsorbates is 3.57%. Based on the thermal dissociative sticking coefficient measured in the previous study for this reaction, the expected coverage is around 0.03 ML. It is confirmed that the previous dissociative sticking coefficient is also observable through STM. It is worth noting that the coverage calculated based on the area in real-space images is subject to feedback loop settings and tip apex radius, which leads to features with higher apparent height appearing to be larger than their physical shape.

3.4 Future Direction

The current results are consistent with the existence of temperature-dependent C-C bond dissociative chemisorption pathways, but the observation of both types of C-C and C-H dissociative products indicates both pathways exist competitively and their weight changes as the temperature rises, which was predicted by *Eldridge et al.*. The room temperature STM study shows that imaging of dissociative chemisorption products is probable. However, to get a better understanding of the exact structure of the reaction products and TMB's potential to make porous graphene, low-temperature STM, with a CO-functionalized tip[87] might be required to more precisely examine the exact structures of surface products.

Chapter 4: Scanning Tunneling Microscopy Induced Defect Growth on CVT Grown TaS_2 Crystals

4.1 Introduction

In the pursuit of novel materials, transition metal dichalcogenides (TMDs) [88-90] have been extensively studied since they show great potential in optoelectronic devices,[91-93] sensors,[94,95] and energy storage systems.[96] In order to make both small and flexible semiconductor devices, a cost-efficient way to produce single atomic layers of TMDs at scale is warranted.[97] Additionally, methods for isolating, contacting, etching, and integrating TMDs are essential for successful device fabrication. Bulk TMD crystals can be grown using chemical vapor transport (CVT), which is a well-established method in the growth of high quality materials.[98,99] All two-dimensional materials, particularly those grown via CVT-grown, often contain point defects formed during the sample growth[92,100] or post-growth treatment, [19,26,101] which affect the properties of TMDs. While these defects can undermine the durability and consistency of materials, recent theoretical studies suggest that chalcogen vacancies introduce deep in-gap states and can serve as dopants. [20,102] It is, therefore, essential to study the relationship between growth conditions and defect formation to identify methods that support optimal device fabrication.

Confined by the van der Waals (vdW) gap between layers, atomically-thin TMDs can be exfoliated or removed from bulk TMDs through mechanical contact with adhesive substrates.[97,103,104] Previous studies have shown that a large-area of single atomic layers of TMDs can be exfoliated by tuning the chalcogen-substrate interaction,[45] and lateral features of a monolayer of TMDs can be patterned through laser-assisted exfoliation.[105] These methods are

promising in manufacturing single or few layers of TMDs at a large scale, but their performance of TMDs prepared in such a way can suffer compared to bulk materials or intentional single-layer growth. A alternative approach for modifying local surface morphology and introduce patterns required for device integration is based on single-layer etching via scanning probes.[106-112] This method has the potential to enable direct-write approaches to patterning. It was discovered that the surfaces of TMDs can be etched by scanning tunneling microscopy (STM), and several possible mechanisms were proposed to explain the tunneling current-induced etching.[107] Similar experiments done with AFM indicate that the participation of a scanning probe is necessary for surface etching, and the water concentration in the experimental environment dictates the etching rate.[108] An ultra-high vacuum (UHV) -STM experiment using tip-induced etching on $TiSe_2$ indicated that the growth of a vacancy island can be tuned by varying the tunneling current setpoint, and the etching can be halted by changing the bias voltage.[111] These studies laid a solid foundation for exploring tip-induced etching, but the kinetics of etching, etch rates, and mechanistic details of the process remain open-ended questions. Further observations of STM-induced etching are needed to provide deeper understanding of the kinetics and mechanisms, as well as to ultimately achieve control over the process. Ideally, tip-induced etching will be used to write device structures or patterns onto TMD surfaces with high precision and yield.

Similar to moving a single atom on the surface, the etching and/or restructuring of the surface can be a result of a combination of several tip-surface interactions including, but not limited to, vdW and electric force between the tip and surface, charge and energy transfer, and bond breaking through electron injection.[113] In this study, we selected the metallic 2H-TaS_2 platform to examine STM-induced surface etching, and the formation and growth of vacancy islands (VIs).

While etching has been reported for the metallic 1T-TaS_2 phase,[109] the hexagonal 2H phase, despite being more stable, has not been studied in this context. By investigating the etching mechanisms on the surface of bulk 2H-TaS_2, our goal is to identify the major contributing factors in large-area tip-induced etching and connect them to the intrinsic material properties.

In this article, we begin by assessing the native defects of 2H-TaS_2 grown by CVT, and then study the nucleation and growth of VIs using STM. We identify point defects and a unique set of linear defects near step edges and observe the tip-induced growth of VIs. By tracking the evolution of VIs over several hours, we extract detailed kinetics information. The evolution of the VIs was captured in time-lapse STM topography images, and image analysis of VI characteristics provides quantitative information on growth kinetics. These observations indicate that VI growth kinetics is independent of bias voltage and is likely coupled to native defects in the respective sample section. The interaction volume of the tip and the surface is discussed and local bond breaking and restructuring of the VI edge is proposed as the underlying mechanism for VI evolution. Small segments of TaS_2 can be moved by the tip and are subsequently reintegrated into the step edge, which is in line with edge restructuring and thus minimization of the edge energy.

4.2 Methods

Sample Preparation: 2H-TaS_2 single crystals were synthesized by chemical vapor transport (CVT) with iodine as the transport agent. A stoichiometric mixture of Ta and S was transferred into an evacuated 18 cm long, 10 mm inner diameter, 12 mm outer diameter quartz tube together with 7.5 mg/cc of iodine. Using liquid nitrogen, the volatile iodine was condensed with the powder at the bottom end of the ampoule during the quartz sealing process. To minimize oxide-based Ta growth, all sample preparation was done in an argon-filled glovebox to reduce the

presence of oxygen and moisture. Additionally, the quartz ampoule was purged and vented with ultrahigh purity argon gas to further reduce the oxygen and moisture content prior to sealing the ampoule. The sealed ampoule was then placed in a four-zone tube furnace and heated up to 950℃ and 850℃ at the charges zone and growth zone, respectively, for 12 days. The typical lateral size of the resultant flakes was 5×5 mm^2. The x-ray powder diffraction (XRD) pattern of the as-grown single crystal is well-matched with the International Centre for Diffraction Powder Diffraction File (ICDD PDF) card 04-001-0070 and confirmed the TaS_2 single crystal is crystallized in the hexagonal crystal structure with space group of $P6_3/mmc$. Energy-dispersive x-ray (EDX) elemental mapping showed that Ta and S are distributed evenly, and no other elements were detected except carbon and oxygen, whose presence is strongly believed to be from the vacuum chamber and subsequent transport through air. The concentration of the resultant flakes is $Ta_{1.02}S_{1.98}$, which is close to the nominal value.

STM measurements and image processing: The experiments were performed under ultra-high vacuum (UHV) conditions with a base pressure of 5×10^{-11} torr using a Scienta-Omicron variable temperature scanning tunneling microscope operating at room temperature. The TaS_2 flake was prepared by mechanical exfoliation in air immediately before being introduced into the load lock chamber (1×10^{-9} torr), and shortly thereafter into the STM chamber. The STM images were acquired in constant current mode at room temperature (297 K). Tungsten tips were prepared by electrochemical etching and the imaging directions are right to left and bottom to top. STM images were processed with Gwyddion and are plane leveled.[85] The vacancy island (VI) features were analyzed with two methods: marking the vacancy island perimeter by hand with subsequent analysis and labeling of the islands with Fiji[114] , and segmentation with Segment Anything,[115] and

subsequently area and perimeter were quantified in Fiji.[114] Both methods yield areas that are within the margin of error, and provided near-identical etching rate data.

Transmission Electron Microscopy (TEM): Scanning TEM (STEM) and electron energy loss spectroscopy (EELS) experiments were performed on a Nion aberration corrected UltraSTEM 100 operated at an accelerating voltage of 60 kV. The experiments were performed with a convergence semiangle of 30 mrad. A 2mm EELS aperture was used to maximize the analytical signal during acquisition with an EELS collection semiangle of ~48 mrad. 4D-STEM data was collected with a 2.5 mrad convergence angle.

4.3 Results and Discussion

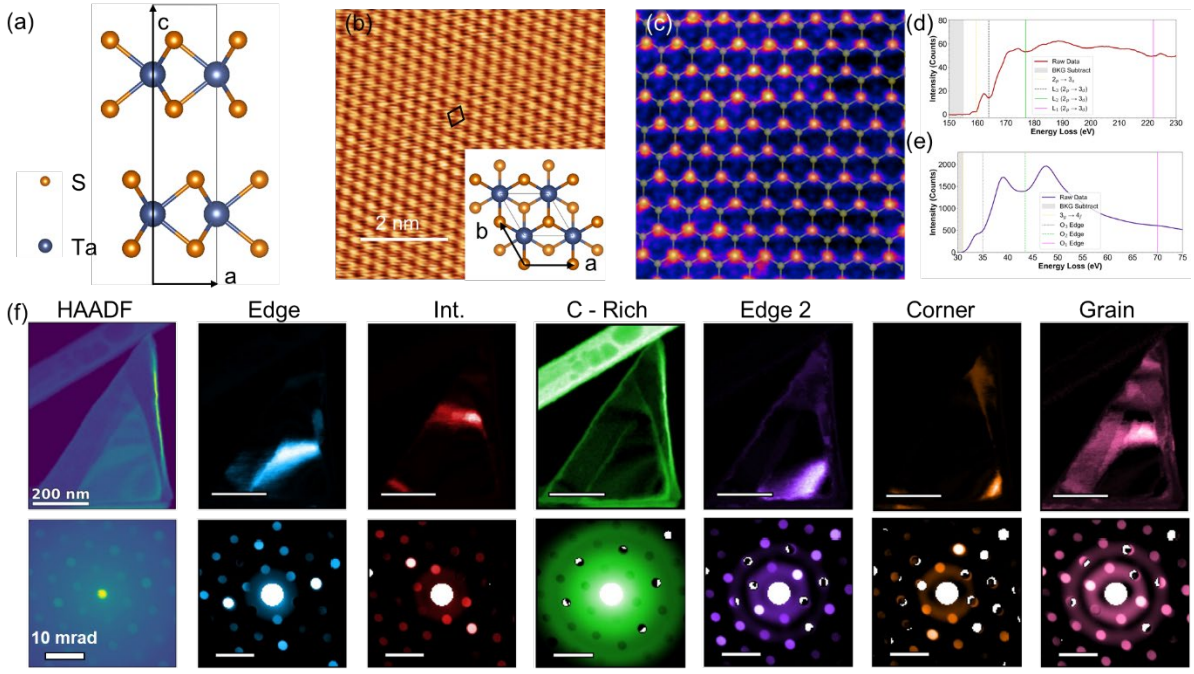

Figure 4-1. (a)The side view of schematic ball and stick model of 2H-TaS_2. (b) STM image after 2D FFT showing a parallelogram unit cell of 2H-TaS_2 sample. The a, b-plane top view of schematic model is shown as an inset. (c) Aberration-corrected STEM image of TaS_2 showing the short-range order and hexagonal lattice. (d) Ta O-edge and (e) S L-edge confirming elements present in deposited flakes. (f) NMF deconvolution maps of grains in a deposited sheet of TaS_2 with corresponding nanodiffraction patterns of the selected regions.

STM and scanning transmission electron microscopy (STEM) data on the pristine 2H-TaS_2 sample are summarized in Figure 1 and confirm the presence of the 2H polymorph. Figure 4-1(a) shows a structure model of this phase, and Figure 4-1(b) includes an STM image with atomic resolution and the *in plane* lattice constant of 0.34 nm from this image corresponds to the 2H structure unit cell.[116] An aberration-corrected high-angle annular dark-field STEM (HAADF-STEM) image is displayed in Figure 4-1 (c), with a transparent overlay of the molecular modeling image included to emphasize where the atoms are positioned in the lattice. In this Z-contrast based

imaging method, the "brighter" atoms represent Ta as they scatter more electrons at higher angles during electron beam interactions, and the S atoms appear dimmer as most electrons scatter at low angles from light elements.[117] Intensity variations confirm the composition of the film, and the atoms present were also verified qualitatively with electron energy loss spectroscopy (EELS), described later.

Figure 4-1(d) presents the 4D-STEM analysis. In this experiment, a converged beam of electrons is rastered across a sample in two-dimensions; thereby creating a two-dimensional diffraction at each location the beam sits in real space.[118] To interpret this dataset, we used deconvolution mapping in the form of non-negative matrix factorization (NMF).[119] First, the HAADF micrograph overviews a low-magnification image of the TaS_2 sheet with the corresponding averaged diffraction pattern from the spectrum image as seen in Figure 4-1(d). Next, since the layer was non-uniform in thickness, which is common in vdW solids,[120,121] NMF was used to decouple each of the "components" identified in the HAADF overview image into a mask and obtained the averaged diffraction pattern of each region. The "edge", of TaS_2 highlights some thick fringes in the film, and the "interior" is a mask between some regions of the layers. The "C-rich" region is masked from drawing analogs to the amorphous rings in the diffraction patterns and shows some carbon accumulation at the edges due to air exposure. The diffraction patterns were all oriented in the same direction, meaning the films were large single crystals. The intensity ratio of the diffraction peaks (inelastic: elastic) changes for each component, but the interpretation of this variation remains an open question. Since this is a layered solid these variations could represent disorder in the crystal, structure factor variations, or surface roughness which can affect the number of counts as the focal plane varies slightly between probe positions.[122] In Figure 4-

1(e) a core-loss EELS spectrum of the Ta O-edge is shown, and while the O-edges are not built for quantification, they are displayed here to verify the presence of Ta atoms. In Figure 4-1(f), the Sulfur L-edge is displayed verifying the preference of S atoms in what appears to be an S-rich films from the morphology of the dispersed flakes.[30]

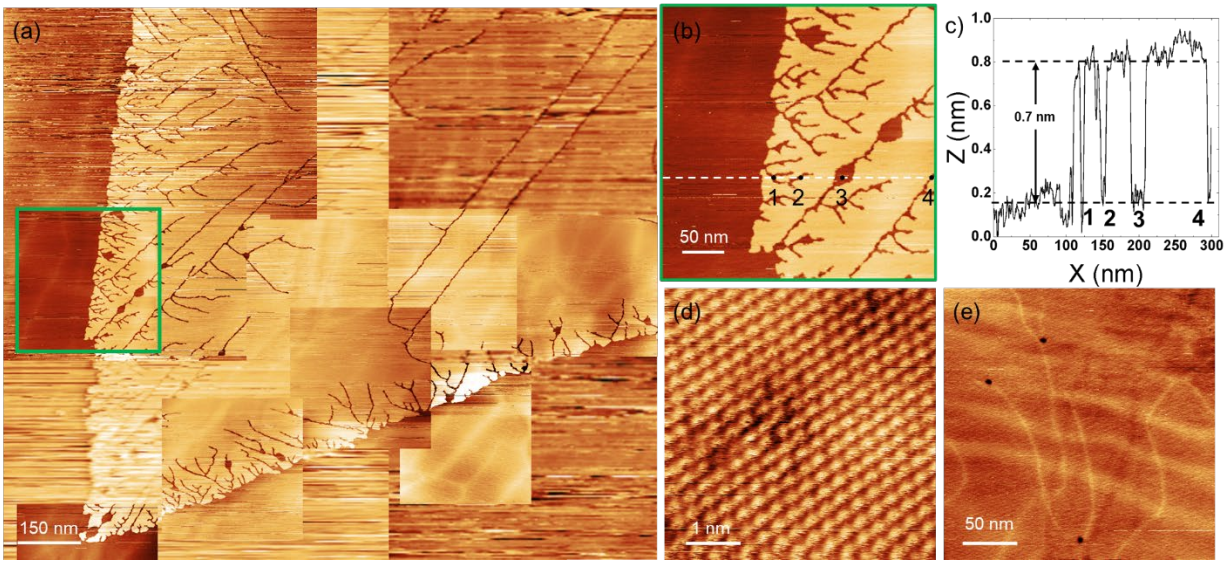

Figure 4-2. (a) A large area composite STM image of TaS2 showing the morphology of a surface island with characteristic defects around the step edge. (b) an STM image showing linear defects on the right side of the image. V_{bias} = 1.0 V, I_t= 20 pA. (c) Line profile taken across the white dashed line in (d). (d) Atomic resolution after 2D FFT filtering with point defects. V_{bias} = 0.1 V, I_t= 350 pA. (e) Subsurface defects from different layers. V_{bias} = 1.0 V, It= 200 pA.

Figure 4-2(a) shows a large area STM image 1000×1000 nm^2 of 2H-TaS_2, illustrating the general surface morphology of the sample in a region with high defect density. The image includes a monoatomic step, and the top layer has the typical triangular shape of transition metal dichalcogenide islands imprinted by the underlying crystal symmetry. The topography image is composed of a large area image on which several higher resolution images are superimposed. The step edge of the island shows a large density of linear defects which are visually reminiscent of

fracture cracks. The shape of these linear defects indeed resembles drainage system patterns in geomorphology maps. These defects can be seen on multiple occasions while surveying large sections of the sample surface. This supports their interpretation as defects caused by the specific reactions in the CVT growth process and is most likely related to the presence of iodine flux agents. The density of the linear defects in Figure 4-2(a) is reduced with distance from the island and step edges. The longer linear defects propagate mostly at angles of about 60° with respect to the island edges and are frequently interrupted by "holes" in the top layer, which can undergo branching. Figure 4-2(b) shows a topography image with a more detailed view of the linear defects, and the line profile was taken along the white dashed line and is included in Figure 4-2(c). Positions 1 to 4 correspond to linear defects and the height difference over the linear defects is 0.7 nm, which is equivalent to the step edge height of one S-Ta-S layer. It is worth noting that we did not see any linear defects during the STEM survey but it is admittedly difficult to find 1D linear defects in a 3D sample with the added challenge that the linear defects might be more prevalent in the near surface region. It is also possible that the line defects are subjected to clustering during the growth, both horizontally and vertically. New areas grown directly on top of defected areas are more likely to contain defects but less likely to have defects over a perfect area. This is because certain defects tend to propagate vertically (from layer to layer) during the CVT growth. This was revealed during the layers' removal by tip etching, presented later in this article.

Several point defects are visualized at atomic resolution and are shown in Figure 4-2(d) with the depth profile confirming the presence of a vacancy. Figure 4-2(e) highlights a segment of Figure 4-2(a) where brighter features, which resemble the linear surface defects from Figure 4-2(a) in shape and extension, can be directly observed. Unlike the linear defects at the surface which are

present as grooves, these structural inhomogeneities do not exceed one atomic height and appear as apparent protrusions. The surface morphology is preserved and these linear defects are interpreted as being sub-surface features from linear defects which were overgrown during the CVT growth process. The subsequent etching experiments illustrate their vertical correlation through several TaS_2 layers. Some round VIs are located directly above the sub-surface features, mostly at branching points, and might later serve as nucleation centers for VIs. The defects presented in Figure 4-2 were stable during more than 24 hours of STM imaging. This particular set of images was acquired immediately after baking the chamber and the tip. Subsequent experiments required the introduction of new tips without the baking of the chamber. Adsorbates, such as water, might accumulate on the tip or the sample surface due to the transfer-related pressure variations. These are small concentrations of adsorbates but can introduce variations in the etching efficiency and modify the tip-surface interactions.

In subsequent experiments, it was indeed observed that surface etching and growth of VIs can be induced by scanning and imaging with the STM tip on 2H-TaS_2. We describe here the emergence of VIs, their coalescence and growth, and the removal of entire TaS_2 layers through interaction of the surface with the STM tip. VIs appear and grow during extended periods of imaging and this process is tentatively tied to (i) an abundance of surface defects such as point defects, linear defects, step edges, and small VIs or defect clusters which serve as VI nucleation points, and (ii) the presence of adsorbates such as water at the STM tip, which can then participate in the electron-induced chemical reaction of TaS_2 to a volatile reaction product. A quantitative analysis of the images, as described in the method section, is used to determine the growth rates of individual, isolated VIs, and coalescence events. An extended set of image stacks to illustrate

different scenarios of VI formation is included in the Supplemental Information and references throughout the manuscript.

Here we present the data and the analysis for images with sufficient quality for quantitative analysis was feasible. The tip was scanned over an area of 800 ×800 nm^2 for more than 48 hours in total. Five layers of TaS_2 were removed within the scanner area over this period of time and removal occurred by nucleation and growth of VIs – an inverse of the growth process. Due to the constant change of the tip state in this process, the images tend to be rather streaky, which is a substantial challenge for tracking the individual features especially at the beginning of the experiment when many VIs were nucleating simultaneously. This is seen in the Graphic Interchange Format (GIF) stacks of some of the etch sequences, which are included in the Supplemental Information Figure S1-3, Figure S4, and Figure S5. For the quantitative analysis of VI growth kinetics 8 VIs were selected which are well isolated from other islands, do not undergo coalescence within the data range, and whose images include a sufficient number of frames with consistent image quality for quantitative feature analysis.

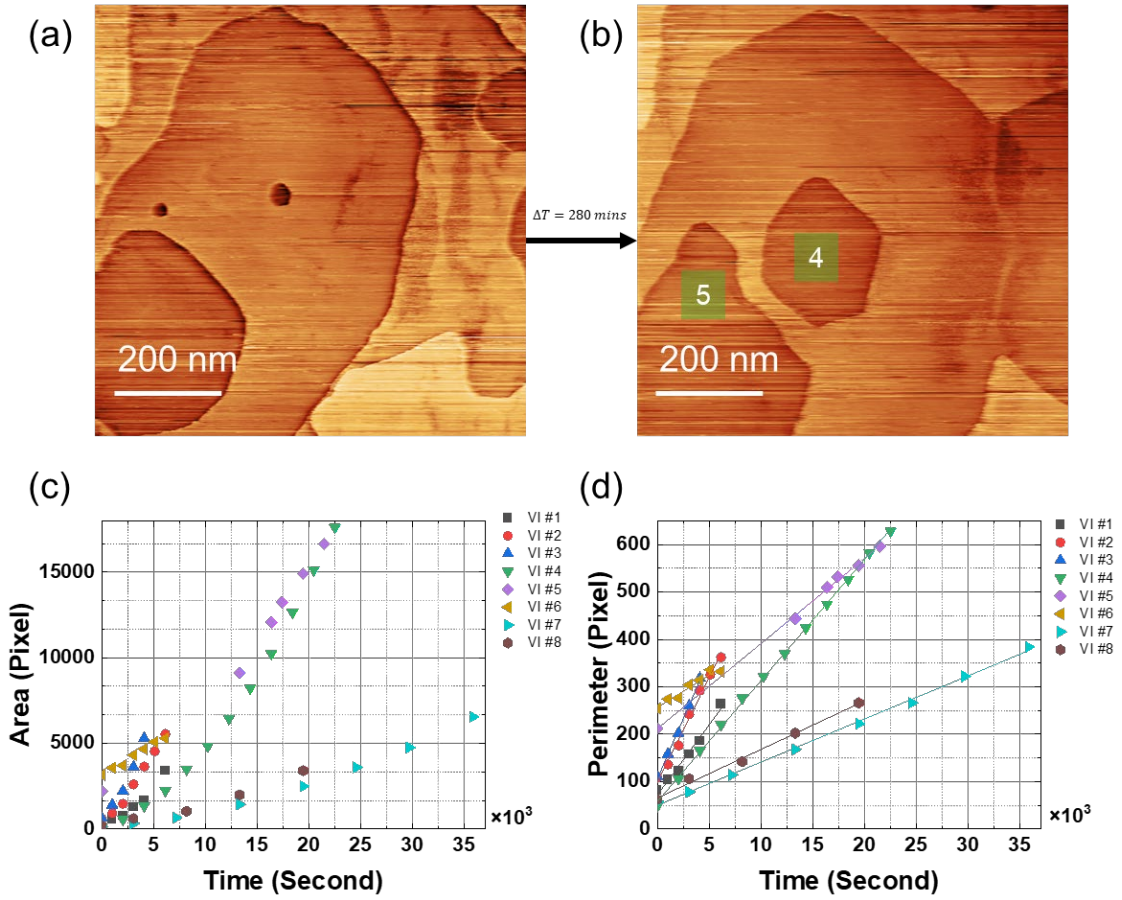

Figure 4-3. (a) and (b) Two STM images of an emerging vacancy island (No. 4 in the subsequent analysis) in the middle of the image. These two images are 244 minutes apart. (c) Area progression of 8 different vacancy islands. (d) Perimeter progression and linear fits (dashed lines) of 8 different vacancy islands.

Figures 4-3(a) and (b) show an example of an isolated vacancy island (this island was assigned as number 4) at the center of the images which was selected for the study of its growth kinetics. All selected isolated islands were tracked, and their area and perimeter progression were plotted against time in Figures 4-3(c) and (d). The perimeter data were fitted with linear functions and yielded an $R^2 > 0.99$ and the slope represents the VI growth rate. Perimeter and area are given in units of pixel where one pixel corresponds to 1.56 nm, and 2.44 nm^2, respectively. The growth

rates vary between VIs but they are surprisingly insensitive to imaging conditions. To understand the effect ouf tunneling conditions on the VI growth rate, changes in bias voltage were initiated during the growth of specific VIs, which is shown in Supplemental Information Figure S6, and in Tables S1 and S2. The variation in bias voltage between 0.5 and 1.5 V did not influence the VI growth rate. However, to limit the number of variables, the same imaging conditions were maintained for most of the experiment. The initial size in the first image recorded for a VI does not correlate with the growth rate either: VI#6 has a growth rate close to VIs #4, #8, and #7 but begins with a much larger initial area.

At first, the isolated and small VIs present in a shape close to a circle, and as the area of the islands increases, a hexagonal shape becomes clearly defined as seen in Figure 4-3(b). The hexagonal shape becomes evident when the area of the VI is about 3% of the total area of the image. Since 2H-TaS_2 is in the $P6_3/mmc$ space group the hexagonal vacancy island shape is indeed expected and minimizes the boundary energy of the perimeter. The thermodynamically preferred hexagonal shape is disrupted during coalescence events or in the vicinity of defect sites which pin the VI boundary which is discussed in Figures 4-4 and 4-5. This leads to a wide range of VI shapes, and all of the VIs will eventually merge with other VIs and finally, a complete layer will be removed.

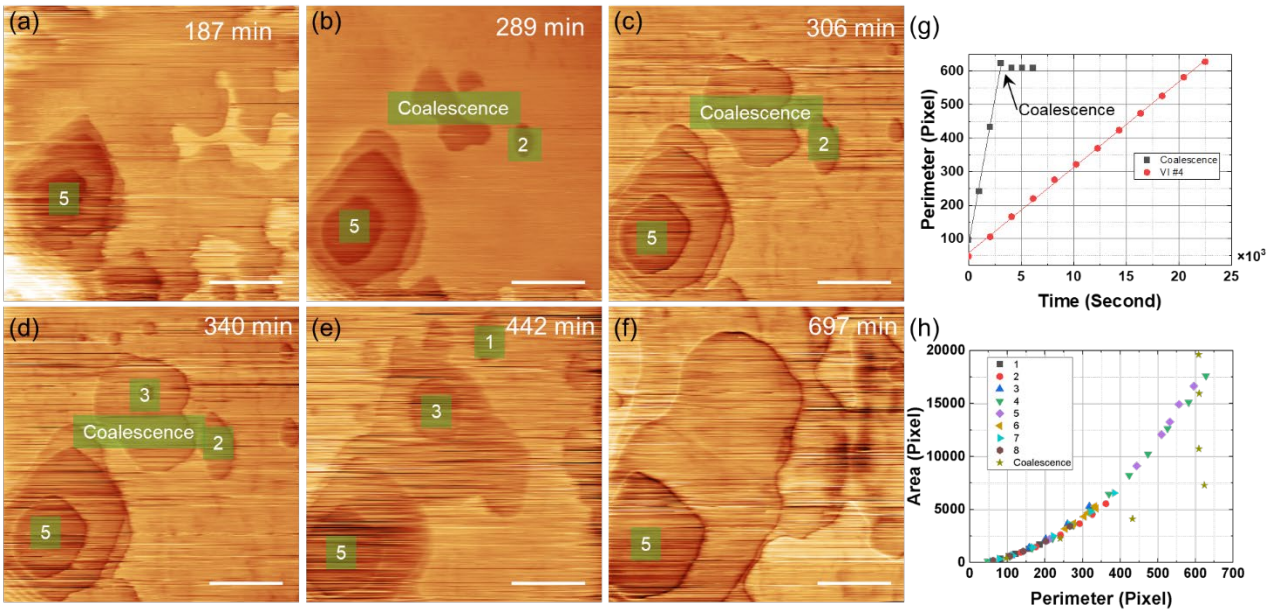

Figure 4-4. (a) – (f) Sequential STM images over the same area showing several individual vacancy islands as they coalesce into one. Time intervals since the start of the collection. V_{bias} = 0.5 V, I_t= 20 pA. Scale bar = 200 nm. The vacancy islands that were extracted are labeled with numbers with green background. (g) The comparison between the total perimeter over time of coalescence islands and an isolated island. (h) The area versus perimeter for all the vacancy islands analyzed

Figure 4-4 illustrates the growth and coalescence of VIs in a single set of images. Islands VI#3 and #2 in Figure 4(a) –(f) undergo coalescence and were added to the analysis of isolated islands. This is the same experiment series used in Figure 4-3 and Figure 4-4 and the numbers refer to identical islands. In Figure 4-4(a) – (f), a series of STM topography images with multiple coalescence events is presented. Two batches of islands in Figure 4-4(a) – (f) originate from similar locations across multiple layers: one being roughly the center of the image where coalescence happened first; the other at the bottom left corner labeled VI#5, which in the end coalesces with (VI#2+VI#3). The VI#5 is originally "stacked" three layers deep and is the result of a previous

series of scans observing VI evolution in the vicinity of closely aggregated step edges (Supplementary Information Figure S1). In addition, a sub-surface line defect is uncovered at the end of this series and marked for t=679 min at the right-hand side of the image. The pinning of the recession of the TaS_2 layer at this sub-surface line defect is shown in more detail in Figure S3 of the Supplementary Information.

The area and perimeter progression of a coalescence event between VI#2 and VI#3, and the growth of several isolated islands are plotted in Figures 4-4(g) and (h). For the isolated VIs area and perimeter follow their set geometric relation and all data sets collapse onto a single curve. In the case of coalescence, the VI area continues to increase but the perimeter is near constant. This is commensurate with the minimization of the line energy represented by perimeter length as the driving force for coalescence. The area vs. perimeter plot in Figure 4-4(f) also shows that Vi#2 and VI#3 follow the trends appropriate for isolated islands before coalescence. But before the coalesced island VI#2+VI#3 can reach the optimized hexagonal shape which would further reduce the line energy, it coalesces with VI#5 and several other small VIs for near complete removal of a layer within the scan area. Delawski and Parkinson's observations on $SnSe_2$ with AFM tip-induced etching, on the other hand, present a non-linear increase in the perimeter but the area of the VIs goes through a maximum.[108] However, the number of coalescence events is larger than in our case and caused by a significantly higher density of pit-forming events. In contrast, our work shows relatively sparse pit nucleation density and concomitantly fewer coalescence events. Hence the VI growth where perimeter and area are related by the geometric formula of a hexagon dominates for many VIs. Note that on some areas of the sample, a rapid pit growth is seen and paired with

frequent coalescence extending over several layers of TaS_2, which does not allow for a reliable quantification of growth kinetics.

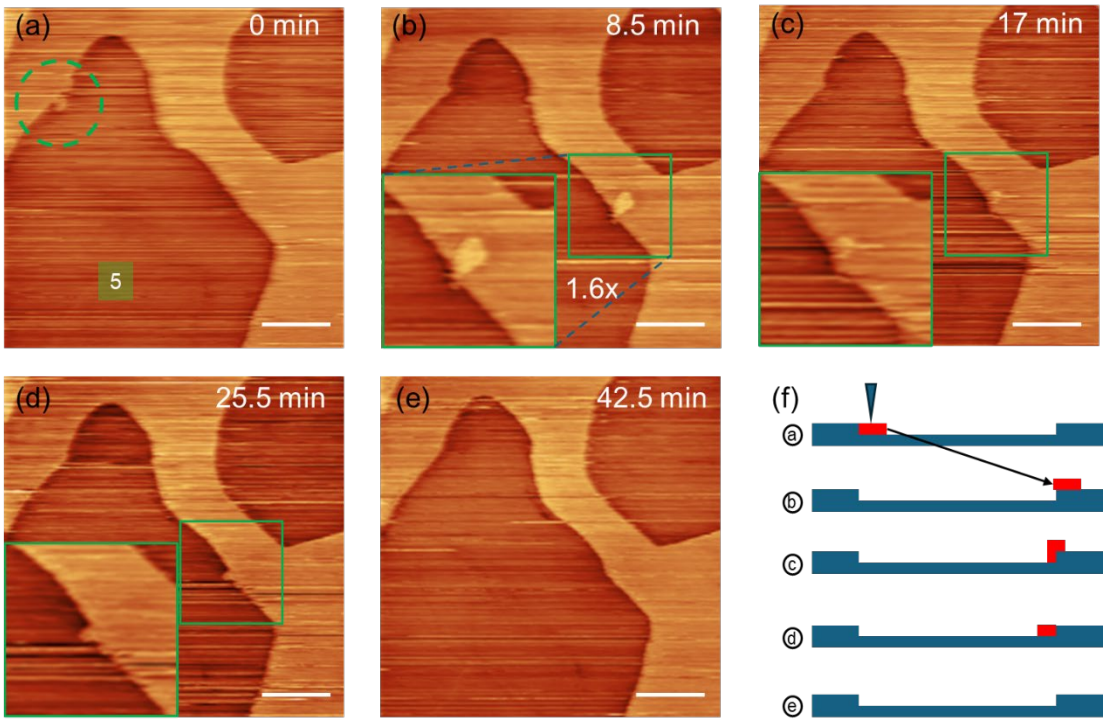

Figure 4-5. (a)-(e) Sequential STM images showing a TaS_2 island moved by the STM tip during scanning and recombining with the layer below it on the step edge. Scale bar = 50 nm. For (b) – (d), zoomed in images focus on the TaS_2 island are inserted as insets. (f) A schematic representation of the moving island (red) and the two stationary layers of TaS_2 (blue).

In addition to the etching events, it is also observed that small TaS_2 islands can break off from the large "continent" on the same layer and redeposited on another section of the layer. These small islands become more mobile and then can be moved by the scanning probe. This is shown in Figure 4-5 where a small TaS_2 island (~ 300 nm^2) was detached from one step edge and moved to the top of another one, which is inside of VI#5 island. A cartoon showing the relative vertical position of the moving island (red) with respect to the stationary layers of TaS_2 (blue) is pictured

in Figure 4-5(f). In Figure 4-5(a), the island is seen attached to the top left side of the vacancy island, and the TaS_2 island was moved on top of the right side of the vacancy island sitting now on the step edge. From Figure 4-5(c) to (e): in Figure 4-5(e), the "mobile" island has merged with the step edge underneath. This shows another type of tip-induced reaction, where a nanometer sized piece is moved across the surface and reverses tip-induced etching locally. It is worth noting that the timeframe for this process is shorter than the time marks on the image which relate to time at the start of each 800×800 nm frame, and only a small portion of this time contributes to the moving of the island (less than 100 nm). It is particularly interesting to see that the nanosized islands is fully integrated in the edge of the VI in Figure 4-5(e) which indicates a significant driving force towards edge faceting and mobility of TaS_2 molecules or fragments. And while we see in these images the motion of a nanoscale piece of material it can conjecture that smaller fragments can also be moved through the tip interaction. Hence not only does the electron-induced bond breaking play a role in the surface dynamics of VI nucleation and growth, but tip-induced surface diffusion is a significant contributor to the process.

The interaction between the tip and the surface can lead to the nucleation of VIs, which undergo growth and coalescence events during continued scanning of the surface. The shape for VIs is hexagonal if the islands are isolated and can adopt various geometries following coalescence events. The edges of VIs restructure over time approaching the preferred hexagonal edge termination as prescribed by the underlying hexagonal structure. The emergence of triangular or hexagonal VIs and etch pits have been described for several TMD materials,[108,111,123] and can consist of metal or chalcogenide-terminated facets. The edge re-faceting is seen particularly well in Figure 4-5, where a small TMD fragment dislodged by the tip is incorporated in the step edge

after several imaging cycles. The significant "streaking" of the images during scanning is an additional indication of the rapid and facile diffusion of TaS_2 fragments on the surface. Over time the VI growth leads to the removal of complete TaS_2 layers within the scan area while the region outside the scan window remains unchanged (Supplemental Information Figure S2). This is important for the control of patterning of TaS_2 for nanoscale device fabrication and processing.

The VIs tend to nucleate at defects such as the line defects which figure prominently in Figure 4-2, and S9 (section S6) in the Supplemental Information, or at multilayer steps shown in Figure S1 in the Supplemental Information. It is very likely that many of the VIs originate at point defects or defect clusters on the surface, albeit the larger scale images do not provide direct visual confirmation. The growth rate was determined for isolated islands for a total of 8 VIs during different stages of scanning and varies by at most a factor of four between islands when comparing the rate of perimeter growth. The number of islands which are amenable to this analysis is relatively small since coalescence is a frequent event. Interestingly coalescence leads to a rapid increase in area while (nearly) conserving the perimeter length in accordance with an Ostwald ripening mechanism. Initially, the perimeter of coalesced islands is not faceted, and faceting of the step edges to minimize the line energy occurs on a longer timeframe. Note that "rearrangement" here can be achieved by local detachment or attachment of molecules that are mobile on the surface.

From our observations, we can now develop a mechanistic model for the tip-induced etching of 2H-TaS_2. Each pixel in an 800×800 nm^2 image corresponds to 2.44 nm^2 and 25 unit cells of 2H-TaS_2, whereas each side of the pixel of 1.556 nm length is occupied by 4.7 unit cells.

To achieve an increase in perimeter with a rate as recorded for VI#4 (Figures 4-2 and 4-3) about 40 pixels corresponding to about 200 unit cells have to be removed from the entire perimeter per pass with the STM tip (or per image). Interestingly the rate of VI perimeter increase does not depend on the initial size of the VI measured, a clear correlation with the imaging conditions cannot be established, and no directional dependence of the etch rate with respect to slow and fast scan directions is evident. We therefore propose that the etching itself is initially a local event where a TaS_2 molecule or fraction of such a molecule is removed from the perimeter of a VI through initiation of a local bond breaking most likely triggered by the tunneling electron. The presence of defects will lower the activation barrier and therefore promote the nucleation of VIs. This model is commensurate with our assessment on the rate of removal of molecules from the perimeter of the VI. This assumption is commensurate with prior observations by Parkinson et al.[107,108] and the strong dependence of tip-induced etch rates on the respective TMD.

However, the variability in etch rates between isolated VIs quantified in Figure 4-3 remains an open question. The sensitivity of the process to relatively small variations in "vacuum quality". Our very first scan of the surface which was performed immediately after chamber bake-out including the tip showed a rather stable surface, and VIs did not develop over several hours of imaging. Any subsequent imaging was done at a later time, when the tip needed to be exchanged, and despite the use of a load-lock minute amounts of water are likely to accumulate within the chamber. We propose therefore that water adsorbates, even in small amounts, contribute to accelerating etch rates significantly. It is known for other systems that small amounts of CO, for example, can dramatically change growth and reaction pathways. Specifically for TMDs, the reaction of the step edge with water is rapid and has been used to "carve" triangular defects and

VIs and even large trenches into MoS_2.[123] Another scenario is that the density of defects as VI nucleation sites may vary across the surface and contribute to accelerate etch rates. This can only be resolved if we manage to record the defect inventory without triggering VI nucleation. Finally, the cross-talk between adjacent VIs, terraces, and features on the surface can control the concentration of molecule molecules on the surface by acting as sources or sinks. This in turn controls not primarily the etch rate of the tip but the recombination rate at the perimeter. In general diffusion lengths on 2D material surfaces are relatively long on the terraces and as such cross-talk can extend far beyond the imaging range captured with the STM. The pinning of the VI perimeter at a sub-surface line defect shown in the Supplemental Information Figure S3 might be a consequence of a modification of the molecule mobility on the surface. It is not known whether etched molecules can desorb from the surface or, alternatively, remain on the surface forming what might be described as a "molecule gas".

Each of these processes can be tested individually and further experiments will lead to a better quantitative description of the etching process. This is needed to establish tip-induced etching as a process suitable for deterministic pattern writing toward building TMD heterostructures and achieve integration with other processes on the path to 2D materials based device architecture.

4.4 Conclusion

In summary, the combined STEM and STM studies reveal the unique intrinsic defects in the CVT-grown 2H-TaS_2. The linear defects are associated also with sub-surface structures which

suggests that the CVT growth process can lead to clustering and propagation of defects. The tip-induced nucleation and growth kinetics of VIs are quantified using AI-assisted thresholding methods. The growth kinetics of VIs are discussed, and several mechanisms and reaction pathways are discussed. It is concluded that minute amounts of water play a significant role in VI growth. In addition, significant cross-talk between adjacent VIs likely exists due to long diffusion paths of TaS_2 molecules and fragments and serves to modulate the VI growth kinetics. Our findings reveal key elements to fast tip-induced etching and new potential methods for 2D material manipulation with STM.

4.5 Supplemental Information

S1 Stacked vacancy islands (VIs) and bunched steps generated by STM etching

At the initial stage of the experiment, after rapid etching of the surface material was observed, we interrupted the scanning and reduced the image framesize from 800×800 nm^2 to 200×200 nm^2, and then scanned at the reduced framesize for about 3.5 hours, and finally switched back to 800×800 nm^2. Comparison between the images before and after the switch, plus the images collected at 200×200 nm^2 are shown in Figures S1-1 and S1-2, and S1-3 which includes a GIF set up from a complete STM image set to illustrate the surface evolution over time. A square of etched area that corresponds to the 200×200 nm^2 frame is marked in Fig. S1c which was recorded after returning to the larger image size. The image drift for this experiment was about 0.038 nm/s and is indicated by the green arrow, and exacerbated by switching image dimensions. Therefore the smaller image square marked in Figure S1-1(b) is not at the center of the frame. Figure S1-1

includes the 800×800 nm^2 image at the start (a) and end (b) of the experiment with the smaller image frame measurements measured between the two. The increase in VIs throughout the experiment is evident and shows increase in the size, and number of the VIs with multiple coalescence events. Unique to this series is the depth of the VIs in the vicinity of the bunched steps labeled K1: a VI at least 5 layers deep develops in its vicinity. The "stacking depth" in this VI is unusual – most VIs on a terrace are only one or two layers deep with sequential removal of layers. This is indicative of an easier nucleation of VIs close to multi-layer step edges. Figure S1-2 shows several images (a) to (e) extracted from an image stack of 17 images included in the GIF file. From figure S1-2(a) to (b) nearly a complete TaS_2 layer is removed around the feature B2 (sub-surface defect) after coalescence of several islands. The VI then grows quickly and the image drift now allows us to see the increase in step bunching around B1 and K1 (see legend for features in the figure). Continued imaging clearly leads to rapid increase in the step bunch slope through reduction in the associated terrace width: etch rates along the step edges is high, and numerous VIs nucleate close to the step bunch. This leads to a deep trench which is seen in Figure S1-1(b) after the increase of the images size to capture the larger region around the step bunch.

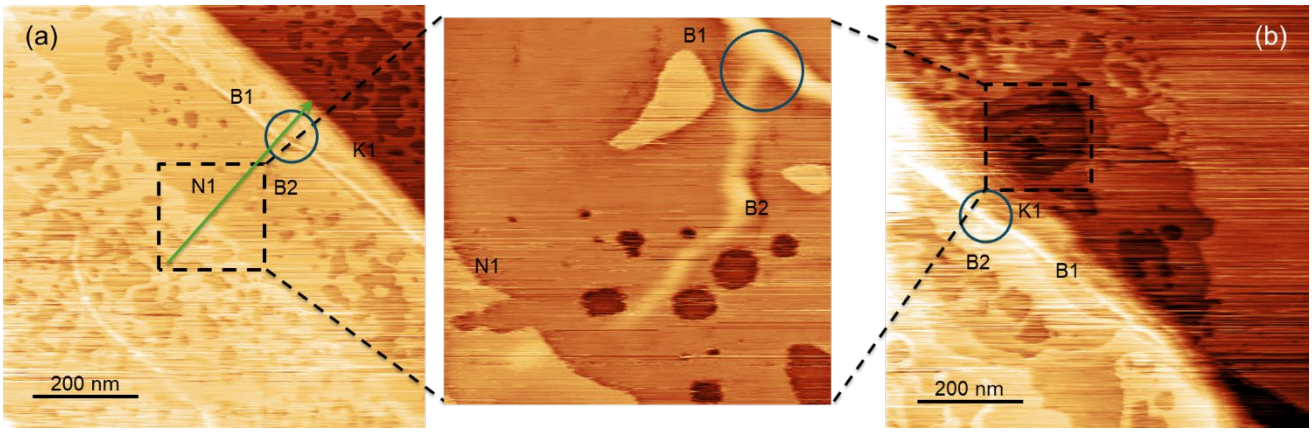

Figure S1-1: (a) STM image that shows large numbers of VIs formed in the first hour of the experiment scanned at larger image size. The black dashed square indicates the subsequent scan area after the scanner size was changed to 200×200 nm^2. (V_{bias} = 1 V, I = 50 pA). (b) After returning to 800×800 nm^2 scan area – the square indicates the position of the smaller image frame at the end of the sequence. Labels: B1 and B2: sub-surface defect lines, N1: notch in step edge, K1: bunched steps; Broken lines: (a) First image frame position, and (b) last image frame position; Green arrow: direction of the thermal scanner drift

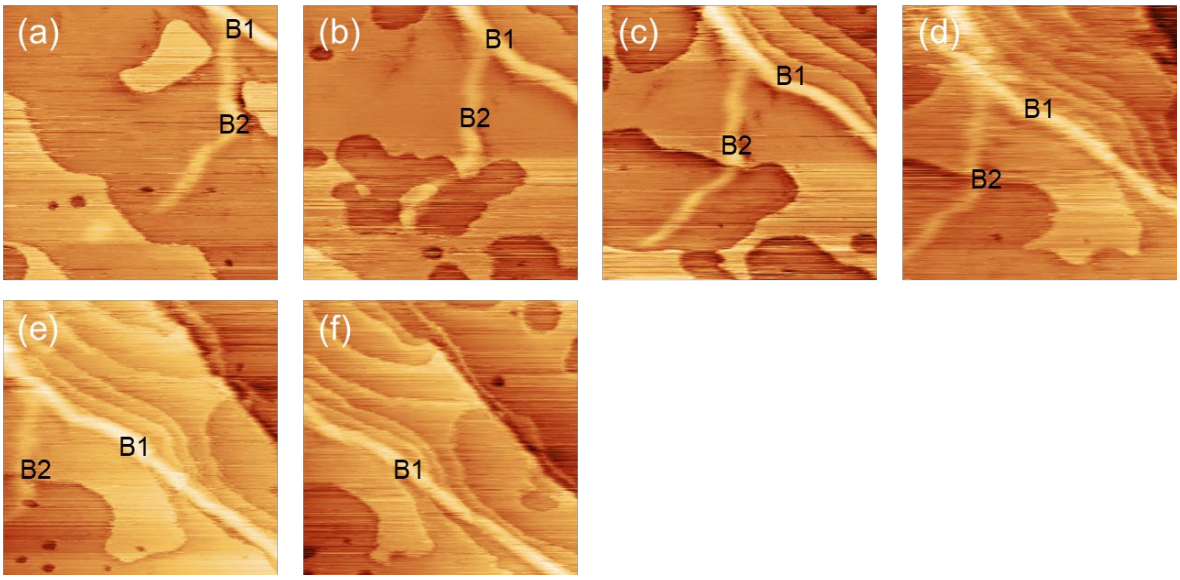

Figure S1-2: (a) to (f): Select images with 200×200 nm^2 (V_{bias} = 1 V, I = 50 pA) for increasing etch time. The image drift can be recognized by following the distinct image features B1 and B2. The complete set of 17 images in this sequence is captured in a GIF file added in Figure S1-3..

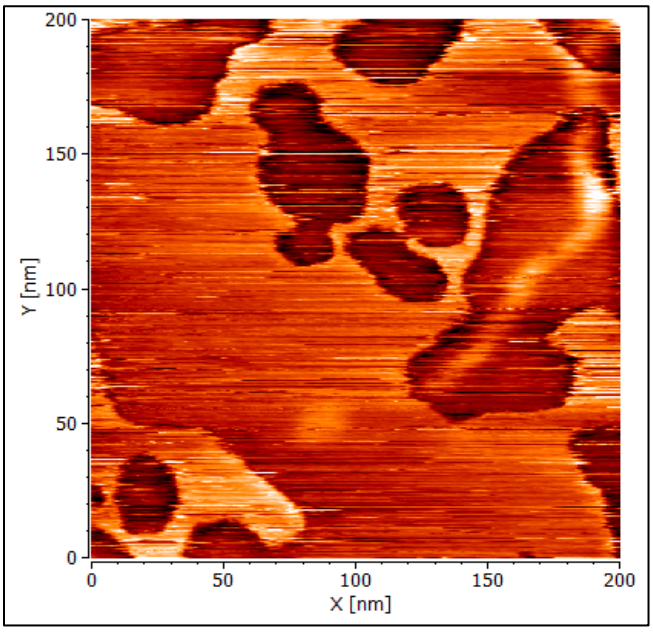

Figure S1-3: The First image of a GIF movie made of 17 sequential images spanning ~144 minutes with about 500 s per image. (V_{bias} = 1 V, I = 50 pA) Movie available from the author upon request.

S2 Test participation of scanning probe tip in the etching

To test that the STM probe, respectively the STM tip, actively participates in the etching mechanism. we carried out several scanner position changes after a few scans and observed the boundary created by the scanner. The VIs above the boundary have grown much larger in size compared to the ones below the boundary which are only captured after changing the scan region. This proves that the participation of the STM tips is essential for the surface etching discussed in this work. In addition, we held the STM tip stationary with feedback loop on in the middle of a scan and resumed after ~30 minutes, and no notable etching rate changes were discovered between the two image sections before and after the interruption. In conclusion, the scanning of the probe is essential to the etching mechanism.

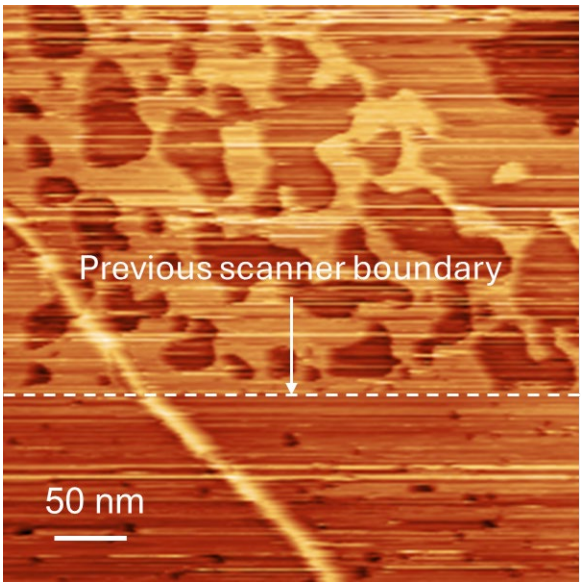

Figure S2. STM image showing the dependency of surface etching on scanner size. The previous area was scanned across for ~ 2 hours. This area was scanned across for ~ 25 minutes. The bright line extending across the image on the left-hand side is a sub-surface defects discussed also in the main body of the manuscript.

S3 Pinning of VIs at sub-surface features

In Fig. S3, we show a "pinning" effect where the growth of VIs is influenced by the sub-surface defects similar to the ones shown in Fig. 4-2(e) in the chapter 4.3 and Fig. S2. The sub-surface line defect in image S3 nearly bisects the image from top to bottom and is marked with a yellow arrow. With the presence of sub-surface defects, the removal of surface TaS_2 or the growth of VIs tends to follow the preexisting pattern of the sub-surface features. The reducing surface materials exhibit a pattern of step edge diffusion,[124] however, the removal of material in the middle of the image where the VI intersects with the sub-surface defect was delayed. Image S3 is a time series recorded over ~24 h, and in the first 4 image slices the top TaS_2 layer is completely removed, in the following three image slices the subsequent layer is etched. After several layers of

exfoliation by the tip etching, the sub-surface features are still visible, indicating a vertical propagation of defects during the growth process extending through several layers of the TMD. This means that once a line-type defect has formed the growth will be modified in its vicinity as the crystal growth continues. The removal of multiple layers by tip etching therefore gives us a clear image of what is happening during the CVT growth process itself and the etching serves like a local depth probe. Locations directly above the line defect remains the most active sites due to the structural and electronic inhomogeneities that disrupted the growth of the TMD and nucleation of the subsequent layer. This leads to the concentration of the defect density over some areas of the sample. This is why defect-free areas and smooth step edges were also observed in other areas of the sample, where there was an absence of sub-surface features.

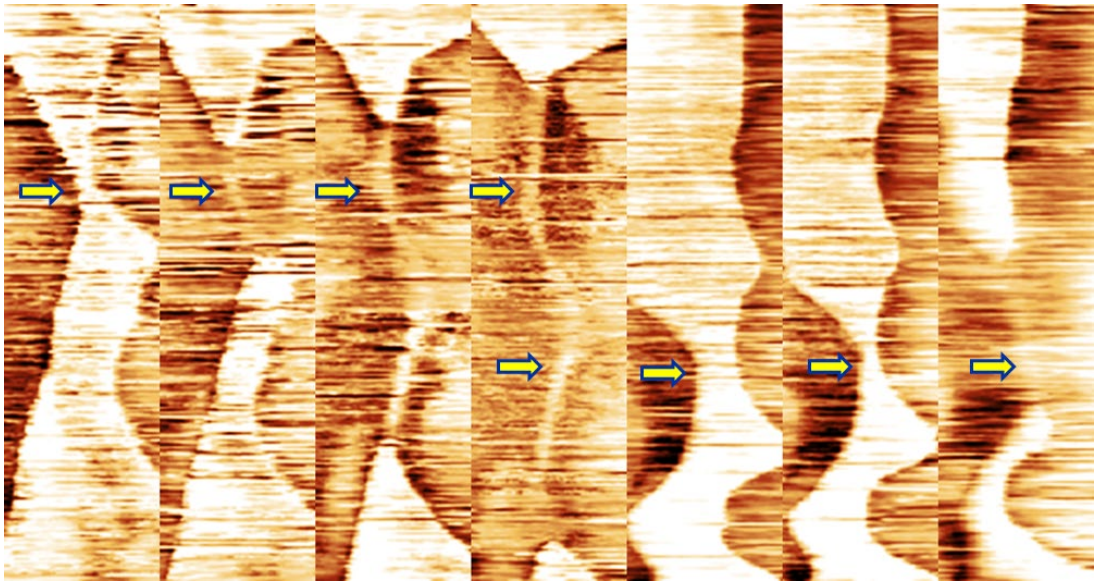

Figure S3. Sequential STM images over the same area recorded for ~ 24 hours. Different time interval between each frame. The yellow arrow indicates where the removal of the top layer is slowed/pinned by the underlying sub-surface defects.

Image stacks "movies" of the surface etching

To better display the progress of tip-induced VI growth, we combined the images presented in this work into animated GIFs, shown in Fig. S4 and S5. Images from these series were used to follow select VIs during their "lifetime" and are discussed in the manuscript. It is also evident that image quality varies dramatically over the course of etching and image acquisition, which we attribute to changes in the tip quality, and the propensity of the tip to pick up small TaS_2 fragments as shown in Figure 4-5. During the imaging for the first GIF (Fig. S4), the imaging conditions were changed a few times in order to test the impact of the voltage and tunneling current on the etching rate. Those conditions were collected in Table S1 and S2. Fig. S6 shows that a switch of bias voltage from 0.5V to 1.5V, the etching rate has a 10% decrease from 0.02783 to 0.02518. However, this kind of rate decrease is also seen for other VIs if we apply two-slope fitting for all the islands. It is worth noting that the overall etching rate seems to be decreasing over time, so there is no obvious evidence that changes in voltage and tunneling current will influence the etching rate.

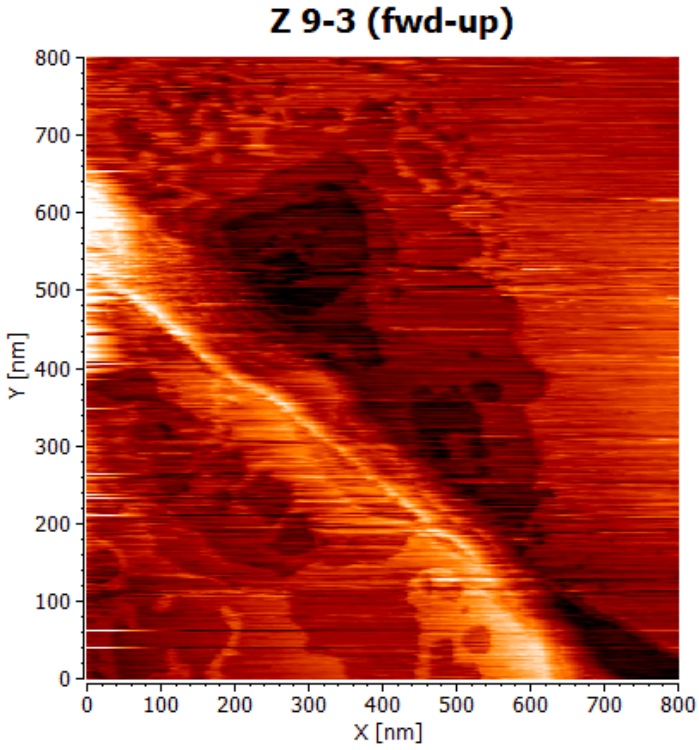

Figure S4. The first image of a GIF movie made of 68 sequential images spanning ~19.5 hours. Only one scanning direction (up and forward) was included to avoid feature twitching.

Table S1. VIs isolated and discussed in the main body of the manuscript from *set 9 movie* and their imaging conditions. "Number" refers to the respective label used in the graphs in Figures S4 and S5 , and "image number" is the subsequence isolated for the analysis of the individual VIs in this set.

Vacancy Island Number	Image Number	Bias (V)	Set Point (pA)	Probe Speed (nm/s)
1	9-20 to 9-26	0.5	20	1600
2	9-15 to 9-21	-1 and 0.5 (switch at 9-16)	20	1600
3	9-21 to 9-25	0.5	20	1600
4	9-49 to 9-71	0.5 and 1.5 (switch at 9-59)	20	1600
5	9-4 to 9-25	-1 and 0.5 (switch at 9-16)	20	1600
Coalescence	9-13 to 9-19	-1 and 0.5 (switch at 9-16)	20	1600

Table S2. VIs analyzed in set 11 movie and their imaging conditions.

Vacancy Island Number (continued count from Table S1)	Image Number	Bias (V)	Set Point (pA)	Probe Speed (nm/s)
6	11-3 to 11-9	1	50	1600
7	11-10 to 11-45	1	50	1600
8	11-26 to 11-45	1	50	1600

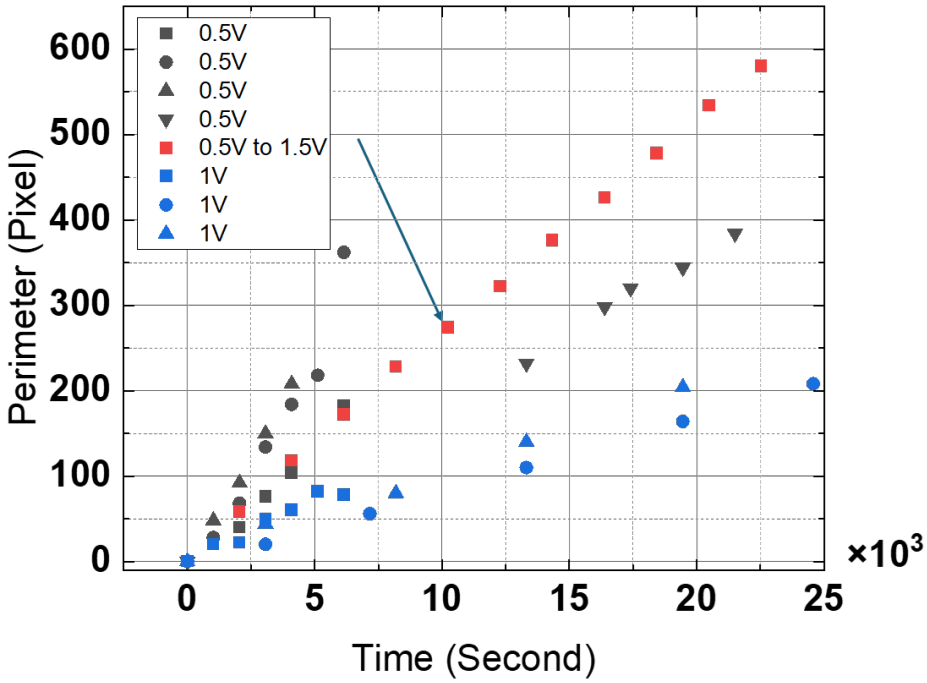

Figure S6. Perimeter progression versus growth time for VIs.

S4 VI outline process

The image masking of the VIs outlines was carried out initially by hand, but it was realized that the margin of error on the perimeter scale over the size of the figure due to a longer drawing time. As a result, a secondary method was used to extract VIs features. Selected plane-leveled images were plugged into a new AI imaging tool "Segment Anything" demo[115,125] to mask features through a Computer Vision method. The masked images were measured in FIJI[114] for area and perimeter. We found that the difference between the area calculated from the hand draw outline and Segment Anything is <3%. The challenges remain that very streaky images cannot be masked well despite the fact that they are still visible to human inspection. However, the hand drawn outlines become error prone, and we therefore limited our analysis to those VIs with the smallest errors.

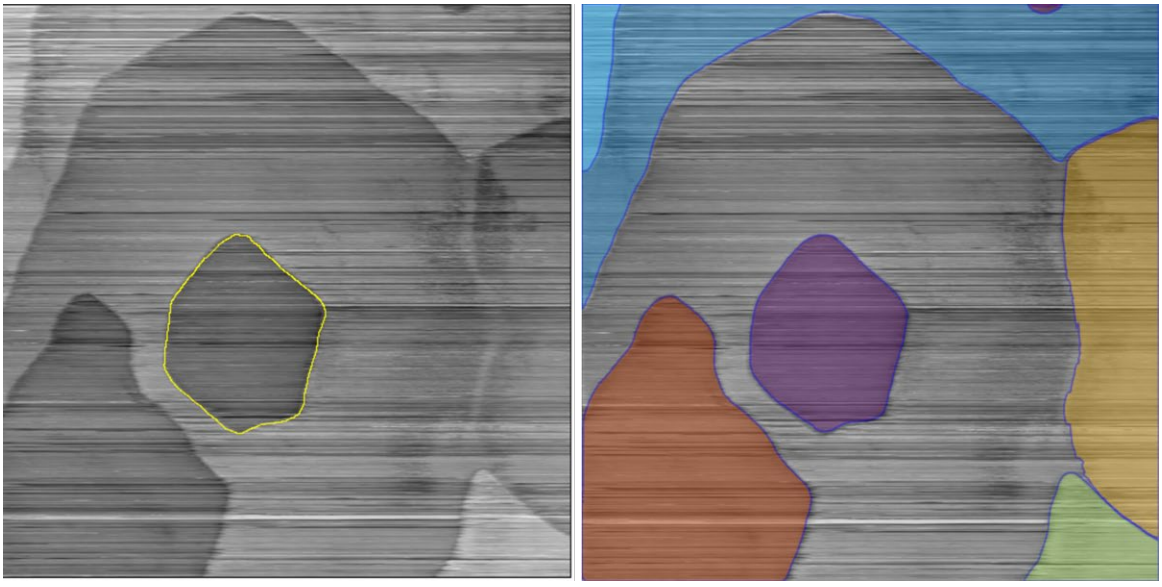

Figure S7. A comparison between the two methods used for masking VIs: (Left) Outlining by hand in FIJI [114] (Right) Auto-masking through Segment Anything demo.[115]

S5 Screw Dislocation

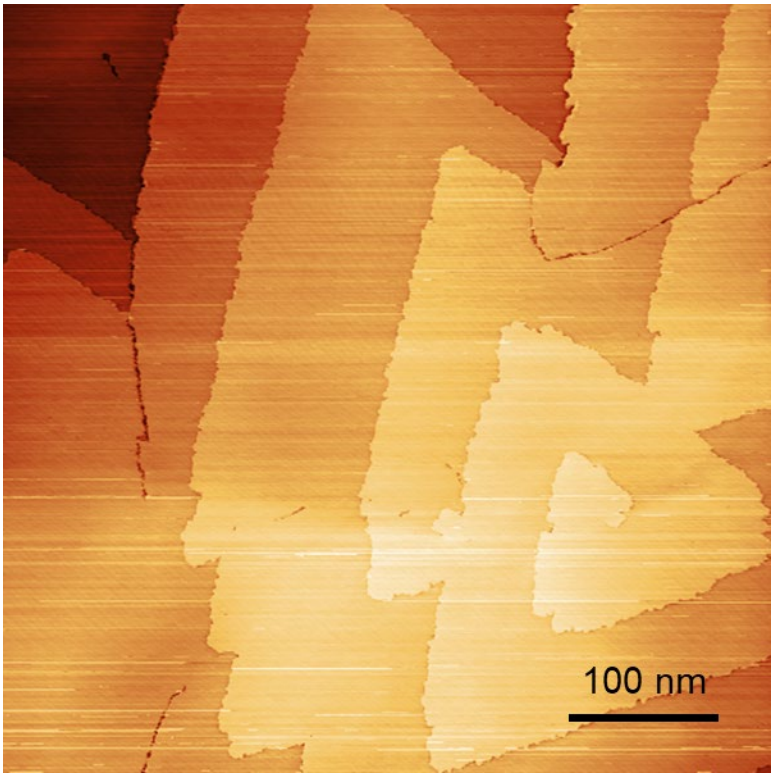

Figure S8. STM image of a separated region enriched with topological defects, including a screw dislocation, found on the 2H-TaS_2.

Fig. S8 shows a screw dislocation that has a Euclidean surface and aligned spiral angle.[126] Screw dislocations can be typical to the sample grown by the chemical vapor methods. The curvature of the vertexes is round instead of pointy, which is expected in the stacking of 2H phase layered prototypes.

4.6 Future Direction – Tip-Induced Phase Transition

During STM experiments, it is common for users to use the voltage pulse as a tip reset process when the tip is in an unstable state. It was discovered that voltage pulses could modify 2D material surface structures, like making monolayer pits on graphite.[106] Zhang *et al.* show that a 1T polytype of $TaSe_2$ can be created by pulsing the surface with a voltage, and that the size of the 1T island scales with the amplitude of the pulse.[35] A similar phase transition from the more stable 2H prototype to 1T prototype was shown on a monolayer level for a single layer of 1H on 1T bulk.[127] A domain boundary enriched metallic mosaic state was found in the 1T phase created by these procedures which is significantly different from the bulk 1T state.[128,129] It is worth noting the previously mentioned publications were done at a temperature of 10 K or below. This process is particularly interesting because it introduces a brand new way of studying TMD phase transitions and these materials exhibit ample electronic states, like superconductive[130] and CDW[127], as well as a Mott insulating state.[131-133] Additionally, having the ability to precisely create 1T and 2H polymorphs has profound implications in the field of electronic device manufacturing[134-136] and hydrogen evolution reaction catalysts.[21,137-139] Phase transitions in TMD bulk materials has been studied through theory[135,140] and experiments.[141,142] However, scanning probe microscopy remains the only method to study the single layer phase transition because it can introduce a focused tunneling current to specific surface sites and also examine the local outcome with surface sensitivity. On top of our previous report on pulse voltage tip-induced etching, it was found that our tip reset process could introduce some level of superlattice on the surface but due to the high noise level in imaging at room temperature, no atomic resolution image was produced. The tip-induced phase transition was recreated during the liquid nitrogen

temperature STM measurements on 2H-TaS_2. We started with negative voltage pulses at various bias and tunneling current set points.

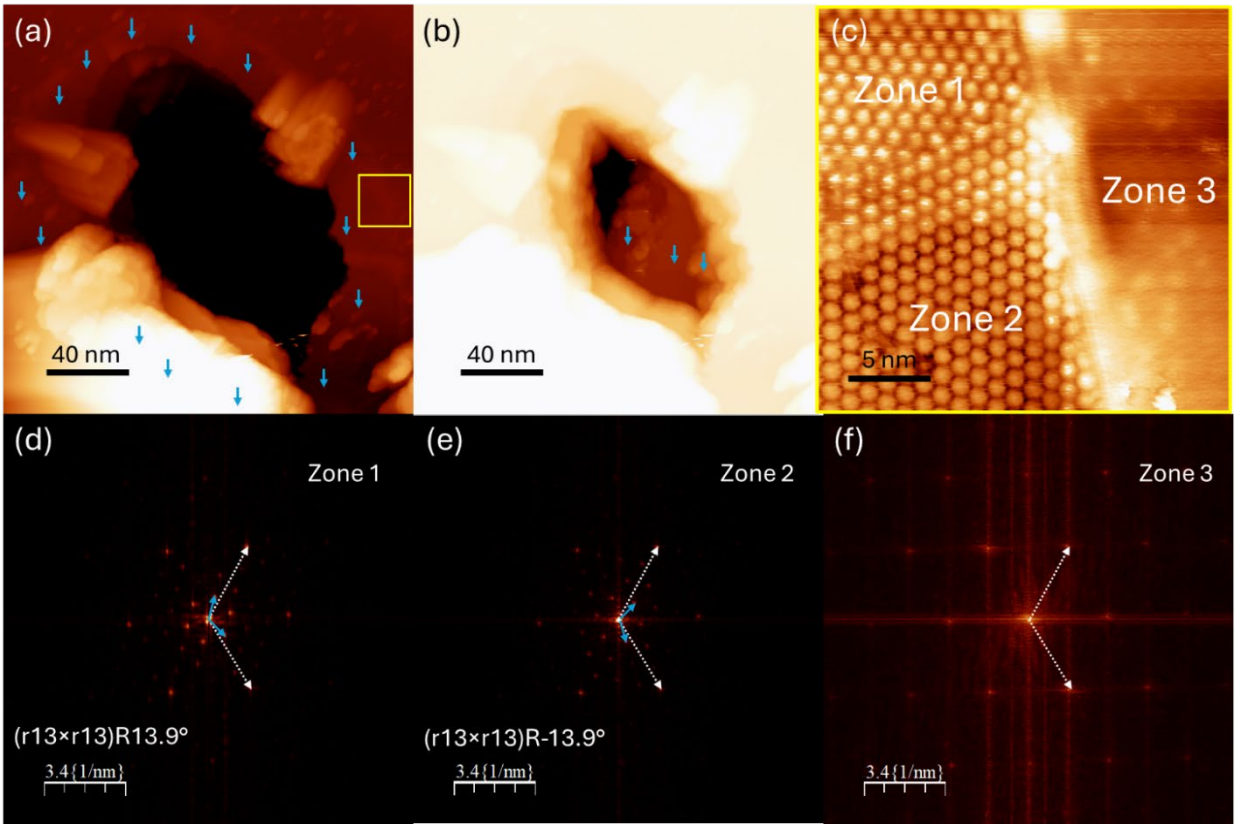

Figure 4-6. Voltage Pulse induced surface damage and 1T phase transition on 2H-TaS2. (a) STM image of the out (b) Same image in (a) but with adjusted contrast to show the center crater area. (c). (d) – (e) 2-D FFT of STM image in Zone 1, 2, and 3, respectively.

In Fig. 4-6, the aftermath of a single tip pulse at -2.3 V for 4 ms from a setpoint of -1.1 V, 36 pA is shown. It was found that a huge crater was created at the origin of the voltage pulse. A halo of superstructures was created by the pulse, labeled by blue arrows in Fig. 4-6(a) and (b). A high-resolution STM image over the domain boundary between 1T and 2H phases is shown in Fig. (c). The in-plane superlattice in Zone 1 and 2 exhibit a $(\sqrt{13} \times \sqrt{13})$ periodic unit cell, which

corresponds to the commensurate CDW states at a temperature below 200 K.[143] The sulfur atomic unit cell of the 1T domain is identical to the intrinsic 2H domain, ruling out the possibility of Moire pattern created by top surface layer mismatch. Interestingly, we found that the "Stars of David" superstructures have different directionality. From the 2D-FFT in Fig. 4-6(d) and (e), it was discovered that Zone 1 has a $(\sqrt{13} \times \sqrt{13})\ R13.9°$ supercell, but Zone 2 has a $\left(\sqrt{13} \times \sqrt{13}\right)R - 13.9°$. The current imaging tunneling spectroscopy data of each zone has been taken, and it was learned that there are several smaller domains that exist in each zone. As a result, line spectra from one domain to another do not give us a clean-cut summary of the electronic structure for each domain and boundaries. Future work will use machine learning methods, like k-mean clustering[144], to separate smaller domains by their corresponding STS spectra.

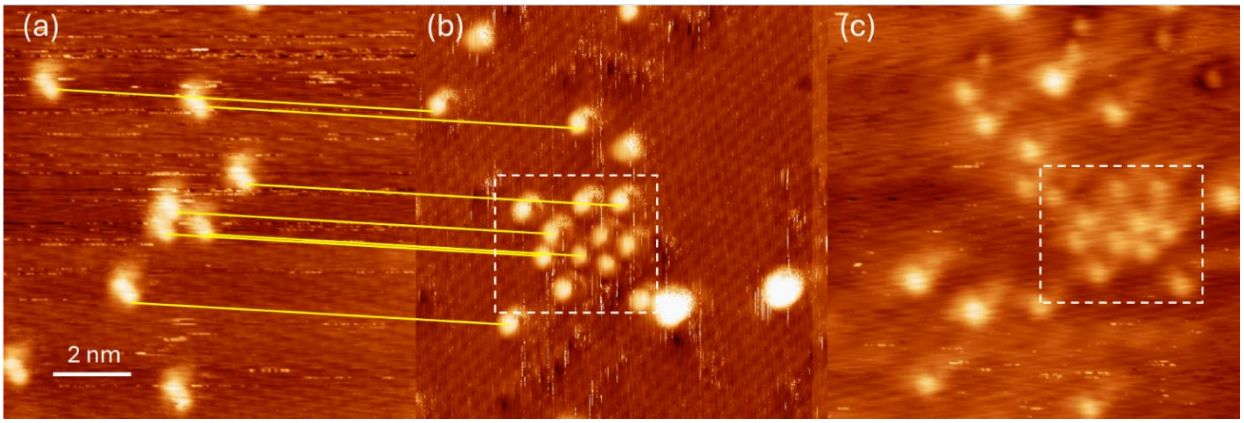

Figure 4-7. 2H to 1T phase transition induced by small area high voltage scanning. The yellow line across (a) and (b) indicates the same bright spots. (a) Setpoint: -1V, 200pA (b) Setpoint: -500mV, 200pA. (c) Setpoint: 1V, 50pA.

It has occurred to us that the voltage pulse method is not very efficient due to more frequent tip state changes at 77 K compared to 4 K. In addition, the damage caused by the pulses not only limits the application of the 1T-nanocrystal created this way, but also destabilizes the tip, making

the data collection about the aftermath difficult to interpret. Inspired by the tip-induced defect growth and a previous phase transition study on a CO monolayer on Cu(111),[145] a high voltage scanning process was adapted to study the fundamental phase transition steps from 2H to 1T. In Fig. 4-7, before(a), 510 seconds of -2.7 V, 200 pA scan was carried out in a 1×1 nm (256 x 256 pixels) region in the middle of the frame with a 1 nm/s scanning speed;; from (a) to (b), 820 seconds of -2.7 V, 200 pA scan was carried out in a 1×1 nm (256 x 256 pixels) region in the middle of the frame with a 1 nm/s scanning speed; from (b) to (c), 893.2 seconds of -2.7 V 200 pA in a 1 x 1 nm (512 x 512 pixels) region at the bottom left of the white dashed box in (b) 1 nm/s. It was shown that individual bright spots are created on the surface. At the center of the STM images, where the high voltage scans were carried out, a single $(\sqrt{13} \times \sqrt{13})$ unit cell was assembled in Fig. 4-7(b). However, the following scan did not extend the supercell but created more bright spots in the surrounding area.

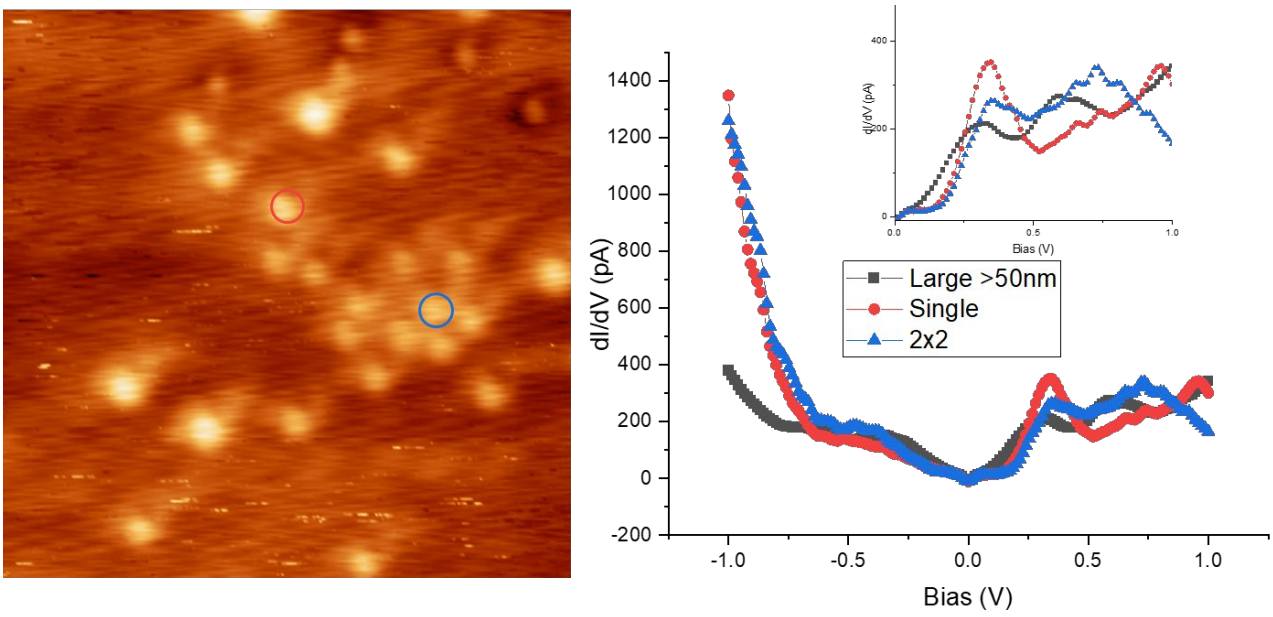

Figure 4-8. (Left) STM image after several sessions of high voltage scanning. The locations for STS are labeled by red and blue circles. (Right) dI/dV of single bright spot (red circle), the single 2×2 unit supercell (blue circle), and the 1T domain (black curve, taken in Zone 2 in Figure 4-6(c)). Spectroscopy setpoint: 1V, 200 pA.

To make sure the bright spots created are indeed associated with the 1T phase, the dI/dV spectra of the bright spots are plotted together with dI/dV taken from Zone 2 in Fig. 4-6(c). From the fermi level to 1 V, we can see the single point and single unit cell both have a state at 0.35 V and the Zone 2 has a state at 0.30 V. The second notable state is at the range between 0.58 V to 0.96 V. It is shown that there is a decreasing trend in peak energy and amplitude as the supercell size increases from a single point to a unit cell to a large area of 1T domain. Future work in progress is to find the transition threshold energy by varying the pulse voltage and its starting current or

position setpoint. A different scanning path instead of the classic line-by-line path will be explored to see if it is possible to continuously build extra supercells on the foundation of existing ones.

Chapter 5. Comparative Study of Surface Electronic Structures of Fe_xTaS_2 and 2H-TaS_2

5.1 Introduction

Transition metal dichalcogenides (TMDs) are a family of two-dimensional (2D) materials that have sparked extensive interest for their tunable electronic,[93] magnetic,[91,146] and optical properties.[147] TMD sandwiched layers typically bond by a weak van der Waals interaction, which leads to opportunities for introducing stable dopant within the van der Waal gaps. The intercalation of 3d and 4d elements in transition metal dichalcogenides can be used to achieve control of magnetic properties.

Fe_xTaS_2 is formed by layers of TaS_2 which are intercalated with the 3d magnetic metal Fe. The guest Fe atoms occupy octahedral sites within the van der Waals gaps of the 2H-TaS_2. These materials show non-trivial magnetic behavior. The increase in Fe intercalant composition induces a ferromagnetic (FM) to antiferromagnetic (AFM) transition at $x \cong 0.4$. The Curie temperature of Fe_xTaS_2 also exhibits a strong dependence on Fe concentration. As Fe concentration increases, the Curie temperature rises, reaching a maximum value of 160 K at x = 0.25 and starting to decrease to 35K at x = 0.33.[148-150] In $Fe_{0.25}TaS_2$, the Fe intercalant forms a supercell with horizontal lattice constant $a' = 2a_0$, where a_0 is the lattice constant of the 2H-TaS_2. Fe atoms on each layer overlapped with the atoms in an adjacent layer. In $Fe_{0.33}TaS_2$, Fe intercalant forms a noncentrosymmetric $(\sqrt{3} \times \sqrt{3})R30°$ supercell, where the intercalating Fe atoms don't align in adjacent slabs.[151] These supercells have been observed experimentally through electron

diffractions.[152-154] Magnetotransport measurements were carried out over Fe_xTaS_2 materials with different x composition from 0.25 to 0.33. A large magnetoresistance (MR) was found in $Fe_{0.28}TaS_2$ and the Selected Area Diffraction pattern suggest a $\left(\sqrt{3} \times \sqrt{3}\right)R30°$ supercell, which normally exist in a 0.33 intercalant composition[152]. The rise in MR in off- stoichiometric Fe_xTaS_2 suggests a connection to magnetic disorder scattering, which fundamentally results from a misalignment of the magnetic moments.[155] The misalignments may arise from crystallographic defects stemming from deviations in the commensurate Fe concentrations (x = 0.25, 0.33). Direct observation of such crystallographic defects and their impact on the local electronic and magnetic structure is desirable to advance our understanding of how to engineering controllable MR domains on TMDs.

Like most of the TMDs, TaS_2 occurs in several polytypes, in which the coordination of the transition metal can be either trigonal prismatic (D_{3h}) or octahedral (O_h), and they are named 1T or 1H, respectively. For multi-layers of the 1H, the polytype is named 2H, because its unit cell extends past one vdW layer.[156] 2H polytype is exhibiting superconductivity with a critical temperature of 0.5 K while in bulk crystal form, and it was shown to have a higher critical temperature of 2.2 K when the layers are atomically thin.[130] $4H_b$-TaS_2 is a van der Waals heterostructure comprised of alternating 1T- and 1H-TaS_2 layers, which further increases the superconducting critical temperature to 2.7 K.[157] Charge density waves (CDWs) often develop in the transition metal dichalcogenides, which includes both symmetry types of layered TaS_2. 1 T-TaS_2 shows $\sqrt{13} \times \sqrt{13}\, R13.9°$ CDWs below 540 K, which changes from incommensurate to nearly commensurate upon cooling from 540 K to 350 K. And the CDWs transform to fully commensurate at 180 K, which is associated to the Mott insulating state of the 1T polytype.[131]

Bulk 2H-TaS_2 was reported to form a 3×3 commensurate CDW at 75 K and higher.[158,159] For $4H_b$-TaS_2, both $(\sqrt{13} \times \sqrt{13})\ R13.9°$ and $(3\times3)R30°$ exist within each layer, therefore the Moiré pattern of the superposition of these two supercells can be observed with STM.[160] Such Moiré superpositions of the conventional CDWs in magnetic 2-D materials have been utilized to engineer quantum material properties and to study the unconventional Ising superconductivity.[161-164] Even though Fe intercalated TaS_2 magnetic transport properties have been extensively studied. It remains unknown how the CDW supercells interact with intercalant supercells. As a result, it is crucial to study the TMD intercalation using real space techniques.

To further assess the profound impact on the surface electronic and spin structure of the TMD system, scanning tunneling microscopy/spectroscopy was employed to study the Fe-intercalated and 2H-TaS_2 at 77 K. We observe (1) the 2H-TaS_2 sample does not exhibit significant superlattice in STM/S, (2) Fe-intercalated sample has a strong $\left(\sqrt{3} \times \sqrt{3}\right)R30°$ superlattice in itssurface electronic structure, (3) and the surface LDOS of Fe-intercalated sample shows a peak at around -500 meV that shows increased DOS as the local concentration of Fe intercalants increases.

5.2 Experimental Methods

Fe_xTaS_2 single crystals were prepared using iodine vapor transport in a sealed quartz tube. A nominal composition of $Fe_{0.33}TaS_2$ was sealed into the quartz tube, and upon removal, the single crystals were annealed for ~2 days. Fe intercalations happen naturally in the CVT growth process, forming $Fe_{0.25}$- and $Fe_{0.33}$-TaS_2 domains. The Fe concentration was determined from EDS measurement at NIST. The EDS determined composition was $Fe_{0.28}TaS_2$. 2H- TaS_2 single crystals

were synthesized by chemical vapor transport (CVT) with iodine as the transport agent. Detailed preparation and crystallography characterization were described in Chapter 4 of this dissertation. Both Fe_xTaS_2 and 2H- TaS_2 single crystals were cleaved *in-situ* on a cold stage which was cooled by liquid nitrogen under ultrahigh vacuum (UHV) conditions ($< 1\times10^{-10}$ torr). The cleavage setup includes a heating step to ~ 400 K to cure the epoxy. After cleavage, the samples were immediately transferred under UHV into a pre-cooled homemade high magnetic field low temperature scanning tunneling microscope. STM/STS experiments were carried out at 77 K with base pressure lower than 1×10^{-10} Torr using electrochemically etched nickel tips for intercalated samples and tungsten tips for unintercalated samples. Topographic images were acquired in a constant current mode with a bias voltage applied to the samples. All the spectroscopies were obtained using a lock-in amplifier with bias modulation V_{rms} = 20 mV at 977 Hz.

5.3 Results and Discussion

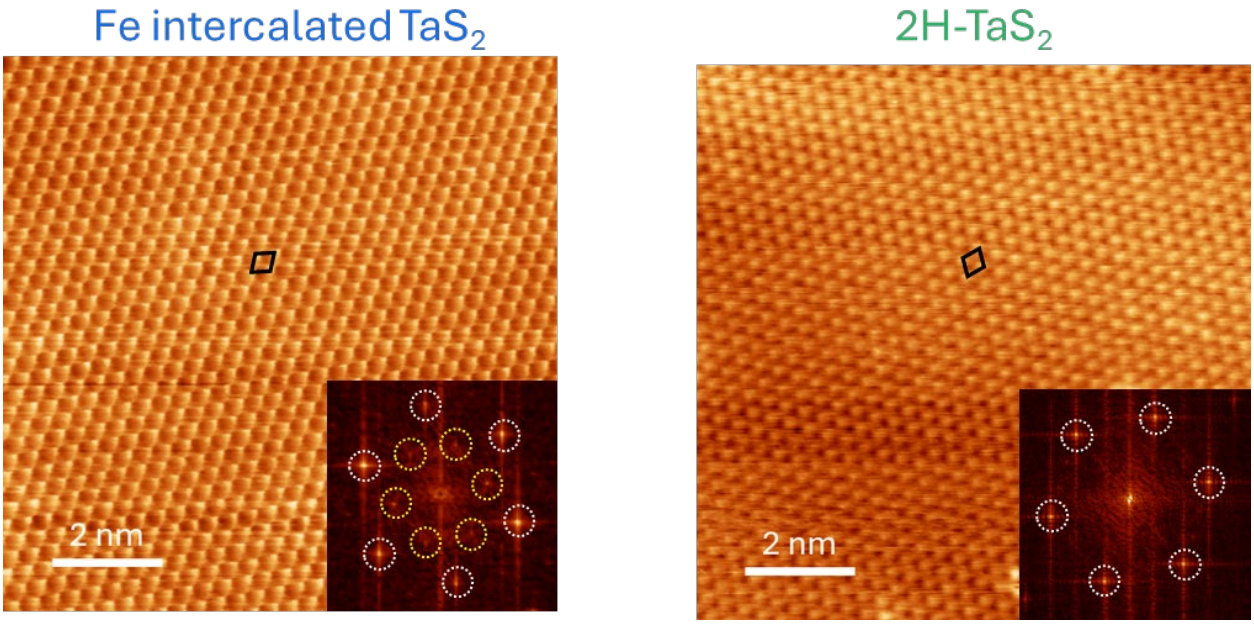

Figure 5-1. Atomic resolution STM images of (Left)Fe-intercalated $Fe_{0.28}TaS_2$, (V = 2 V, I_t = 5 pA), and (Right) 2H-TaS_2 (V = 15 mV , I_t = 50 pA).

High crystalline quality 2H-TaS_2 sheets and Fe intercalated TaS_2 sheets were synthesized via the CVT method and verified by XRD (x-ray diffraction) measurements. The crystals were cleaved *in situ* on a cold stage at 77 K, and then studied by scanning tunneling microscopy/spectroscopy. Some S vacancies and oxygen substitution defects, which are common on TMDs samples, were found on the surface. The STM and current imaging tunneling spectroscopy (CITS) data are taken far from the presence of such defects. Fig. 5-1 shows a side-by-side comparison of atomic resolution images of the two samples, and the Fe-intercalated sample has a $\sqrt{3} \times \sqrt{3}\, R30°$ superlattice. Over the pristine area of the 2H-TaS_2, we conducted multi-biases STM and CITS, and the LDOS were calculated using the method described in Chapter 2. For the

Fe intercalated sample, the existence of a subsurface defect was noticed, and the CITS was collected over a subsurface defect (black dashed circle), which is shown in Fig. 5-2.

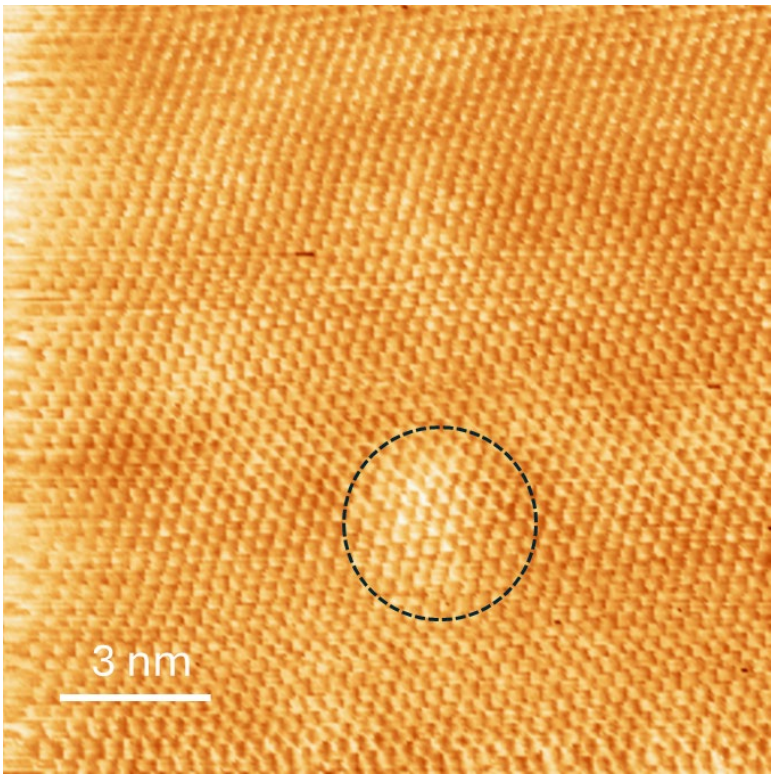

Figure 5-2. Topography of $Fe_{0,28}TaS_2$ taken simultaneously with the current imaging tunneling spectroscopy. (Setpoint: V = 2 V, I = 200 pA)

It is important to note that we did not observe a stable 3×3 CDW on either sample. Even though previous studies have shown CDW states are fully commensurate at 77 K,[158] it is common that the direct observation of standing wave pattern needs to happen at a much lower temperature.[127] 1T phase was also introduced through electric field-induced phase transition in a separate study, and the $\sqrt{13} \times \sqrt{13}\, R13.9°$ CDWs were very distinguishable from the supercell observed on Fe intercalated samples. Therefore, it is confirmed that the $\sqrt{3} \times \sqrt{3}\, R30°$ is a result of the Fe intercalation instead of being a reconstructed TaS_2 polytype.

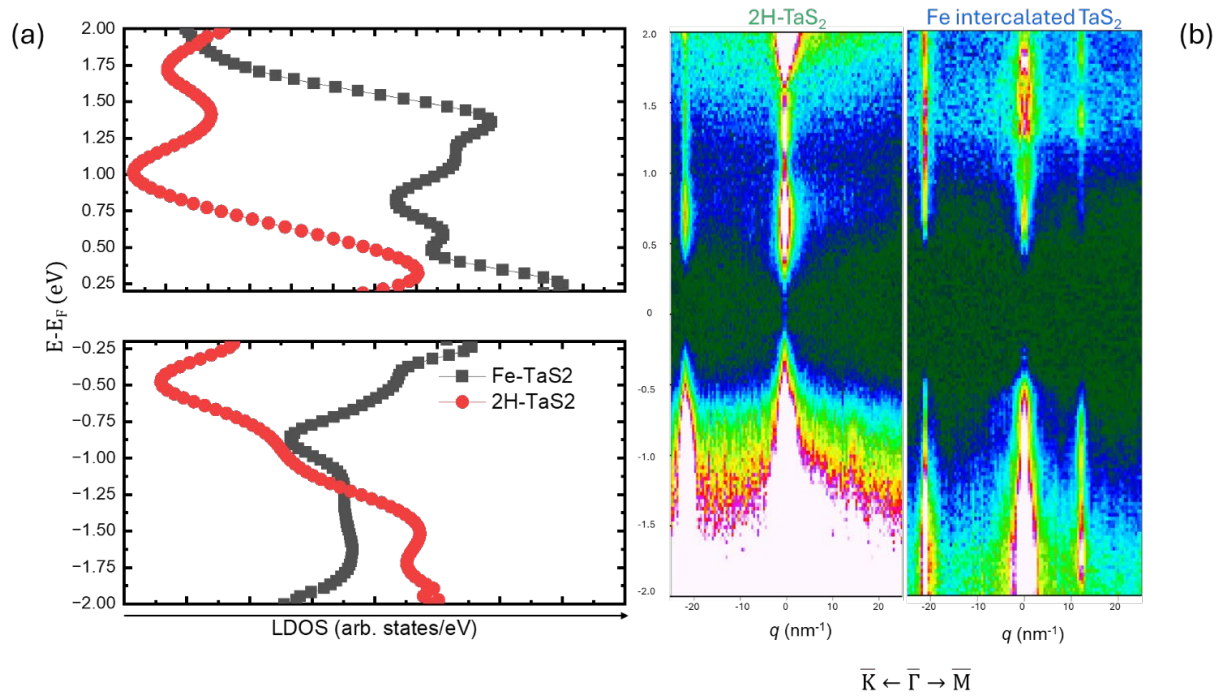

Figure 5-3. Comparison of the electronic structure of 2H-TaS_2 and Fe_xTaS_2. (a) Normalized LDOS calculated from averaged I-V spectra. The Fermi states are removed due to the lack of detection of states. (b) Energy vs. QPI signal in $\overline{K}-\overline{\Gamma}-\overline{M}$ directions. The energy axes are aligned for (a) and (b)

Fig. 5-3(a) displays the surface local density of states calculated from the averaged I-V spectra collected through CITS. dI/dV was also collected, using the lock-in technique introduced in Chapter 2, but I-V curves gave a lower LDOS noise level. Due to the current and bias voltage setpoint selection, the energy range 200 meV to -200 meV doesn't resolve the LDOS sufficiently, so the curve within range after normalization is not displayed here. There are significant differences between the surface LDOS between the two samples. For the occupied states (negative biases), a new state is located around -500 meV, and importantly a uniform density of states for around 600 meV is developed between -1.15 eV and -1.75 eV. For the empty states (positive biases), more states can be resolved compared to the unintercalated sample. Fig. 5-3(b) shows the

Quasiparticle inference analysis map. For additional QPI signal at $q \approx 12$ nm $^{-1}$ along the $\bar{\Gamma}$-$\bar{M}$ direction is found for the Fe intercalated sample which corresponds to the $\sqrt{3} \times \sqrt{3}\, R30°$ state inside the Brillouin zone. Additionally, the intercalation-induced states break between 1.5 to 1.68 eV and -1.9 to -2 eV.

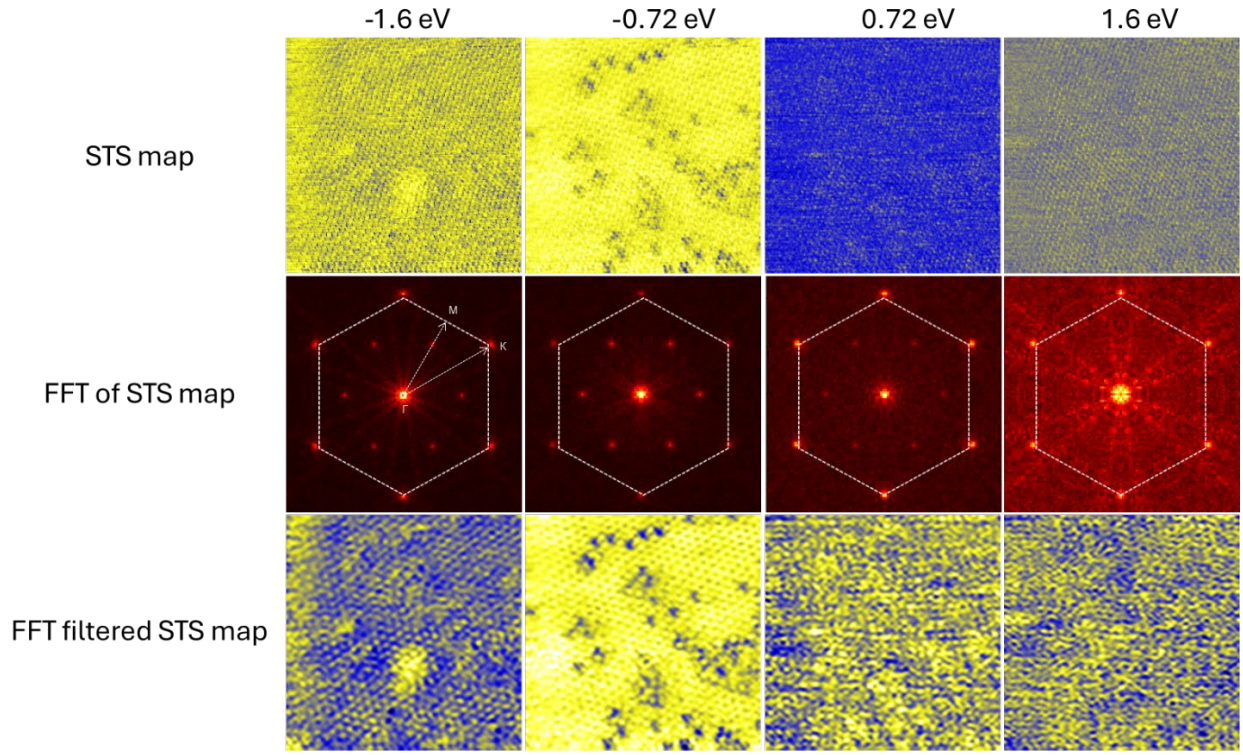

Figure 5-4. (First Row) From left to right, the slices in the hyperspectral CITS maps of $Fe_{0.28}TaS_2$ at -1.6 eV,-0.72 eV, 0.72 eV and 1.6 eV. (Second Row) Drift corrected FFT of the STS map in the same column. The dashed hexagon indicates the surface Brillouin zone. (Third Row) FFT-filtered STS maps, where the FFT signals higher than $q \approx 15$ nm $^{-1}$ are filtered from the image.

After evaluating the individual STS maps of the $Fe_{0,28}TaS_2$ for further analysis, ±0.72 eV and ±1.6 eV slices were shown here in Fig. 5-4. The $\sqrt{3} \times \sqrt{3}\, R30°$ supercell exists in each slice except +1.6 eV, which agrees with the observation in the QPI map. The supercell FFT signals dissipate, and the atomic unit cell signal also weakens. The lattice points having a lowered intensity

lowered the image dI/dV maximum, so it appears that some new states arise around the $\bar{\Gamma}$ point. In the occupied states, we noticed a contrast change on top of the subsurface defect at -1.6 eV and also scattered apparent vacancies at -0.72 eV. For better clarity focused on the defect features, 2D-FFT filtering was applied to the STS maps to remove the signal with a low pass filter with a cutoff at $q \approx 15$ nm $^{-1}$. The filtered maps are shown in the third row of Fig. 5-4. The scattered defects have very little difference in the STS spectra and LDOS. However, the subsurface defect has a very different supercell structure from the surrounding.

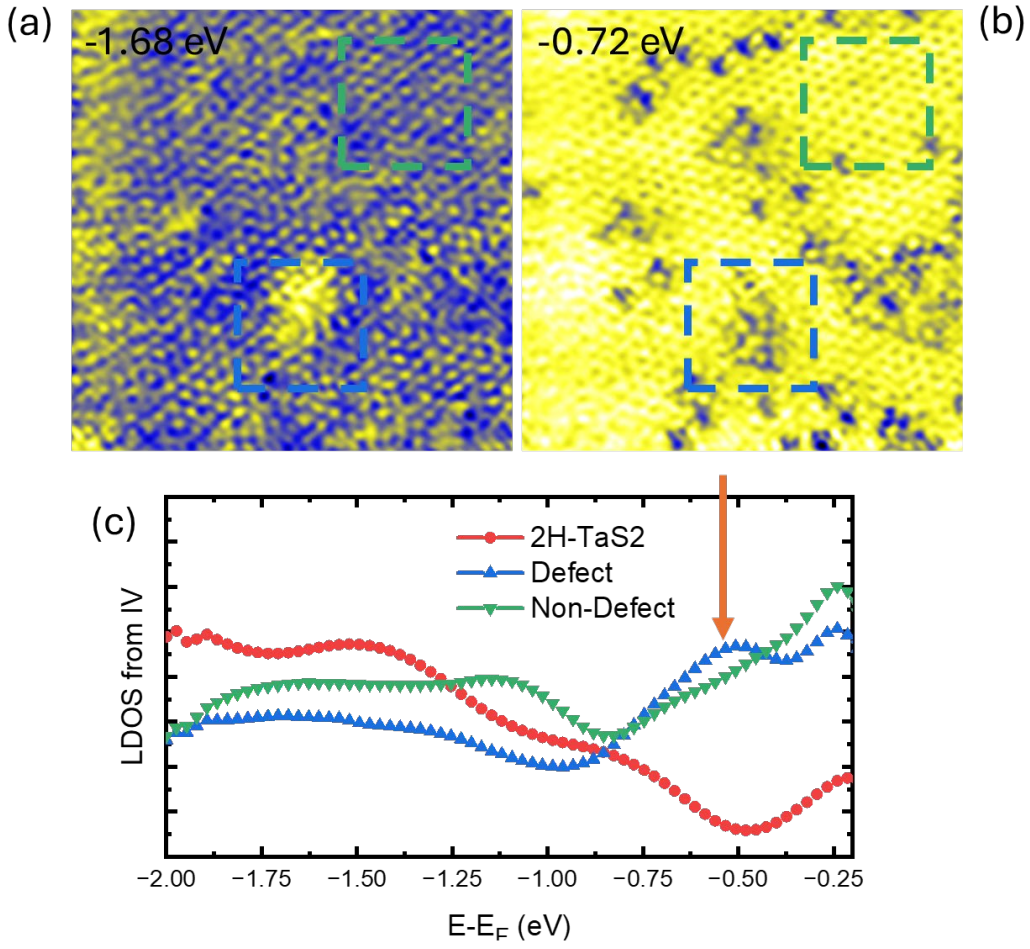

Figure 5-5. Appearance of Fe clustered pocket in $Fe_{0,28}TaS_2$. (a) dI/dV slice at -1.68 V. (b) dI/dV slice at -0.72 V. (c) Normalized LDOS calculated from averaged *I-V* spectra taken in the green and blue boxes in (a) and (b), and they are being compared with 2H-TaS_2 LDOS, which has no Fe composition.

To better understand the nature of the subsurface defect and its impact on the surface electronic structure of $Fe_{0.28}TaS_2$, we averaged the STS spectra from a region over the defect and a region over the intact superlattice, which is represented as the blue and green dashed box, respectively, in Fig. 5-5(a) and (b). We found no significant difference between the defect and non-defect STS in the empty states, but at negative biases, the new occupied state that was at

around -600 meV in Fig. 5-3(a) varies both in energy and amplitude. The position of the defect peak is closer to the Fermi level, sitting at around -500 meV, and LDOS increases slightly at the apex compared to the non-defect LDOS. Moreover, the uniform LDOS for the defect is being pushed in the negative direction, away from the Fermi level. From Fig 5-5(a) and (b), after the signal from TaS_2 atomic unit cells being filtered out, the horizontal location of the Fe within the lattice can be seen, which is showing as the bright yellow spots in the dI/dV slices. Around the defect, the Fe units are distorted and concentrated around the center of the defect. We believe that this is an indication of clustering or segregation of the intercalated Fe, which is also supported by the fact that the current supercell observed is off-stoichiometric to the energy dispersive spectroscopy evaluation. The Fe vacancies in the $\sqrt{3} \times \sqrt{3}\, R30°$ supercell lead to distortion in the Fe layer, creating Fe clusters that strengthen the LDOS at -500 meV.

5.4 Future Direction

Currently, our collaborator has completed the DFT calculations for the surface of $Fe_{0.125}TaS_2$ and $Fe_{0.25}TaS_2$. These structures have been shown to generate 2 × 2 supercells and contain non-trivial Fe states at around -500 meV and stateless gaps at around ±2 eV. These results are promising to interpret our STS results, but the differences in Fe composition between the calculation and sample used in the experiments make it difficult to establish a comparison directly. At 4K, Fe and Cr intercalations introduce a ferromagnetic transition below the Curie temperature.[151] Our magnetic properties measurements also agree with the phase assignment for $Cr_{0.33}TaS_2$. As a result, it is very valuable to conduct STM and spin-polarized STM on intercalated TaS_2 samples at 4K where the superconducting magnets can operate. We expect to see different magnetic domains on surfaces of intercalated 2H TaS_2 created by the subtle differences in the local

Fe composition, clustering and segregation, especially around the -500 ± 100 meV LDOS feature, where the Fe contributes significantly to the surface electronic structure. In addition, the 2H's 3×3 CDWs should become fully observable at 4 K. The interaction between the intercalation-induced supercell and TMDs' CDWs has not been studied thoroughly before and remains critical to the process of engineering the low temperature magnetic properties of TMDs.

Chapter 6 Large Bandgap Observed on the Surfaces of $EuZn_2As_2$ Single Crystals

This manuscript has been authored by UT-Battelle, LLC under Contract No. DE-AC05-00OR22725 with the U.S. Department of Energy. The United States Government retains and the publisher, by accepting the article for publication, acknowledges that the United States Government retains a non-exclusive, paid-up, irrevocable, world-wide license to publish or reproduce the published form of this manuscript, or allow others to do so, for United States Government purposes. The Department of Energy will provide public access to these results of federally sponsored research in accordance with the DOE Public Access Plan (http://energy.gov/downloads/doe-public-access-plan)

6.1 Introduction

In the topological physics community, topological materials with magnetism are extremely attractive, as they exhibit unique physical properties arising from the interplay between their topological electronic structures and magnetic ordering. In particular, their ability to support chiral electron channels with robust and controllable spin-dependent transport properties makes them highly promising for potential applications in spintronics and quantum computing.[165,166] In the search for magnetic topological materials, EuM_2As_2 (M = Zn, Cd, In, Sn, etc.) compounds have received extensive attention in the materials science community. The excitement was initially generated by intensive experimental and theoretical investigations on $EuCd_2As_2$, which suggested

that its electronic structure is topologically protected because of its combined crystallographic and magnetic structures.[167,168] In particular, angle-resolved photoemission spectroscopy (ARPES) measurements indicate the topological phase transition from the Weyl state with a single pair of Weyl points above the Eu ordering temperature $T_N \sim 9$ K to the Dirac state below T_N.[167,169] Eu moment direction in $EuIn_2As_2$ determines the formation of either the axion-insulating state or topological-insulating state.[170,171] Eu-based compounds are thus considered an ideal platform for studying the relationship between electronic topology and magnetism, with switchable topological states solely controlled by magnetism. Naturally, the electronic structure of such a system depends strongly on the magnetic configurations for both bulk and surface.[167-170,172,173]

However, none of the EuM_2As_2 family members has been studied thoroughly. For example, both band calculations and experiments suggest $EuCd_2As_2$ is a topological semimetal.[167,169] There is accumulating evidence for the deviation of the semimetallic behavior for $EuCd_2As_2$ with a low carrier density.[174-176] The semiconducting nature with the bandgap around 0.77 eV has been observed for both bulk[174] and surface.[177] Earlier observation of the metallic transport in $EuCd_2As_2$ could result from band bending at the surface.[175] To investigate the electronic properties at the surface, scanning tunneling microscopy/spectroscopy (STM/S) is an ideal probe, which offers the direct measurement of the local density of states (LDOS) at the atomic level. STM experiments conducted on $EuIn_2As_2$ yielded a partial Eu-terminated surface after cleavage at room temperature[178] and 20 K.[179] However, such partial Eu termination was not observed in $EuCd_2As_2$.[177] Given that the crystal structure of $EuCd_2As_2$ ($P\text{-}3m1$) is slightly different from $EuIn_2As_2$ ($P6_3/mmc$), comparison of the surface termination between them may not be straightforward, however.

Among existing EuM_2As_2 compounds, $EuZn_2As_2$ forms the same structure as $EuCd_2As_2$.[180] Due to closer packing, Eu in $EuZn_2As_2$ orders antiferromagnetically at $T_N \sim 19$ K, double that for $EuCd_2As_2$.[180,181] Above T_N, magnetic fluctuation persists to ~200 K.[181] $EuZn_2As_2$ is thus an excellent system to explore the interplay between electronic properties and magnetism above and below T_N. At present, the surface-state properties of $EuZn_2As_2$ are unknown. Especially, is there evidence for nontrivial electronic topology as seen in $EuCdAs_2$ by ARPES? Given the difficulty in distinguishing Eu and CdAs terminated surfaces in $EuCd_2As_2$,[177] interpretation of data obtained from surface sensitive techniques such as ARPES becomes ambiguous. In this article, we report investigations of the surface electronic structures of $EuZn_2As_2$ single crystals with STM/S and first-principles calculations. The surfaces were created by cleaving single crystals at liquid nitrogen temperature. Through STM/S, we find several types of surface and subsurface defects that have a profound impact on the surface electronic structure, thus allowing us to distinguish different terminations. There are distinct differences between the electronic structures of Eu- and ZnAs-terminated surfaces, which are elucidated by STS measurements. Our results allow us to address questions including (1) the surface atomic and electronic structures of $EuZn_2As_2$, (2) similarities and differences between Eu- and ZnAs-terminated surfaces, and (3) the impact of defects.

6.2 Experimental Methods

Single crystals of $EuZn_2As_2$ were grown via the flux method using Sn with details described elsewhere.[1] The crystal structure was determined via x-ray diffraction at room temperature, which belongs to *P*-3*m*1 space group (#164) with the lattice constants $a = b = 4.2093$

Å, and c = 7.153 Å. The magnetization measurements indicate the antiferromagnetic transition temperature T_N = 19 K. The in-plane electrical resistivity shows metallic behavior above ~ 200 K but nonmetallic below 200 K.[1]

The $EuZn_2As_2$ single crystals were cleaved on a cold stage which was cooled by liquid nitrogen under ultrahigh vacuum condition (< 1×10^{-10} torr). The samples were immediately *in situ* transferred into a pre-cooled homemade high magnetic field low temperature scanning tunneling microscope. STM/STS experiments were carried out at 77 K with base pressure lower than 1×10^{-10} Torr using electrochemically etched Tungsten tips (W tip). All W tips were conditioned and checked using a clean Au (111) surface before each measurement. Topographic images were acquired in a constant current mode with a bias voltage applied to samples. All the spectroscopies were obtained using a lock-in amplifier with bias modulation V_{rms} = 20 mV at 977 Hz. Point spectroscopies, line spectroscopies, and Current-Imaging-Tunneling-Spectroscopy (CITS) were collected at particular single point, along a defined line, and over a grid of pixels at bias ranges around Fermi level using the same lock-in amplifier parameters, respectively.

The data analysis related to structure-property correlation was achieved using the deep kernel learning (DKL) framework. The DKL consists of a deep neural network (DNN) in combination with a Gaussian Process (GP) based regressor. The DNN consisted of three layers with the first, second, and third layers containing 64, 64, and 2 neurons respectively. The output of the last layer was treated as inputs to the GP regression. The inputs for the DKL were feature vectors extracted from the STM morphology image. This was trained against a suitable property scalar that was processed from the spectroscopic data. During the active learning process, the upper confidence bound acquisition function (UCB) was utilized to guide experimental exploration. In

the UCB method, the β parameter was annealed in the range of 10 – 0.001, with a 10 % reduction in every successive iteration. Open-source python packages Atomai (https://github.com/pycroscopy/atomai) was used for image processing and feature extraction, while Gpax (https://github.com/ziatdinovmax/gpax) was used for the DKL-based training and GP regression. These were integrated with LabVIEW programs to access the STM controls.

The integration of the dI/dV hyperspectral image from CITS was carried out in custom python 3.9.12 code. At each topological point, the dI/dV signals were added together for all the bias slices within the bias range and then normalized based on the number of slices included. Then the matrix of the signal was utilized to construct a pseudo-color image. The upper limits of the images were manually selected to maximize the number of features shown in the image.

Density functional theory (DFT) calculations are performed using the projector augmented-wave (PAW) method as implemented in Vienna *ab initio* simulation package (VASP)[68,69]. The exchange correlation energy is described by the generalized gradient approximation (GGA) of Perdew-Burke-Ernzerhof (PBE) functional[182]. The valence configurations for each element are $5s^2 5p^6 6s^2 4f^7$ for Eu, $3d^{10}4s^2$ for Zn, and $4s^2 4p^3$ for As. To accurately describe the Coulomb correlations of the *f* orbitals, we use the spherically averaged DFT+U[183] with an on-site Coulomb interaction *U* of 6 eV. The cutoff of kinetic energy for plane wave expansion is set to 520 eV and the atoms are relaxed until the Hellmann-Feynman forces on each atom is below 0.01 eV/Å. We start from the five-atom primitive cell of bulk $EuZn_2As_2$ [as illustrated in Fig. 1(a)], and double the cell size by expanding the lattice parameter *c* by a factor of two, yielding a ten-atom unit cell for simulations. A Γ-centered **k**-point mesh of 7×7×2 is used to

sample the Brillouin zone of this unit cell. To verify whether the slab is thick enough to prevent interactions between the two surfaces in the slab geometry, we look at the projected density of states (PDOS) at each atomic layer plot. Additionally, we verified that PDOS at the surface will not change after adding more layers, confirming the validity of our slab model for surface calculations. Lattice constants of $EuZn_2As_2$ unit cell are optimized to be $a = b = 4.25$ Å, and $c = 14.47$ Å, in good agreement with the experimental values ($a = b = 4.2$ Å, and $c = 14.4$ Å).

The unit cell of $EuZn_2As_2$ contains two Eu atomic layers along the [001] direction, which are denoted as a "double layer" hereafter. The magnetic configuration considered in the calculations is type-A antiferromagnetic with interlayer spins aligned antiparallelly along the *c* axis and intralayer spins aligned parallelly. We study the (001) surface of $EuZn_2As_2$ and two surfaces can be distinguished: As- and Eu-terminated surfaces. By stacking *seven* unit cells of $EuZn_2As_2$ along the [001] direction, followed by removing the both top and bottom AsZn layers, and an inclusion of vacuum along [001] with a thickness of 15 Å, we create a slab with two Eu-terminated surfaces. By further removing the outer Eu layer from both the top and the bottom surface of the slab, while keeping the vacuum thickness the same, we create an As-terminated slab. We use the **k**-point grid of 7×7×1 for all pristine surface calculations in the described slab geometry. To incorporate the substitutional surface defects in the slab and to reduce the impacts of the finite-size effect, we create a 3×3×1 supercell for both terminations based on the previous slab geometry (576 atoms and 594 atoms for As- and Eu-terminated slabs, respectively) and introduce *one* defect on each surface of this 3×3×1 supercell. The calculations for these larger supercells are performed using a single **k**-point at Γ. STM simulations are visualized using the p4vasp software package[70].

6.3 Influence of Heterogeneities on the Surface Electronic Structures of $EuZn_2As_2$

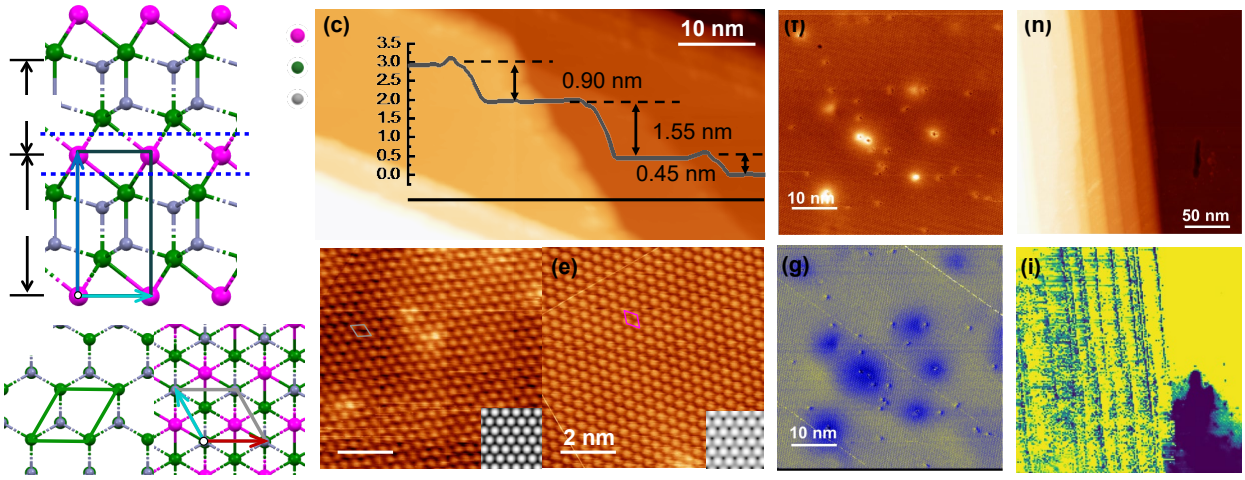

Figure 6-1. **Crystal structure and morphology of $EuZn_2As_2$. (a)** Sideview of the $EuZn_2As_2$ crystal structure. Two blue dashed lines represent possible terminations: Eu (magenta balls) and AsZn (green and grey balls). The black rectangle represents the unit cell in the ***b*** and ***c*** directions. **(b)** Top view of the AsZn and Eu terminations. The *ab*-plane unit cells are represented with solid green and gray parallelograms. **(c)** A large-scale STM topography of $EuZn_2As_2$ showing multiple steps and terraces with various step heights (V_{bias} = -1.5 V, I_t = 50 pA). The line profile along the black line is shown as an overlay. **(d)** and **(e)** STM images of the AsZn (d) and Eu (e) terminations with marked unit cells. V_{bias} = -1.5 V, I_t = 20 and 70 pA, respectively. Their simulated STM are presented as insets. **(f)** A typical high-resolution STM topography of the AsZn surface (V_{bias} = -1.5 V, I_t = 50 pA) with defects. **(g)** STS map collected simultaneously with (f). **(h)** An STM topography of $EuZn_2As_2$ with steps and terraces. **(i)** Integrated empty states image between 0 V and 1.5 V collected within the same area as (h).

$EuZn_2As_2$ crystallizes in a trigonal structure with the space group P-3*m*1 (No. 164) with lattice constants of $a = b = 0.42$ nm, and $c = 0.72$ nm.[180] Fig. 6-1(a) shows the ball and stick model of $EuZn_2As_2$ in the *bc* plane, showing that the AsZn slab is separated by Eu along the *c* direction. When a crystal is cleaved, the bonds between Eu (magenta) and As (green) atoms are expected to break, at the positions indicated by the two blue dashed lines in Fig. 6-1(a). This is because the Eu-As bonding (with a bond length of 0.31 nm) is weaker compared to the As-Zn bonding (with a

bond length of 0.25 nm).[180] With two possible terminations shown in Fig. 6-1(b), Eu or AsZn, step heights of 0.72 nm, or 0.48 nm, or their multiples could be observed. If only one termination were present, the step height is expected to be 0.72 nm or its multiples. Fig. 6-1(c) presents an STM image of $EuZn_2As_2$ after an *in situ* cleavage at 77 K. By scanning along the black line, we obtain the line profile as shown in Fig. 6-1(c). It is obvious that multiple terraces with different step heights are present. Identifying the terminations of these terraces is a nontrivial task, as both the AsZn and Eu terminations have the same lattice constant and symmetry as illustrated in Fig. 6-1(b). Figs. 6-1(d) and 6-1(e) show the STM images with atomic resolution. Through the presence of the unique defects combined with DFT calculations for the AsZn and Eu terminations, we identify that Fig. 6-1(d) is the AsZn surface while Fig. 6-1(e) is the Eu surface, with details described below.

As can be seen from Figs. 6-1(d) and 6-1(e), there are defects at the cleaved surfaces, such as steps generated during cleavage, surface imperfections including absorbates, substitute atoms, vacancies, and scan-induced damage. Fig. 6-1(f) shows a large-scale surface morphology of $EuZn_2As_2$ with atomic resolution, where defects are clearly seen. Fig. 6-1(g) is the STS map collected simultaneously with the STM image shown in Fig. 6-1(f). Note that atomic-level defects can drastically alter the surrounding electronic structure as indicated in blue "clouds" in the STS image with an affecting area of nearly 10 nm × 10 nm. To better illustrate the defects-induced surface electronic property changes, a much larger area of STM and STS images of $EuZn_2As_2$ are shown in Figs. 6-1(h) and 6-1(i), respectively. From these images, multiple step heights are clearly seen, reflecting the presence of both terminations. Note that blue contrast extends beyond step edges, spreading into terraces and appears around defects (on the right large terrace). In brief, the

influence of imperfections on the surface overwhelms the electronic properties over a much larger area than the physical extent of the defects. As such, it is difficult to distinguish the two possible surface terminations using conventional STM and STS imaging techniques.

6.4 Termination Identification Using Substitutional Defects

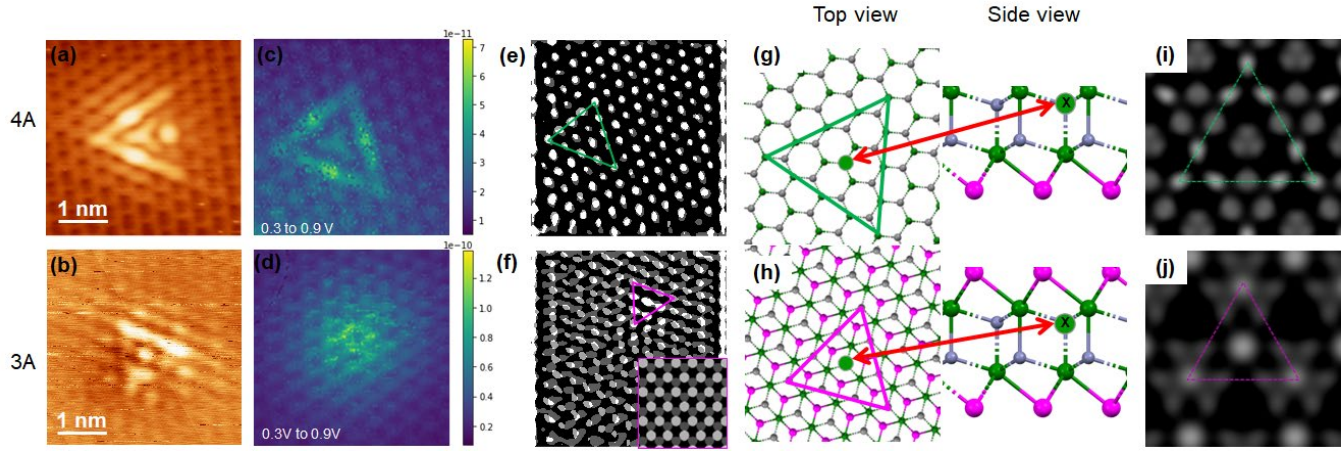

Figure 6-2. STM images, electronic properties, and structure models of the substitutional defects. STM images of **(a)** 4A and **(b)** 3A defects (set point: V_{bias} = -1.5 V, I_t = 50 pA). **(c-d)** Normalized integrated empty states from 0.3 V to 0.9 V of the 4A and 3A defects, respectively. Note the scale difference in the two-color bars. **(e-f)** Comparison of the superimpositions of two STS slices at 1.5 V and 1.075 V (50% transparency) from CITS maps, for 4A and 3A defects, respectively. The superposition of simulated STM images at 2 V and 1 V (65% transparency) of Eu termination is shown as an inset in (f). **(g-h)** Top and side view of the structure model of the 4A and 3A defects (see text for details). Red arrows point to the positions of the defected atoms (atoms with cross). **(i-j)** Simulated STM images for the corresponding 4A and 3A defects at 1 V, respectively.

It is observed that a special group of substitutional defects can be used to differentiate the terminations because of their exclusivity on terminations, although the ascription of the terminations still cannot be identified only with the experimental data. Different from other structural defects like step edges or surface adsorbates, this group of equilateral-triangular-shaped defects, shows a modification to the local density of empty states around the defect (Figs. 6-2 and

6-3). Using the morphology and spectroscopy observations of the substitutional defects as inputs, deep kernel learning (DKL) software[184,185] was used to survey the surface to establish statistics on the correlations between the defects and the local surface termination (i.e., particular kind of terrace) This DKL method enables much faster acquisition of structure-property correlations compared to the traditional operator-driven modes. Coexistence of 3A defects (equilateral-triangular-shaped defects with three-atomic lengths) and 4A defects (equilateral-triangular-shaped defects with four-atomic lengths) on the same surface termination was never observed. However, coexistence of 3A and 3A' defects (see below and Fig. 6-3) was observed on the same terrace, and 4A and 2A' defects (see below and Fig. 6-3) were observed exclusively on the other kind of terrace.

Figs. 6-2(a) and 6-2(b) present STM images with 4A and 3A defects, respectively. Besides their size differences, the sides of the 3A triangle are brighter at the corners while the sides of the 4A triangle feature a bright spot at their center. The 4A defect has a three-pointed star shaped weight center, while the weight center of 3A is a single bright point. The apparent heights of the 4A and 3A defects in the STM images are in the range between 5 and 20 pm, which is too small to be surface adsorbates. For the substitutional defects, the dI/dV maps are integrated over the bias range that shows visible contrast. The data is further normalized by the energy range from 0.3 V to 0.9 V and are shown in Figs. 6-2(c) and 6-2(d) for the 4A and 3A defects, respectively. The triangle shape for 4A remains unchanged through most of the energy slices (Fig. 6-2(c)), while the relative brightness of the 3A defect shifts at different energies resulting in the fuzzy integrated map (Fig. 6-2(d)).

Shown in Fig. 6-2(e) and 6-2(f) are the superimpositions of the STS slices at 1.5 V and 1.075 V (50% transparency) of the surfaces with 4A and 3A defects, respectively. Apparently, the STS maps indicate different bias dependence between 4A and 3A contained surfaces. As outlined with green (Fig. 6-2(e)) and magenta (Fig. 6-2(f)) triangles, the atoms for the two energy slices overlay on top of each other in the whole areas for the surface containing 4A defects. On the contrary, the atoms outside the triangle surprisingly shift at the two energies for the surface containing 3A defects, although the atoms within the magenta triangle overlay each other. This implies that, for the surface surrounding the 3A defects, the visible atoms in STS switch from one element to another between the bias of 1.5 V to 1.075 V, while those within the 3A defect area (magenta triangle) remain unchanged.

To understand the correlations between the defects and terminations, density functional theory (DFT) calculations are performed to sort out the observed distinct features of 4A and 3A defects. The simulated STM images of two pristine $EuZn_2As_2$ surfaces at -1.5 V are shown in the insets of Figs. 6-1(d) and 6-1(e), respectively. Although they look similar, the visible atoms on the AsZn termination are As atoms, while on the Eu termination, they are Zn atoms. Within the experimental bias range, the brightest contrast is always from the As atom for the AsZn termination. But for the Eu termination, the brightest contrast alters from Zn (< 0.5 V) to As (0.5 V – 1.5 V) to Eu (> 1.5 V). The density of states (DOS) switching between 1 V to 2 V is presented in the superimpositions of the two images shown in the inset of Fig. 6-2(f), where the bright atoms alternate from As (1 V) to Eu (2 V). Combining the experiment observation and DFT calculations, we identify the surface with 4A defects as the AsZn termination and the one with 3A defects as

the Eu termination. Being able to identify surfaces is the key towards the study of the surface-state properties of topological materials.

A structure model with a substitutional atomic defect is proposed based on the STM/S signatures on 4A and 3A defects. The model proposes that the observed 4A and 3A defects have the same origin (i.e., an As atom substituting for Zn site), and the 4A and 3A signatures are from the projection of the same substitutional defect on the AsZn and Eu terminations, respectively. The size of the observed triangles is different due to the depth difference of the substitutional atom with respect to the surface. The crossed green atom in the center of the triangle in Figs. 6-2(g) and 2(h) is where the substitutional atom is located (Zn site), the side view shows the depth of the substitution (relative to the surfaces). The follow-up question is what atom occupies the Zn site? In $EuZn_2As_2$, As acts as an electron acceptor and it is unfavorable for either Eu or Zn to replace As. A more feasible scenario is that As is being misplaced, and ultimately acting as an electron donor as well. Considering the radius differences among Eu^{2+} (1.25 Å), As^{3+} (0.7 Å), and Zn^{2+} (0.7 Å), it is likely that As^{3+} can be kinetically misplaced into a Zn^{2+} site such that As functions as an electron donor. This scenario is checked through DFT calculations. The simulated STM images based on the DFT calculations of the corresponding defects are shown in Figs. 6-2(i) and 6-2(j), respectively. Note that the simulated STM images reproduce the main features of the experimental results. DFT based simulations of SM images were also carried out for other substitutional possibilities, none of which resembled the experimental images.

We conducted similar experimental and DFT studies on the surface vacancies. Shown in Fig. 6-3 are two types of vacancy defects marked as 2A' and 3A', respectively. The 2A'-type

vacancy is on the AsZn surface while the 3A'-type vacancy is on the Eu surface based on our assignments above, and the finding of 2A' defects only on the AsZn surface termination with 4A defects, and the finding of 3A' defects only on the Eu surface termination with 3A defects. The line profile across the 2A'-type vacancy gives a height decrease of ~70 pm, indicating a missing atom rather than a substitution. The image of 2A'-type vacancy is bias dependent: it shows a threefold symmetry petal at 1.5 V (see the insert of Fig. 6-3(a)) but a void at -1.5 V (see Fig. 6-3(a)). On the other hand, the 3A'-type vacancy changes from a bright triangle with a hollow center under negative bias (see Figs. 6-3(b) and 6-3(d)) to a uniform dark triangle when turning to a positive bias (Fig. 6-3(f)). Structural models of 2A' defects on the AsZn termination and 3A' defects on the Eu termination are presented in Figs. 6-3(g) and 6-3(h), respectively. Similar to the 4A and 3A defects, the 2A' and 3A'defects have same origin (Zn vacancy), and they are the projection of the Zn vacancy defect on the As-Zn and Eu terminations, respectively.

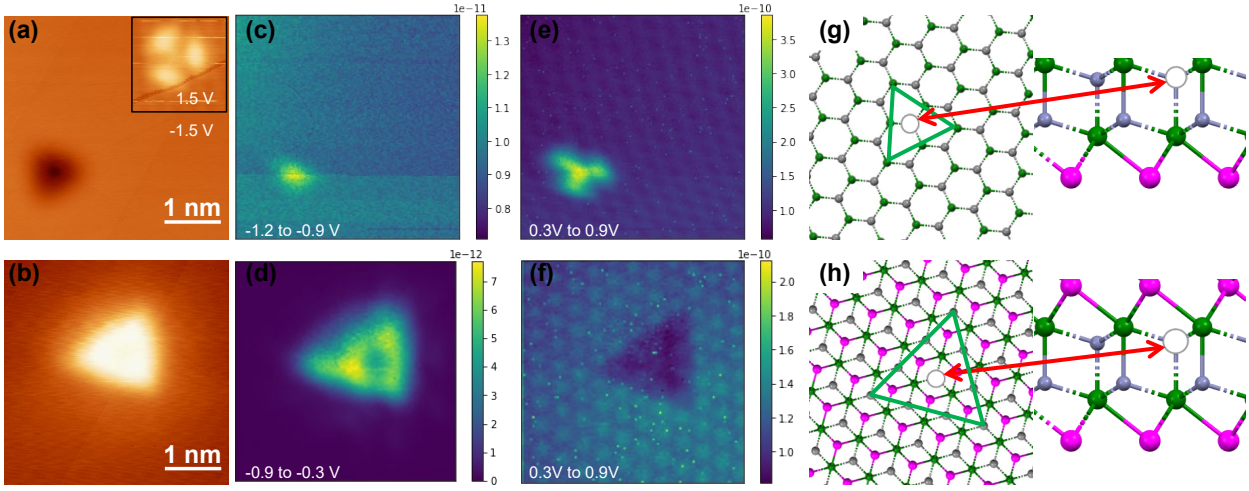

Figure 6-3. STM images, electronic properties, and structure models of vacancy defects. (a-b) STM images of **(a)** 2A' and **(b)** 3A' defects, set point: V_{bias} = -1.5V, I_t = 50pA. **(c-d)** Integrated occupied state maps from -1.2 V to -0.9 V for 2A' and from -0.9 V to -0.3 V for 3A' defects, respectively. **(e-f)** Integrated empty state maps from 0.9 V to 0.3 V for 2A' and 3A' defects, respectively. **(g-h)** Top and side view of the structure models of the vacancy defects (see text for details). Red arrows point to the positions of the defect location (white hollowed atom).

6.5 Electronic Properties of the Defects and Two Terminations of $EuZn_2As_2$

According to first-principles calculations, bulk $EuZn_2As_2$ is expected to be semiconducting with a small bandgap (~ 30 meV).[186] Having identified the surfaces, we can now probe the surface conductance in each case. Fig. 6-4(a) displays the averaged dI/dV spectra collected through continuous imaging tunneling spectroscopy (CITS) at two pristine surfaces as well as defected areas on a linear scale. For easy comparison, we also replot the data on a log scale in Fig. 6-4(b). Remarkably, both the pristine Eu and AsZn surfaces reveal zero conductance between -1 V and +0.5 V in the conductance band. This clearly indicates that the pristine surfaces of $EuZn_2As_2$ are insulating with ~1.5 V bandgap. While structural defects on the surface extend the gap in the conductance band to above 0.6 V (yellow curve in Fig. 6-4(b)), the substitutional (3A and 4A) and

vacancy (2A' and 3A') defects presented above considerably reduce the bandgap width. Especially, on the AsZn surface, the conductance band edge is lowered by the substitutional and vacancy defects 4A and 2A' to around 0.3 V (0.29 V for 2A', and 0.32 V for 4A), while the valence band edge remains unchanged. On the Eu surface, both the 3A- and 3A'-type defects drastically change the band gap widths through both valence and conductance band edges. For 3A (the black curve in Figs. 6-4(a)-(c)), the band gap is 0.9 V, with band edges as – 0.65 V and +0.28 V; for 3A' (the red curve in Fig. 6-4(a)-(c)), the band gap is 0.4 V, with band edges as – 0.34 V and +0.05 V.

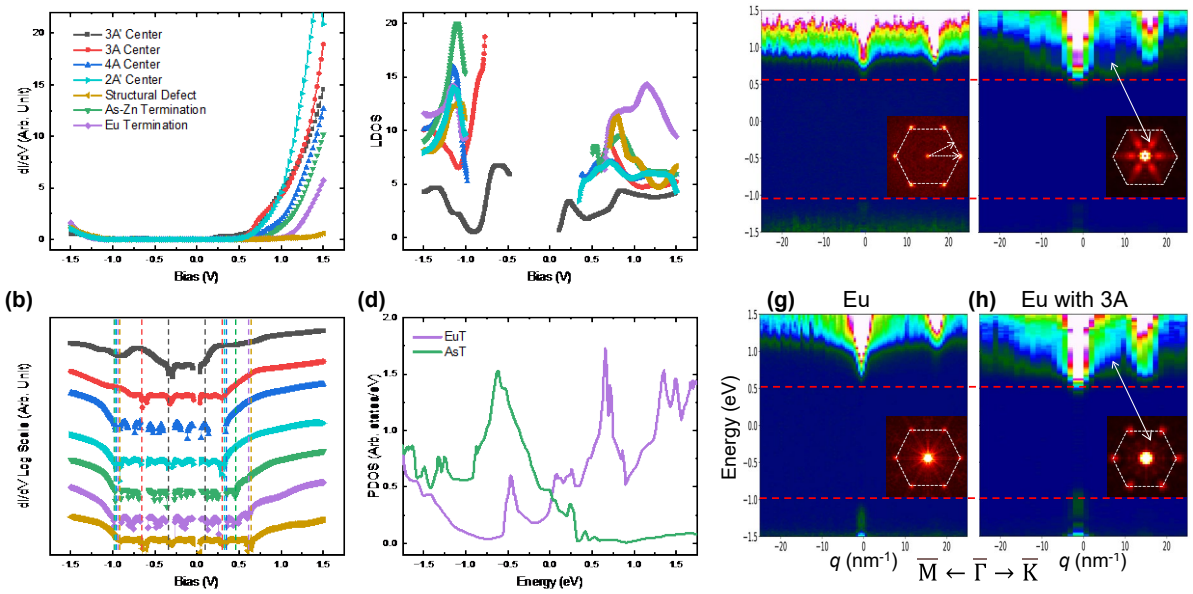

Figure 6-4. Influence of heterogeneities on the surface electronic structures and QPI comparison of the two terminations and defects. (a) Averaged STS spectra comparison of the two pristine surfaces, the two substitutional defects (3A and 4A), two vacancy defects (2A' and 3A'), and an area with structural defects. CITS set point: V_{bias} = -1.5 V, I_t = 200 pA. **(b)** STS spectra in (a) represented on a semi-log scale. Note the bandgap edges are marked by dashed lines. **(c)** Average local density of states (LDOS) derived from (a). **(d)** DFT calculated projected density of states (PDOS) of the two pristine terminations. (e-h) Energy vs. QPI signal in $\overline{M} - \overline{\Gamma} - \overline{K}$ directions for the pristine AsZn **(e)**, AsZn and with 4A defect **(f)**, pristine Eu **(g)**, Eu with 3A **(h)** defects, respectively. QPI maps from the FFT of the CITS are shown in the insets, energy at 1 V.

The bandgap width decreases by the presence of 4A and 3A defects are also shown in the quasiparticle interference (QPI) maps acquired from the fast Fourier transformation (FFT) of STS maps. The QPI analysis is conducted in the energy range between -1.5 V and +1.5 V, with the 25 mV energy intervals. The momentum maps are shown in Figs. 6-4 (e) and 6-4(g), with the QPI map obtained from the STS map at 0.6 V shown in the insets, respectively. The red dotted lines mark the valence and conductance band edges of the pristine surfaces. The penetration of the states into the gap is clearly shown in Figs. 6-4(f) and 6-4(h) for defected surfaces. The reciprocal lattice points of the atomic lattice are observable at $q_x \approx 17.4$ nm $^{-1}$, which is consistent with the atomic resolution STM images. QPI maps show similar dispersing signal at $\bar{\Gamma}$ for all cases, but additional QPI signal at $q \approx 8.7$ nm $^{-1}$ along the $\bar{\Gamma}$-$\bar{K}$ direction is found for the surface containing 4A defects, which corresponds to a new state inside the Brillouin zone. It occurs in the energy range of 0.5 ~ 1.5 eV as shown in Fig. 6-4(f), marked by white arrows, from the interference of scattered quasiparticles. This indicates that the surface-projected electronic structure strongly depends on the specific defects. We consider that defects affect the scattering potentials that influence the relative intensity between the scattering wavevectors, which even modify the surface band structure with new scattering wavevectors.

It is apparent that the decrease of the bandgap by substitutional and vacancy defects is in the compensation of the DOS away from the Fermi level. The LDOS, calculated from $(dI/dV)/(I/V)$ in Fig. 6-4(c), shows the comparison of the DOS changes of various cases. The two pristine terminations show the highest filled state peak (AsZn, green, -1.1 V) and the highest empty state

peak (Eu, purple, +1.2 V). This trend is consistent with the DFT calculated projected density of state (PDOS) shown in Fig. 6-4(d). The presence of the defects suppresses those peaks and pushes more states into the bandgap, forming in-gap states.

According to experimental investigations, $EuCd_2As_2$ shows semimetallic behavior when the hole concentration is high[167,169] but is semiconducting when the hole concentration is low.[174-177] Bulk $EuZn_2As_2$ is also hole dominant[180] with nontrivial topological bands.[187] If the $EuZn_2As_2$ pristine surfaces preserve the same properties as that in the bulk, one expects that Zn vacancies introduce additional holes into the system. For As substitution into Zn sites, the situation is less clear. From the chemistry point of view (both ionic size and Zn function), As in the Zn site should behave as As^{3+}. The replacement of Zn^{2+} by As^{3+} will introduce an extra electron, thus reducing the overall hole concentration. Surprisingly, both substitutional and vacancy defects reduce the bandgap size regardless of the nature of the defects-induced carriers. What is more remarkable is that defects-induced bandgap modification is much more dramatic on the Eu surface than that on the AsZn surface: (1) the bandgap in the area around the Zn vacancy on the Eu surface is 0.4 V but 1.3 V on the AsZn surface, and (2) the gap measured in the As substituted area is 0.9 V on the Eu surface but 1.3 V on the AsZn surface. This implies that the Eu layer plays an extremely important role in the electronic properties of $EuZn_2As_2$.

According to Ref. [169], nontrivial topological bands were obtained by ARPES in the temperature window between 11 K and 17 K, which is just above T_N of $EuCd_2As_2$. The band splitting results from strong spin fluctuation, thus regarded as the Weyl state.[1] However, between 11 K and 17 K, the resistivity shows clearly non-metallic behavior,[1] which makes one consider

that the Wely cone observed in ARPES reflects the surface state of $EuCd_2As_2$. For $EuZn_2As_2$, our experimental data shown in Figure 6-4 shows no sign of the topological electronic structure at 77 K. Given that the resistivity increases with decreasing temperature between T_N (~19 K) and 77 K,[180,181] it is unlikely that the surface gap size reduces when approaching T_N. Based on the quantitative analysis of defects effects to the LDOS, the gap size is greatly reduced with the defects in the Eu layer (3A and 3A') than that in the AsZn layer (4A and 2A') (see Figure 6-4(b)). Within the Eu layer, the vacancy (3A') results in a much smaller gap size than the As defect (3A). This confirms the strong interplay between electronic properties and magnetism even at 77 K and the vacancy makes much greater suppression of local magnetic interaction than the As defect. The fact that defects in the Eu layer alter both valence and conduction bands further indicates the important contribution of local magnetism to LDOS, compared with the defects in the AsZn layer which only lower down the conduction states. With the understanding of defects' effects on two different surfaces, we can now reconcile the discrepancy between the LDOS distribution for both the pristine AsZn and Eu surfaces and the calculated PDOS shown in Fig. 6-4(d). Our calculations were based on the A-type antiferromagnetically ordered state at 0 K for a slab with a clean and non-reconstructed surface. In our structural model, the unsaturated dangling bonds from a sharp cut of the surface tend to give in-gap surface states, yielding a conductive surface from calculations. Normally, calculated results can be used to compare with experimentally obtained results at finite temperatures such as electronic structure, defects effects, and structural parameters. Given that spin fluctuation plays an important role above T_N of $EuZn_2As_2$ as discussed above, calculations by including spin fluctuation are needed.

6.6 Multiscale Defect Discovery via Deep-Kernal Learning[184,185,188]

Prior to the implementation of the DKL, CITS was performed regularly to assess the impact of surface defects on the LDOS. The initial understanding was that finding a pristine surface area to conduct CITS to get a good representation of the LDOS of different areas and then separating them later into two terminations. The DKL was implemented at first to find avoid various surface adsorbate defects. In the experiment, the structural input is extracted from the STM topography while the scalar property is derived from spectroscopic measurements. In our implementation, each experiment begins with an initial set of 20 data points randomly measured across the region following which the DKL model is deployed. At each iteration, the previous set of experimental observations serves as the training data. The DKL prediction is used to derive the acquisition function[189], which is dynamically incorporated into the STM for each successive measurement. The experiment continues until a set of iterations is complete. We found that the pristine surface by implementing DKL to identify the adsorbate defects which extend the bandgap surrounding the physical extends of themselves. The bandgap (E_g) was estimated from the conductivity vs. bias (dI/dV vs V) spectrum. The valence and the conduction band edges were determined by fitting a slope at the two sides of the spectrum where the signal starts to increase from the stateless gap. By setting the scalar to the bandgap observed in STS spectrum and setting new area to minimize the scalar. For the reproducibility survey of substitutional defects, similar scalar was used to locate the defects since they are reducing the bandgap. For vacancy defects, the scalar was set to:

$$scalar = \frac{Area\,(\frac{dI}{dV}\ for\ V = [0,\ 0.5])}{Area\,(\frac{dI}{dV}\ for\ V = [0,\ 1.5])} = \frac{\int_0^{0.5} GdV}{\int_0^{1.5} GdV}$$

which essentially defines the state ratio between 0 to 0.5V and 0 to 1.5V because we found a non-trivial initial increase in conductance at lower bias from the STS spectra on vacancy defects.

6.7 Summary

We have investigated the surface electronic properties of $EuZn_2As_2$ using STM/S. The surfaces were created by cleaving $EuZn_2As_2$ single crystals at 77 K and studied at the same temperature. Two surfaces, Eu- and AsZn-terminated, with identical surface structures, were identified through defect-induced LDOS changes, which are confirmed by DFT simulations. Several properties were observed: (1) both Eu and AsZn pristine surfaces are insulating with a bandgap around 1.5 eV at 77 K, (2) the surface bandgap is dramatically reduced due to defects located in the Zn site, either Zn vacancy or As substitution, and (3) defect-induced LDOS changes are much more impactful on the Eu surface than on the AsZn surface, implying the importance of local magnetic interaction to the electronic properties since only Eu is magnetic. This is why our experimental results obtained at 77 K cannot be explained by DFT calculations for T = 0 K with an A-type antiferromagnetic ordering. Spin fluctuation should be considered in the calculation for electronic structures above T_n. The work presented here forms a basis to identify Eu terminations efficiently for future STM experiments. Our ongoing STM/S experiments conducted below T_n shows an absence of bandgaps, which indicates that the antiferromagnetic ordering of $EuZn_2As_2$ surface states can be assessed without hindrance at 4 K. Future work on spin-polarized STM/S will further our understanding of the magnetic configuration of surface Eu atoms, and its interplay with structural defects.

Chapter 7. Reference

1 Schwach, P., Pan, X. L. & Bao, X. H. Direct Conversion of Methane to Value-Added Chemicals over Heterogeneous Catalysts: Challenges and Prospects. *Chem Rev* **117**, 8497-8520 (2017).

2 Liu, L. C. & Corma, A. Isolated metal atoms and clusters for alkane activation: Translating knowledge from enzymatic and homogeneous to heterogeneous systems. *Chem-Us* **7**, 2347-2384 (2021).

3 Donald, S. B., Navin, J. K. & Harrison, I. Methane dissociative chemisorption and detailed balance on Pt(111): Dynamical constraints and the modest influence of tunneling. *J Chem Phys* **139** (2013).

4 Navin, J. K., Donald, S. B. & Harrison, I. Angle-Resolved Thermal Dissociative Sticking of Light Alkanes on Pt(111): Transitioning from Dynamical to Statistical Behavior. *J Phys Chem C* **118**, 22003-22011 (2014).

5 Cushing, G. W., Johanek, V., Navin, J. K. & Harrison, I. Graphene Growth on Pt(111) by Ethylene Chemical Vapor Deposition at Surface Temperatures near 1000 K. *J Phys Chem C* **119**, 4759-4768 (2015).

6 Johanek, V., Cushing, G. W., Navin, J. K. & Harrison, I. Real-time observation of graphene oxidation on Pt(111) by low-energy electron microscopy. *Surf Sci* **644**, 165-169 (2016).

7 Wang, X. *Light Alkane Activation on Rh(111), an Imperfectly Perfect Surface*, University of Virginia.

8 Rasheed, M. W., Mahboob, A. & Hanif, I. Investigating the properties of octane isomers by novel neighborhood product degree-based topological indices. *Frontiers in Physics* **12** (2024).

9 Islam, M. M., Catlow, C. R. A. & Roldan, A. Mechanistic Pathways for the Dehydrogenation of Alkanes on Pt(111) and Ru(0001) Surfaces. *ChemCatChem* **16**, e202301386 (2024).

10 Eldridge, T. J. *Alkane Activation on Pt(111): Thermal Kinetics, Thermodynamics, and the Role of Van Der Waals Interactions*, University of Virginia, (2018).

11 Johnson, D. F. & Weinberg, W. H. Quantification of the Selective Activation of C-C Bonds in Short-Chain Alkanes - Reactivity of Ethane, Propane, Isobutane, N-Butane and Neopentane on Ir(111). *J Chem Soc Faraday T* **91**, 3695-3702 (1995).

12 Xu, H., Yuro, R. & Harrison, I. STM investigation of hot bromine atom chemistry on Pt(111). *P Soc Photo-Opt Ins* **3272**, 73-83 (1998).

13 Schwendemann, T. C., Samanta, I., Kunstmann, T. & Harrison, I. Ordered methyl bromide monolayer on Pt(111). *Abstr Pap Am Chem S* **230**, U1211-U1212 (2005).

14 Schwendemann, T. C., Samanta, I., Kunstmann, T. & Harrison, I. CH3Br structures on Pt(111): Kinetically controlled self-assembly of weakly adsorbed dipolar molecules. *J Phys Chem C* **111**, 1347-1354 (2007).

15 Fivaz, R. & Mooser, E. Mobility of Charge Carriers in Semiconducting Layer Structures. *Phys Rev* **163**, 743-755 (1967).

16 Zhu, T. H. *et al.* Transport properties of few-layer $NbSe_2$: From electronic structure to thermoelectric properties. *Mater Today Phys* **27** (2022).
17 Fu, M. M. *et al.* Defects in Highly Anisotropic Transition-Metal Dichalcogenide PdSe2. *J Phys Chem Lett* **11**, 740-+ (2020).
18 Gao, N., Guo, Y., Zhou, S., Bai, Y. Z. & Zhao, J. J. Structures and Magnetic Properties of MoS_2 Grain Boundaries with Antisite Defects. *J Phys Chem C* **121**, 12261-12269 (2017).
19 Moody, G. *et al.* Microsecond Valley Lifetime of Defect-Bound Excitons in Monolayer WSe_2. *Phys Rev Lett* **121** (2018).
20 Yuan, S. J., Roldán, R., Katsnelson, M. I. & Guinea, F. Effect of point defects on the optical and transport properties of MoS_2 and WS_2. *Phys Rev B* **90** (2014).
21 Shen, W., Qiao, L., Ding, J. & Sui, Y. M. Constructing 1 T-2 H TaS2 nanosheets with architecture and defect engineering for enhance hydrogen evolution reaction. *J Alloy Compd* **935** (2023).
22 Voiry, D., Yang, J. & Chhowalla, M. Recent Strategies for Improving the Catalytic Activity of 2D TMD Nanosheets Toward the Hydrogen Evolution Reaction. *Adv Mater* **28**, 6197-6206 (2016).
23 Pedersen, P. D., Vegge, T., Bligaard, T. & Hansen, H. A. Trends in CO2 Reduction on Transition Metal Dichalcogenide Edges. *Acs Catal* **13**, 2341-2350 (2023).
24 Shi, Y. M., Li, H. N. & Li, L. J. Recent advances in controlled synthesis of two-dimensional transition metal dichalcogenides vapour deposition techniques. *Chem Soc Rev* **44**, 2744-2756 (2015).
25 Cavallini, M. & Gentili, D. Atomic Vacancies in Transition Metal Dichalcogenides: Properties, Fabrication, and Limits. *Chempluschem* **87** (2022).
26 Blades, W. H., Frady, N. J., Litwin, P. M., McDonnell, S. J. & Reinke, P. Thermally Induced Defects on WSe_2. *J Phys Chem C* **124**, 15337-15346 (2020).
27 Zhu, H. *et al.* Defects and Surface Structural Stability of $MoTe_2$ Under Vacuum Annealing. *Acs Nano* **11**, 11005-11014 (2017).
28 Komsa, H. P. *et al.* Two-Dimensional Transition Metal Dichalcogenides under Electron Irradiation: Defect Production and Doping. *Phys Rev Lett* **109** (2012).
29 Barja, S. *et al.* Identifying substitutional oxygen as a prolific point defect in monolayer transition metal dichalcogenides. *Nat Commun* **10** (2019).
30 Cao, D., Shen, T., Liang, P., Chen, X. & Shu, H. Role of Chemical Potential in Flake Shape and Edge Properties of Monolayer MoS2. *The Journal of Physical Chemistry C* **119**, 4294-4301 (2015).
31 Salazar, N., Rangarajan, S., Rodriguez-Fernandez, J., Mavrikakis, M. & Lauritsen, J. V. Site-dependent reactivity of MoS2 nanoparticles in hydrodesulfurization of thiophene. *Nat Commun* **11** (2020).
32 Binnig, G. & Rohrer, H. Scanning Tunneling Microscopy. *Helv Phys Acta* **55**, 726-735 (1982).
33 Fischer, Ø., Kugler, M., Maggio-Aprile, I., Berthod, C. & Renner, C. Scanning tunneling spectroscopy of high-temperature superconductors. *Reviews of Modern Physics* **79**, 353 (2007).

34 Kim, J.-J. *et al.* Observation of a phase transition from the T phase to the H phase induced by a STM tip in 1 T− TaS 2. *Physical Review B* **56**, R15573 (1997).
35 Zhang, J., Liu, J., Huang, J. L., Kim, P. & Lieber, C. M. Creation of nanocrystals through a solid-solid phase transition induced by an STM tip. *Science* **274**, 757-760 (1996).
36 Li, L. F. *et al.* Chemically identifying single adatoms with single-bond sensitivity during oxidation reactions of borophene. *Nat Commun* **13** (2022).
37 Merino, P., Grosse, C., Roslawska, A., Kuhnke, K. & Kern, K. Exciton dynamics of C_{60}-based single-photon emitters explored by Hanbury Brown-Twiss scanning tunnelling microscopy. *Nat Commun* **6** (2015).
38 Gordon, O. *et al.* Scanning tunneling state recognition with multi-class neural network ensembles. *Rev Sci Instrum* **90** (2019).
39 Gordon, O. M., Junqueira, F. L. Q. & Moriarty, P. J. Embedding human heuristics in machine-learning-enabled probe microscopy. *Mach Learn-Sci Techn* **1** (2020).
40 Chen, F. X. R. *et al.* Deep learning based atomic defect detection framework for two-dimensional materials. *Sci Data* **10** (2023).
41 Yothers, M. P., Browder, A. E. & Bumm, L. A. Real-space post-processing correction of thermal drift and piezoelectric actuator nonlinearities in scanning tunneling microscope images. *Rev Sci Instrum* **88** (2017).
42 Krull, A., Hirsch, P., Rother, C., Schiffrin, A. & Krull, C. Artificial-intelligence-driven scanning probe microscopy. *Commun Phys-Uk* **3** (2020).
43 Liu, Y. *et al.* Learning the right channel in multimodal imaging: automated experiment in piezoresponse force microscopy. *npj Computational Materials* **9**, 34 (2023).
44 Roccapriore, K. M., Kalinin, S. V. & Ziatdinov, M. Physics discovery in nanoplasmonic systems via autonomous experiments in scanning transmission electron microscopy. *Advanced Science* **9**, 2203422 (2022).
45 Magda, G. Z. *et al.* Exfoliation of large-area transition metal chalcogenide single layers. *Sci Rep-Uk* **5** (2015).
46 Huang, Y. *et al.* Universal mechanical exfoliation of large-area 2D crystals. *Nat Commun* **11** (2020).
47 Tian, S. *et al.* Controllable Edge Oxidation and Bubbling Exfoliation Enable the Fabrication of High Quality Water Dispersible Graphene. *Sci Rep-Uk* **6**, 34127 (2016).
48 Li, Z. *et al.* Mechanisms of Liquid-Phase Exfoliation for the Production of Graphene. *Acs Nano* **14**, 10976-10985 (2020).
49 Achee, T. C. *et al.* High-yield scalable graphene nanosheet production from compressed graphite using electrochemical exfoliation. *Sci Rep-Uk* **8**, 14525 (2018).
50 Linstrom, P. J. & Mallard, W. G. The NIST Chemistry WebBook: A chemical data resource on the internet. *J Chem Eng Data* **46**, 1059-1063 (2001).
51 Muller, E. W. & Bahadur, K. Field Ionization of Gases at a Metal Surface and the Resolution of the Field Ion Microscope. *Phys Rev* **102**, 624-631 (1956).
52 Cavallini, M. & Biscarini, F. Electrochemically etched nickel tips for spin polarized scanning tunneling microscopy. *Rev Sci Instrum* **71**, 4457-4460 (2000).
53 Wintterlin, J. *et al.* Atomic-Resolution Imaging of Close-Packed Metal-Surfaces by Scanning Tunneling Microscopy. *Phys Rev Lett* **62**, 59-62 (1989).

54 Binh, V. T. & Garcia, N. Atomic Metallic Ion Emission, Field Surface Melting and Scanning Tunneling Microscopy Tips. *J Phys I* **1**, 605-612 (1991).
55 Binh, V. T., Purcell, S. T., Gardet, G. & Garcia, N. Local Heating of Single-Atom Protrusion Tips during Field Electron-Emission. *Surf Sci* **279**, L197-L201 (1992).
56 Binnig, G., Rohrer, H., Gerber, C. & Weibel, E. 7x7 Reconstruction on Si(111) Resolved in Real Space. *Phys Rev Lett* **50**, 120-123 (1983).
57 Tersoff, J. & Hamann, D. R. Theory of the Scanning Tunneling Microscope. *Phys Rev B* **31**, 805-813 (1985).
58 Stroscio, J. A. & Feenstra, R. M. in *Methods in Experimental Physics* Vol. 27 (eds Joseph A. Stroscio & William J. Kaiser) 95-147 (Academic Press, 1993).
59 Hamers, R. J., Tromp, R. M. & Demuth, J. E. Surface Electronic-Structure of Si(111)-(7 X 7) Resolved in Real Space. *Phys Rev Lett* **56**, 1972-1975 (1986).
60 Bardeen, J. Tunnelling from a Many-Particle Point of View. *Phys Rev Lett* **6**, 57-& (1961).
61 Feenstra, R. M. Tunneling Spectroscopy of the (110)-Surface of Direct-Gap Iii-V Semiconductors. *Phys Rev B* **50**, 4561-4570 (1994).
62 Feenstra, R. M. Tunneling spectroscopy of the Si(111)2x1 surface. *Phys Rev B* **60**, 4478-4480 (1999).
63 Gumbel, E. J. The return period of flood flows. *Ann Math Stat* **12**, 163-190 (1941).
64 Hoffman, J. E. *et al.* Imaging quasiparticle interference in $Bi_2Sr_2CaCu_2O_{8+\delta}$. *Science* **297**, 1148-1151 (2002).
65 Allan, M. P. *et al.* Imaging Cooper pairing of heavy fermions in $CeCoIn_5$. *Nat Phys* **9**, 468-473 (2013).
66 Marques, C. A. *et al.* Tomographic mapping of the hidden dimension in quasi-particle interference. *Nat Commun* **12** (2021).
67 Zou, Q. *et al.* Exploration of two surfaces observed in Weyl semimetal BaMnSb2. *Npj Quantum Mater* **7** (2022).
68 Kresse, G. & Hafner, J. Ab-Initio Molecular-Dynamics for Open-Shell Transition-Metals. *Phys Rev B* **48**, 13115-13118 (1993).
69 Kresse, G. & Furthmuller, J. Efficient iterative schemes for ab initio total-energy calculations using a plane-wave basis set. *Phys Rev B* **54**, 11169-11186 (1996).
70 <www.p4vasp.at>
71 Davisson, C. J. & Germer, L. H. Reflection and refraction of electrons by a crystal of nickel. *P Natl Acad Sci USA* **14**, 619-627 (1928).
72 Ogletree, D. F., Vanhove, M. A. & Somorjai, G. A. Leed Intensity Analysis of the Structures of Clean Pt(111) and of Co Adsorbed on Pt(111) in the C(4x2) Arrangement. *Surf Sci* **173**, 351-365 (1986).
73 Johnson, D. F. & Weinberg, W. H. Quantitative-Determination Of The Activity Of Defect Sites On A Single-Crystalline Surface - C-H Bond Activation Of C-13 Labeled Ethane On Ir(111). *J. Chem. Phys.* **101**, 6289-6300 (1994).
74 Hagedorn, C. J., Weiss, M. J., Kim, T. W. & Weinberg, W. H. Trapping-mediated dissociative chemisorption of cycloalkanes on Ru(001) and Ir(111): Influence of ring

strain and molecular geometry on the activation of C-C and C-H bonds. *Journal of the American Chemical Society* **123**, 929-940 (2001).
75 Johnson, D. F. & Weinberg, W. H. QUANTIFICATION OF THE SELECTIVE ACTIVATION OF C-C BONDS IN SHORT-CHAIN ALKANES - REACTIVITY OF ETHANE, PROPANE, ISOBUTANE, N-BUTANE AND NEOPENTANE ON IR(11). *Journal of the Chemical Society-Faraday Transactions* **91**, 3695-3702 (1995).
76 Johnson, D. F. & Weinberg, W. H. Quantification Of The Selective Activation Of C-H Bonds In Short-Chain Alkanes - The Reactivity Of Ethane, Propane, Isobutane, N-Butane, And Neopentane On Ir(111). *J. Chem. Phys.* **103**, 5833-5847 (1995).
77 Kelly, D. & Weinberg, W. H. Trapping-mediated dissociative chemisorption of C3H8 and C3D8 on Ir(110). *J. Chem. Phys.* **105**, 271-278 (1996).
78 Kelly, D. & Weinberg, W. H. Direct dissociative chemisorption of methane, ethane, propane, and cyclopropane on Ir(110). *J. Vac. Sci. Technol. A* **15**, 1663-1666 (1997).
79 Jachimowski, T. A. & Weinberg, W. H. Trapping-mediated dissociative chemisorption of cyclopropane on Ru(001) via C-C bond cleavage. *Surf. Sci.* **370**, 71-76 (1997).
80 Jachimowski, T. A. & Weinberg, W. H. Trapping-mediated dissociative chemisorption of ethane and propane on Ru(001). *Surf. Sci.* **372**, 145-154 (1997).
81 He, R., Cong, S., Wang, J., Liu, J. & Zhang, Y. Porous Graphene Oxide/Porous Organic Polymer Hybrid Nanosheets Functionalized Mixed Matrix Membrane for Efficient CO2 Capture. *Acs Appl Mater Inter* **11**, 4338-4344 (2019).
82 Zhou, M., Zhang, J., Jiang, H. & Chen, R. Controllable synthesis of Pd-zeolitic imidazolate framework-porous graphene oxide (Pd-ZIF-pGO) with enhanced catalytic properties for the reduction of nitroarenes. *Reaction Kinetics, Mechanisms and Catalysis* **135**, 867-879 (2022).
83 Mamba, G. *et al.* State of the art on the photocatalytic applications of graphene based nanostructures: From elimination of hazardous pollutants to disinfection and fuel generation. *Journal of Environmental Chemical Engineering* **8**, 103505 (2020).
84 Moreno, C. *et al.* On-surface synthesis of porous graphene nanoribbons mediated by phenyl migration. *Communications Chemistry* **7**, 219 (2024).
85 Necas, D. & Klapetek, P. Gwyddion: an open-source software for SPM data analysis. *Cent Eur J Phys* **10**, 181-188 (2012).
86 Krupski, K., Moors, M., Jóźwik, P., Kobiela, T. & Krupski, A. Structure Determination of Au on Pt(111) Surface: LEED, STM and DFT Study. *Materials* **8**, 2935-2952 (2015).
87 Bartels, L., Meyer, G. & Rieder, K. H. The evolution of CO adsorption on Cu(111) as studied with bare and CO-functionalized scanning tunneling tips. *Surf Sci* **432**, L621-L626 (1999).
88 Novoselov, K. S. *et al.* Two-dimensional atomic crystals. *P Natl Acad Sci USA* **102**, 10451-10453 (2005).
89 Novoselov, K. S., Mishchenko, A., Carvalho, A. & Neto, A. H. C. 2D materials and van der Waals heterostructures. *Science* **353** (2016).
90 Wu, Y. C., Li, D. F., Wu, C. L., Hwang, H. Y. & Cui, Y. Electrostatic gating and intercalation in 2D materials. *Nat Rev Mater* **8**, 41-53 (2023).

91 Mak, K. F., McGill, K. L., Park, J. & McEuen, P. L. The valley Hall effect in MoS_2 transistors. *Science* **344**, 1489-1492 (2014).
92 Wang, Q. X. *et al.* High-Energy Gain Upconversion in Monolayer Tungsten Disulfide Photodetectors. *Nano Lett* **19**, 5595-5603 (2019).
93 Ippolito, S. *et al.* Covalently interconnected transition metal dichalcogenide networks via defect engineering for high-performance electronic devices. *Nat Nanotechnol* **16**, 592-598 (2021).
94 Loo, A. H., Bonanni, A., Ambrosi, A. & Pumera, M. Molybdenum disulfide (MoS_2) nanoflakes as inherently electroactive labels for DNA hybridization detection. *Nanoscale* **6**, 11971-11975 (2014).
95 Pumera, M. & Loo, A. H. Layered transition-metal dichalcogenides (MoS_2 and WS_2) for sensing and biosensing. *Trac-Trend Anal Chem* **61**, 49-53 (2014).
96 Zhang, G., Liu, H. J., Qu, J. H. & Li, J. H. Two-dimensional layered MoS_2: rational design, properties and electrochemical applications. *Energ Environ Sci* **9**, 1190-1209 (2016).
97 Li, Y. A., Kuang, G. Z., Jiao, Z. J., Yao, L. & Duan, R. H. Recent progress on the mechanical exfoliation of 2D transition metal dichalcogenides. *Mater Res Express* **9** (2022).
98 Schmidt, M., Gooth, J. & Binnewies, M. Preparation and Crystal Growth of Transition Metal Dichalcogenides. *Z Anorg Allg Chem* **646**, 1183-1194 (2020).
99 Habib, M. *et al.* Bridging the gap: an in-depth comparison of CVT-grown layered transition metal dichalcogenides for supercapacitor applications. *Mater Adv* **5**, 1088-1098 (2024).
100 Hou, N. N. *et al.* Fabrication of oxygen-doped $MoSe_2$ hierarchical nanosheets for highly sensitive and selective detection of trace trimethylamine at room temperature in air. *Nano Res* **13**, 1704-1712 (2020).
101 Shawkat, M. S. *et al.* Thickness-Independent Semiconducting-to-Metallic Conversion in Wafer-Scale Two-Dimensional $PtSe_2$ Layers by Plasma-Driven Chalcogen Defect Engineering. *Acs Appl Mater Inter* **12**, 14341-14351 (2020).
102 Tongay, S. *et al.* Defects activated photoluminescence in two-dimensional semiconductors: interplay between bound, charged, and free excitons. *Sci Rep-Uk* **3** (2013).
103 Liu, F. Mechanical exfoliation of large area 2D materials from vdW crystals. *Prog Surf Sci* **96** (2021).
104 Heyl, M. & List-Kratochvil, E. J. W. Only gold can pull this off: mechanical exfoliations of transition metal dichalcogenides beyond scotch tape. *Appl Phys a-Mater* **129** (2023).
105 Poddar, P. K. *et al.* Resist-Free Lithography for Monolayer Transition Metal Dichalcogenides. *Nano Lett* **22**, 726-732 (2022).
106 Mizutani, W., Inukai, J. & Ono, M. Making a Monolayer Hole in a Graphite Surface by Means of a Scanning Tunneling Microscope. *Jpn J Appl Phys 2* **29**, L815-L817 (1990).
107 Parkinson, B. Layer-by-Layer Nanometer Scale Etching of 2-Dimensional Substrates Using the Scanning Tunneling Microscope. *J Am Chem Soc* **112**, 7498-7502 (1990).

108 Delawski, E. & Parkinson, B. A. Layer-by-Layer Etching of 2-Dimensional Metal Chalcogenides with the Atomic Force Microscope. *J Am Chem Soc* **114**, 1661-1667 (1992).

109 Yamaguchi, W., Shiino, O., Sugawara, H., Hasegawa, T. & Kitazawa, K. Surface etching of 1T-TaS2 with the UHV-STM. *Appl Surf Sci* **119**, 67-75 (1997).

110 Kidd, T. E., Gamb, B. I., Skirtachenko, P. I. & Strauss, L. H. Dopant Enhanced Etching of TiSe2 by Scanning Tunneling Microscopy. *Langmuir* **26**, 10980-10984 (2010).

111 Zheng, H. S. *et al.* Electrical Stressing Induced Monolayer Vacancy Island Growth on TiSe2. *Nano Lett* **18**, 2179-2185 (2018).

112 Vey, K., Goschke, R. A., Buslaps, T., Walter, U. & Steglich, F. Stm-Mediated Surface Degradation on 1t-Tas_2. *Surf Sci* **311**, 53-63 (1994).

113 Ko, W., Ma, C., Nguyen, G. D., Kolmer, M. & Li, A.-P. Atomic-Scale Manipulation and In Situ Characterization with Scanning Tunneling Microscopy. *Advanced Functional Materials* **29**, 1903770 (2019).

114 Schindelin, J. *et al.* Fiji: an open-source platform for biological-image analysis. *Nat Methods* **9**, 676-682 (2012).

115 Kirillov, A. *et al.* Segment Anything. *arXiv e-prints*, arXiv:2304.02643 (2023).

116 Meetsma, A., Wiegers, G. A., Haange, R. J. & Deboer, J. L. Structure of 2h-Tas2. *Acta Crystallogr C* **46**, 1598-1599 (1990).

117 Burns, K. *et al.* Tailoring the Angular Mismatch in MoS2 Homobilayers through Deformation Fields. *Small* **19**, 2300098 (2023).

118 Biswas, A. *et al.* Non-Linear Optics at Twist Interfaces in h-BN/SiC Heterostructures. *Adv Mater* **35**, 2304624 (2023).

119 Lee, D. D. & Seung, H. S. in *Proceedings of the 14th International Conference on Neural Information Processing Systems* 535–541 (MIT Press, Denver, CO, 2000).

120 Baradwaj, N. *et al.* Probing phonon focusing, thermomechanical behavior, and moiré patterns in van der Waals architectures using surface acoustic waves. *npj Computational Materials* **10**, 137 (2024).

121 Kenaz, R. *et al.* Thickness Mapping and Layer Number Identification of Exfoliated van der Waals Materials by Fourier Imaging Micro-Ellipsometry. *Acs Nano* **17**, 9188-9196 (2023).

122 Williams, D. & Carter, C. *Transmission Electron Microscopy: A Textbook for Materials Science*. Vol. III (2009).

123 Wang, Z. G. *et al.* Controllable etching of MoS_2 basal planes for enhanced hydrogen evolution through the formation of active edge sites. *Nano Energy* **49**, 634-643 (2018).

124 Michely, T. & Krug, J. *Islands, mounds, and atoms : patterns and processes in crystal growth far from equilibrium*. (Springer, 2004).

125 *Segment Anything*, <https://segment-anything.com/demo>

126 Zhao, Y. Z. & Jin, S. Stacking and Twisting of Layered Materials Enabled by Screw Dislocations and Non-Euclidean Surfaces. *Accounts Mater Res* **3**, 369-378 (2022).

127 Wang, Z. Y. *et al.* Surface-Limited Superconducting Phase Transition on 1T-TaS_2. *Acs Nano* **12**, 12619-12628 (2018).

128 Cho, D. *et al.* Nanoscale manipulation of the Mott insulating state coupled to charge order in 1-TaS_2. *Nat Commun* **7** (2016).
129 Ma, L. G. *et al.* A metallic mosaic phase and the origin of Mott-insulating state in 1T-TaS_2. *Nat Commun* **7** (2016).
130 Navarro-Moratalla, E. *et al.* Enhanced superconductivity in atomically thin TaS_2. *Nat Commun* **7** (2016).
131 Sipos, B. *et al.* From Mott state to superconductivity in 1T-TaS_2. *Nat Mater* **7**, 960-965 (2008).
132 Zhang, H. M., Yan, C. H., Ge, Z. Z., Weinert, M. & Li, L. Impenetrable Barrier at the Metal-Mott Insulator Junction in Polymorphic 1H and 1T $NbSe_2$ Lateral Heterostructure. *J Phys Chem Lett* **13**, 10713-10721 (2022).
133 Fei, Y., Wu, Z. X., Zhang, W. H. & Yin, Y. Understanding the Mott insulating state in 1-TaS_2 and 1-$TaSe_2$. *Aapps B* **32** (2022).
134 Eda, G. *et al.* Coherent Atomic and Electronic Heterostructures of Single-Layer MoS_2. *Acs Nano* **6**, 7311-7317 (2012).
135 Zhao, W. & Ding, F. Energetics and kinetics of phase transition between a 2H and a 1T MoS_2 monolayer-a theoretical study. *Nanoscale* **9**, 2301-2309 (2017).
136 Oyedele, A. D. *et al.* $PdSe_2$: Pentagonal Two-Dimensional Layers with High Air Stability for Electronics. *J Am Chem Soc* **139**, 14090-14097 (2017).
137 Lukowski, M. A. *et al.* Enhanced Hydrogen Evolution Catalysis from Chemically Exfoliated Metallic MoS_2 Nanosheets. *J Am Chem Soc* **135**, 10274-10277 (2013).
138 Voiry, D. *et al.* Conducting MoS_2 Nanosheets as Catalysts for Hydrogen Evolution Reaction. *Nano Lett* **13**, 6222-6227 (2013).
139 Voiry, D. *et al.* Enhanced catalytic activity in strained chemically exfoliated WS_2 nanosheets for hydrogen evolution. *Nat Mater* **12**, 850-855 (2013).
140 Feng, L. Y., Villaos, R. A. B., Huang, Z. Q., Hsu, C. H. & Chuang, F. C. Layer-dependent band engineering of Pd dichalcogenides: a first-principles study. *New J Phys* **22** (2020).
141 Duerloo, K. A. N., Li, Y. & Reed, E. J. Structural phase transitions in two-dimensional Mo- and W-dichalcogenide monolayers. *Nat Commun* **5** (2014).
142 Li, Y., Duerloo, K. A. N., Wauson, K. & Reed, E. J. Structural semiconductor-to-semimetal phase transition in two-dimensional materials induced by electrostatic gating. *Nat Commun* **7** (2016).
143 Wilson, J. A., Di Salvo, F. J. & Mahajan, S. Charge-density waves and superlattices in the metallic layered transition metal dichalcogenides (Reprinted from Advances in Physics, vol 32, pg 882, 1974). *Advances in Physics* **50**, 1171-1248 (2001).
144 Zou, Q. *et al.* Competitive and cooperative electronic states in $Ba(Fe_{1-x}T_x)_2As_2$ with T = Co, Ni, Cr. *Npj Quantum Mater* **6** (2021).
145 Wortmann, B. *et al.* Reversible 2D Phase Transition Driven By an Electric Field: Visualization and Control on the Atomic Scale. *Nano Lett* **16**, 528-533 (2016).
146 Guguchia, Z. *et al.* Magnetism in semiconducting molybdenum dichalcogenides. *Sci Adv* **4** (2018).
147 Zhao, H., Pettes, M. T., Zheng, Y. & Htoon, H. Site-controlled telecom-wavelength single-photon emitters in atomically-thin $MoTe_2$. *Nat Commun* **12** (2021).

148 Eibschutz, M., Mahajan, S., Disalvo, F. J., Hull, G. W. & Waszczak, J. V. Ferromagnetism in Metallic Intercalated Compounds Fe_xTaS_{-2} (0.20 Less-Than-or-Equal-to X Less-Than-or-Equal-to 0.34). *J Appl Phys* **52**, 2098-2100 (1981).
149 Narita, H. *et al.* Preparation and Physical-Properties of Fe_xTaS_{-2} (0.15-Less-Than-or-Equal-to-X-Less-Than-or-Equal-to-0.50) Compounds. *J Solid State Chem* **108**, 148-151 (1994).
150 Ko, K. T. *et al.* RKKY Ferromagnetism with Ising-Like Spin States in Intercalated $Fe_{1/4}TaS_2$. *Phys Rev Lett* **107** (2011).
151 Xie, L. S., Husremovic, S., Gonzalez, O., Craig, I. M. & Bediako, D. K. Structure and Magnetism of Iron- and Chromium-Intercalated Niobium and Tantalum Disulfides. *J Am Chem Soc* **144**, 9525-9542 (2022).
152 Hardy, W. J. *et al.* Very large magnetoresistance in $Fe_{0.28}TaS_2$ single crystals. *Phys Rev B* **91** (2015).
153 Danz, T. *et al.* Structural and magnetic characterization of large area, free-standing thin films of magnetic ion intercalated dichalcogenides $Mn_{-0.25}TaS_2$ and $Fe_{0.25}TaS_2$. *J Phys-Condens Mat* **28** (2016).
154 Horibe, Y. *et al.* Color Theorems, Chiral Domain Topology, and Magnetic Properties of Fe_xTaS_2. *J Am Chem Soc* **136**, 8368-8373 (2014).
155 Chen, C. W., Chikara, S., Zapf, V. S. & Morosan, E. Correlations of crystallographic defects and anisotropy with magnetotransport properties in Fe_xTaS_2 single crystals ($0.23 \leq x \leq 0.35$). *Phys Rev B* **94** (2016).
156 Wilson, J. A. & Yoffe, A. D. The transition metal dichalcogenides discussion and interpretation of the observed optical, electrical and structural properties. *Advances in Physics* **18**, 193-335 (1969).
157 Ribak, A. *et al.* Chiral superconductivity in the alternate stacking compound 4Hb-TaS_2. *Sci Adv* **6** (2020).
158 Liu, W. *et al.* Experimental observations and density functional simulations on the structural transition behavior of a two-dimensional transition-metal dichalcogenide. *Sci Rep-Uk* **10** (2020).
159 Scholz, G. A., Singh, O., Frindt, R. F. & Curzon, A. E. Charge-Density Wave Commensurability in 2h-Tas_2 and Ag_xTaS_2. *Solid State Commun* **44**, 1455-1459 (1982).
160 Fujisawa, Y. *et al.* Superposition of $\sqrt{13}$ x $\sqrt{13}$ and 3 x 3 supermodulations in TaS_2 probed by scanning tunneling microscopy. *J Phys Conf Ser* **969** (2018).
161 Zhao, W. M. *et al.* Moire enhanced charge density wave state in twisted 1T-$TiTe_2$/1T-$TiSe_2$ heterostructures. *Nat Mater* **21**, 284-+ (2022).
162 Mchugh, J. G., Enaldiev, V. V. & Fal'ko, V. I. Moiré superstructures in marginally twisted NbSe2 bilayers. *Phys Rev B* **108** (2023).
163 Cheung, C. T. S. *et al.* Coexisting Charge Density Waves in Twisted Bilayer $NbSe_2$. *Nano Lett* **24**, 12088-12094 (2024).
164 Li, Z. J. *et al.* Beyond Conventional Charge Density Wave for Strongly Enhanced 2D Superconductivity in 1H-TaS_2 Superlattices. *Adv Mater* **36** (2024).
165 Bernevig, B. A., Felser, C. & Beidenkopf, H. Progress and prospects in magnetic topological materials. *Nature* **603**, 41-51 (2022).

166 Zhang, X. M. *et al.* Magnetic topological materials in two-dimensional: theory, material realization and application prospects. *Sci Bull* **68**, 2639-2657 (2023).
167 Ma, J. Z. *et al.* Spin fluctuation induced Weyl semimetal state in the paramagnetic phase of $EuCd_2As_2$. *Sci Adv* **5** (2019).
168 Jo, N. H. *et al.* Manipulating magnetism in the topological semimetal $EuCd_2As_2$. *Phys Rev B* **101**, 140402 (2020).
169 Taddei, K. M. *et al.* Single pair of Weyl nodes in the spin-canted structure of $EuCd_2As_2$. *Phys Rev B* **105**, L140401 (2022).
170 Riberolles, S. X. M. *et al.* Magnetic crystalline-symmetry-protected axion electrodynamics and field-tunable unpinned Dirac cones in $EuIn_2As_2$. *Nat Commun* **12**, 999 (2021).
171 Yan, J. *et al.* Field-induced topological Hall effect in antiferromagnetic axion insulator candidate $EuIn_2As_2$. *Physical Review Research* **4**, 013163 (2022).
172 Soh, J. R. *et al.* Ideal Weyl semimetal induced by magnetic exchange. *Phys Rev B* **100**, 201102 (2019).
173 Ma, J. *et al.* Emergence of Nontrivial Low-Energy Dirac Fermions in Antiferromagnetic $EuCd_2As_2$. *Adv Mater* **32** (2020).
174 Santos-Cottin, D. *et al.* $EuCd_2As_2$: A Magnetic Semiconductor. *Phys Rev Lett* **131**, 186704 (2023).
175 Wang, Y. X. *et al.* Absence of metallicity and bias-dependent resistivity in low-carrier-density $EuCd_2As_2$. *Sci China Phys Mech* **67**, 247311 (2024).
176 Nishihaya, S. *et al.* Intrinsic insulating transport characteristics in low-carrier density $EuCd_2As_2$ films. *Appl Phys Lett* **124**, 023103 (2024).
177 Sun, Y. K. *et al.* Experimental evidence for field-induced metamagnetic transition of $EuCd_2As_2$. *J Rare Earth* **40**, 1606-1610 (2022).
178 Gong, M. D. *et al.* Surface state evolution induced by magnetic order in axion insulator candidate $EuIn_2As_2$. *Phys Rev B* **106** (2022).
179 Li, Y. *et al.* Surface and electronic structure of antiferromagnetic axion insulator candidate $EuIn_2As_2$. *Acta Physica Sinica* **70**, 186801-186801-186801-186809 (2021).
180 Blawat, J. *et al.* Unusual Electrical and Magnetic Properties in Layered $EuZn_2As_2$. *Adv Quantum Technol* **5** (2022).
181 Regmi, P., Blawat, J. & Jin, R. Y. Large unconventional Hall effect observed in $EuZn_2As_2$. *Phys Rev B* **111** (2025).
182 Perdew, J. P., Burke, K. & Ernzerhof, M. Generalized gradient approximation made simple. *Phys Rev Lett* **77**, 3865-3868 (1996).
183 Dudarev, S. L., Botton, G. A., Savrasov, S. Y., Humphreys, C. J. & Sutton, A. P. Electron-energy-loss spectra and the structural stability of nickel oxide: An LSDA+U study. *Phys Rev B* **57**, 1505-1509 (1998).
184 Liu, Y. *et al.* Experimental discovery of structure–property relationships in ferroelectric materials via active learning. *Nature Machine Intelligence* **4**, 341-350 (2022).
185 Narasimha, G. *et al.* Multiscale structure-property discovery via active learning in scanning tunneling microscopy. *arXiv e-prints*, arXiv:2404.07074 (2024).

186 Wang, Z. C. *et al.* Anisotropy of the magnetic and transport properties of $EuZn_2As_2$. *Phys Rev B* **105** (2022).
187 Blawat, J., Speer, S., Singleton, J., Xie, W. W. & Jin, R. Y. Quantum-limit phenomena and band structure in the magnetic topological semimetal $EuZn_2As_2$. *Commun Phys-Uk* **6** (2023).
188 Narasimha, G., Kong, D., Gai, Z., Vasudevan, R. & Ziatdinov, M. Active Learning Based Structure-Property Correlation in STM. *Microscopy and Microanalysis* **30** (2024).
189 Shahriari, B., Swersky, K., Wang, Z., Adams, R. P. & De Freitas, N. Taking the human out of the loop: A review of Bayesian optimization. *Proceedings of the IEEE* **104**, 148-175 (2015).

Appendices

Appendix A. Pyrometer readings of the crystal and the PBN heater

Power(W)	*PBN Temperature(K)*	*Pt(111) Temperature (K)*
2.5	840	617
3.1	893	639
3.9	968	674
4.7	1023	711
5.7	1096	744
6.8	1154	766
7.4	1213	790
8.8	1291	829
10.1	1346	851
11.0	1390	872
12.6	1437	896
13.7	1497	919
15.6	1556	947
16.8	1594	977
18.5	1663	997
20.0	1720	1021
21.9	1761	1045
23.8	1830	1076
25.5	1872	1112
27.3	1893	1126
29.7	1893	1157